Orchard Storage Company LLC

Underground Injection Control – Class VI Permit Application for

Orchard No. 1 to No. 7

Section 1 – Site Characterization

Gaines County, Texas

Prepared for *Orchard Storage Company LLC*
Houston, Texas

By
Lonquist Sequestration, LLC
Austin, TX

Revised August 2024

LONQUIST SEQUESTRATION LLC

SECTION 1 – SITE CHARACTERIZATION

TABLE OF CONTENTS

Figures

Tables

1.1.   Overview

This site characterization for Orchard Storage Company LLC's (Orchard Storage) Orchard Project, for injection wells No. 1 through No. 7 was prepared to meet the requirements of 16 Texas Administrative Code (TAC) **§5.203 (c)(2)** [Title 40, U.S. Code of Federal Regulations (40 CFR) **§146.82(a)(3)**]. This section describes the regional and site geology for the proposed location. This site characterization incorporates analysis from multiple data types, including core, well logs, seismic (2D), academic and professional publications (e.g., regional geologic frameworks), and nearby subsurface analogs.

1.2.   Regional Geology

1.2.1   Regional Geologic Setting

The Permian Basin is a large sedimentary basin covering more than 75,000 square miles of west Texas and southeastern New Mexico. The basin developed in an open marine environment in the middle of the Carboniferous period, approximately 320-325 million years ago (Galley, 1958). It is an asymmetrical, northwest-southeast trending system bound by the Marathon-Ouachita orogenic belt to the south, the Northwest Shelf and Matador Arch to the north, the Diablo Platform to the west, and the Eastern Shelf to the east (Beaumont, 1981). Figure 1-1 shows a map of the Permian Basin sub-basins and the Orchard location (from Merrill et al., 2015).

Researchers commonly subdivide the Permian Basin into two sub-basins and one platform—the Delaware Basin to the west, the Central Basin Platform in the center, and the Midland Basin to the east (Popova, 2022). The tectonic history of the Permian Basin is mainly affected by the uplift of the Central Basin Platform, and partly by the thrusting of the Marathon-Ouachita orogenic belt, with the main phase of basin differentiation occurring during the Pennsylvanian and Wolfcampian periods due to rapid subsidence in the Delaware and Midland basins (Popova, 2020).
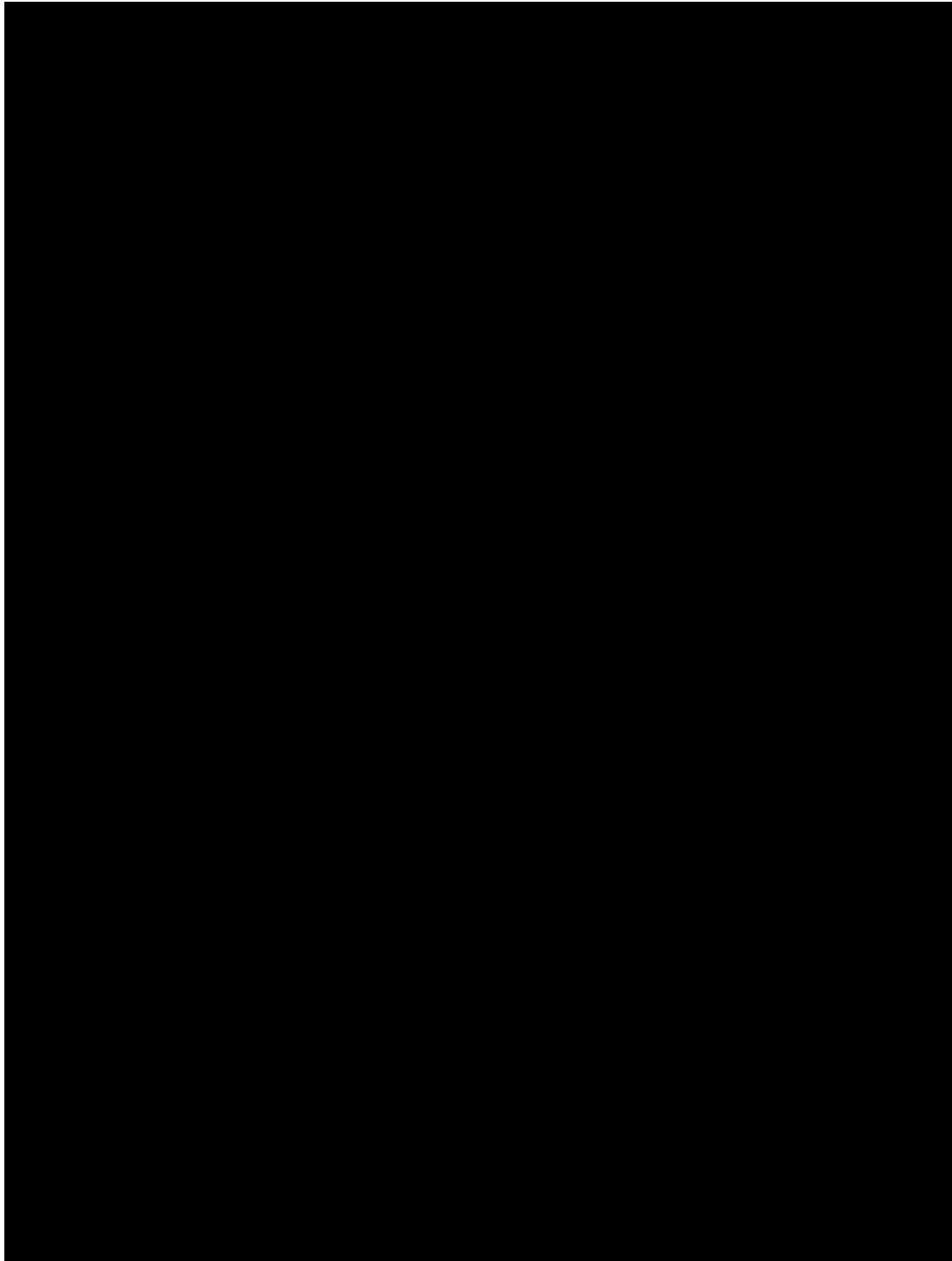
Figure 1-1 – Permian Basin sub-basins with the Orchard location indicated by the black star (from Merrill et al., 2015).

1.2.2 Regional Stratigraphic Model

The Permian Basin Paleozoic succession is comprised of carbonate, clastic, and evaporite rocks. Figure 1-2 shows a generalized stratigraphic column of geologic units in the Paleozoic strata of the Permian Basin (Merrill et al., 2015). This Permian System stratigraphy, per the U.S. Geological Survey (USGS) assessment of CO_2 storage opportunities, reflects a composite of several stratigraphic schemes attributed to several decades of hydrocarbon development in the area.

System	Series/Stage	Stratigraphic unit				
		NW Shelf New Mexico	Delaware Basin	Central Basin Platform	Midland Basin	NW Shelf Texas
Triassic	Upper	Santa Rosa	Santa Rosa	Dockum	Dockum	Dockum
Permian	Ochoan	Dewey Lake	Dewey Lake	Dewey Lake	Dewey Lake	Dewey Lake
		Rustler	Rustler	Rustler	Rustler	Rustler
		Salado	Salado	Salado	Salado	Salado
			Castile			
	Guadalupian	Artesia Gp.: Tansill / Yates / Seven Rivers / Queen (Goat Seep) / Grayburg; Capitan	Delaware Mountain Gp.: Bell Canyon / Cherry Canyon / Brushy Canyon	Capitan; Tansill / Yates / Seven Rivers / Queen (Goat Seep) / Grayburg (Artesia Gp.)	Artesia Gp.: Tansill / Yates / Seven Rivers / Queen / Grayburg	Artesia Gp.: Tansill / Yates / Seven Rivers / Queen / Grayburg
		San Andres: upper San Andres / lower San Andres	Brushy Canyon / Cutoff	San Andres: upper San Andres / lower San Andres / Holt	San Andres	San Andres: upper San Andres / lower San Andres
	Leonardian	Yeso: Glorieta / Paddock / Blinebry / Tubb / Drinkard; Abo	Bone Spring: 1st carbonate / 1st sand / 2nd carbonate / 2nd sand / 3rd carbonate / 3rd sand / lower carbonate	Glorieta / upper Clear Fork / middle Clear Fork / Tubb / lower Clear Fork (Clear Fork Gp.); Wichita / Abo	undivided clastic and carbonate rocks; Spraberry / Dean	Glorieta / upper Clear Fork / middle Clear Fork / Tubb / lower Clear Fork (Clear Fork Gp.); Abo
	Wolfcampian	Hueco	Hueco	Wolfcamp	Wolfcamp	Wolfcamp

Figure 1-2 – Generalized stratigraphic column of geologic units in the Paleozoic strata of the Permian Basin (Merrill et al., 2015).

Each stratigraphic succession reflects a composite of high-frequency cyclicity incorporating lowstand, transgressive, and highstand system tracts across the region. These successions are reflective of paleo-topographic changes across the area caused by sea-level fluctuation, subsidence, water depth, and compaction forces. █████████████████████████████ ███████████████████████████

███ ███ ███████████████████████████████████
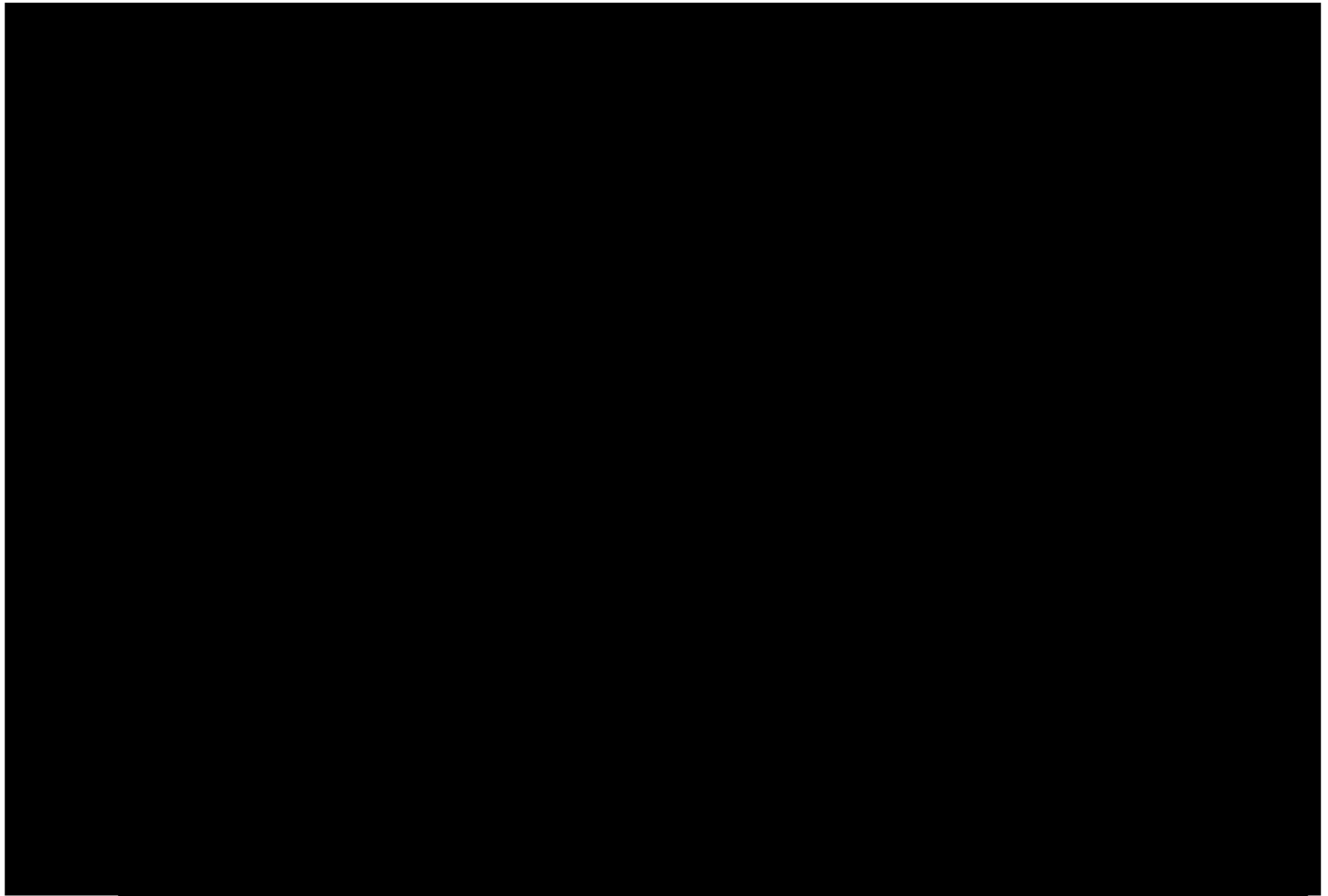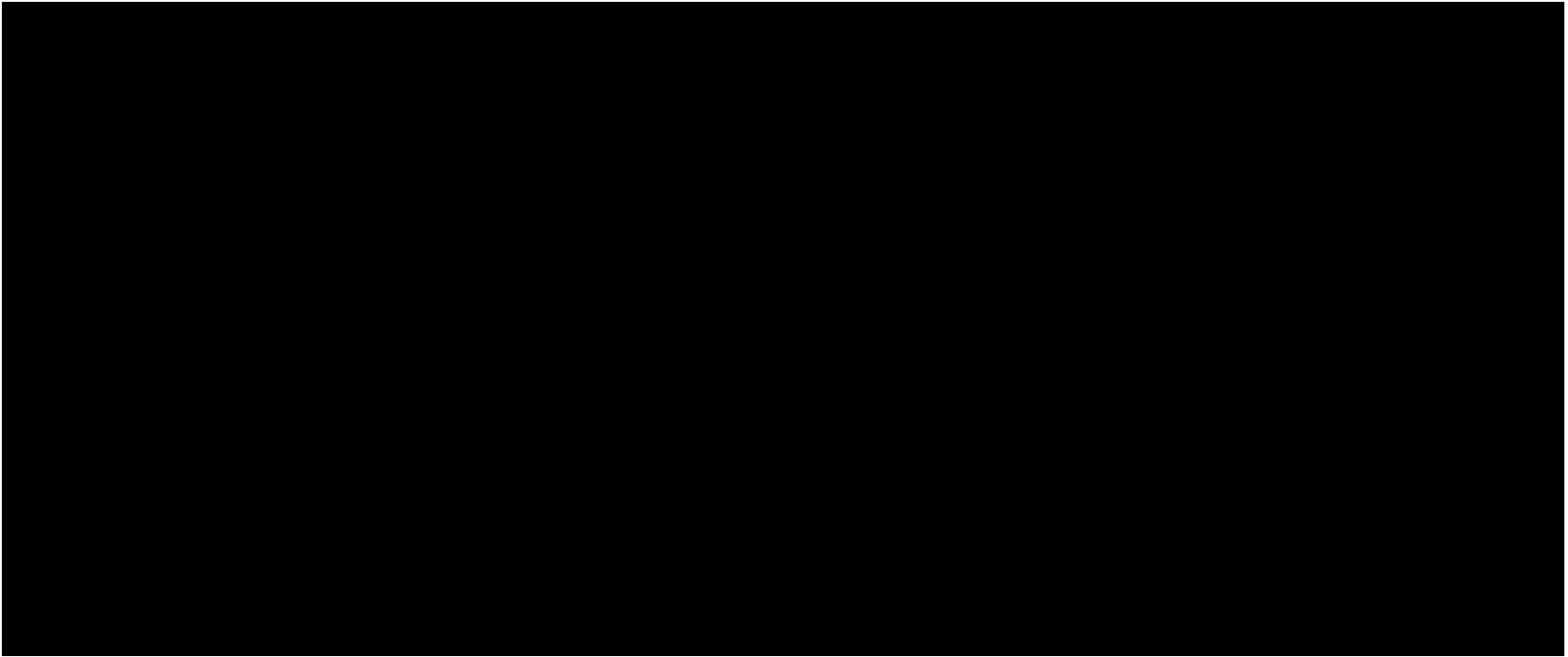
Figure 1-3 —

Figure 1-4 – ██

1.2.3 Regional Depositional Model

Facies are associated with shelf-to-basin changes across the region. The proposed Orchard No. 1–No. 7 injection wells are in an area that reflects evolution from slope- to supratidal-dominated regimes, from the Leonardian through the Guadalupian successions. Iterations of the regional depositional model have been developed through several decades of academic and professional research. These models incorporate the research of time-equivalent outcrops in western Texas and eastern New Mexico, showing shelf-to-basin changes from the Northwest Shelf into the Delaware Basin portion of the Permian Basin. These models correlate to the Leonardian and Guadalupian successions in the Central Basin Platform, Northwest Shelf, Midland Basin, and Eastern Shelf, as Figure 1-5 shows.
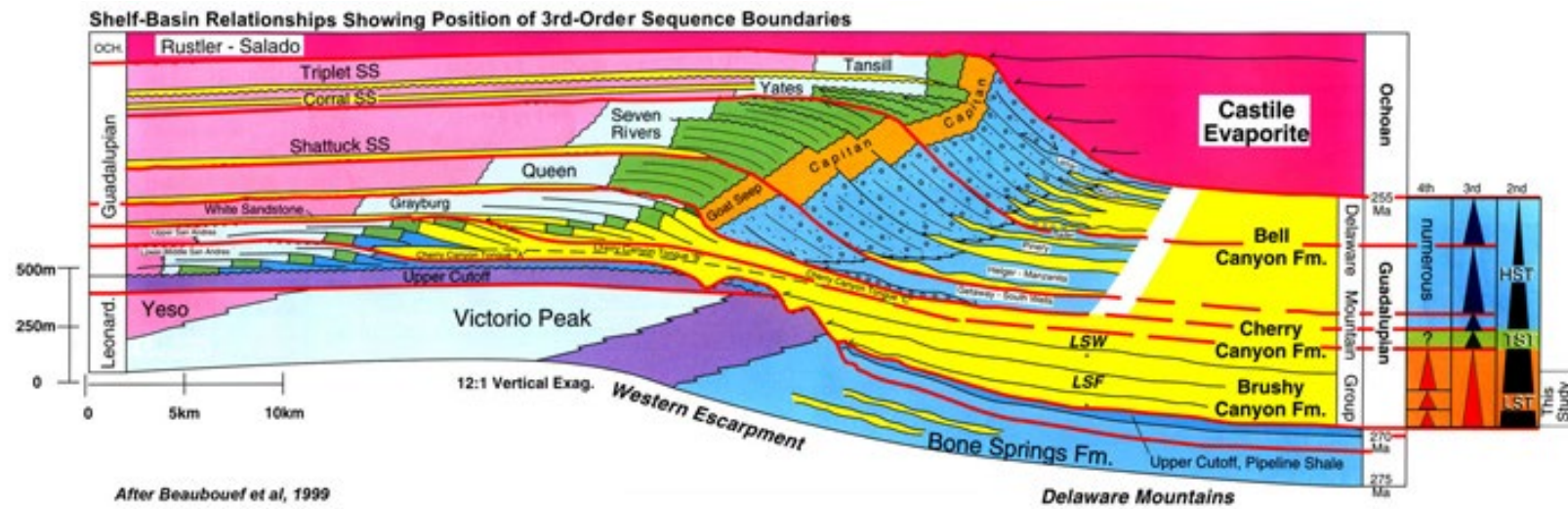
Figure 1-5 – Upper Permian stratigraphy of the Northwest Shelf of the Delaware Basin (after Beaubouef et al., 1999).

1.2.4 Major Stratigraphic Units
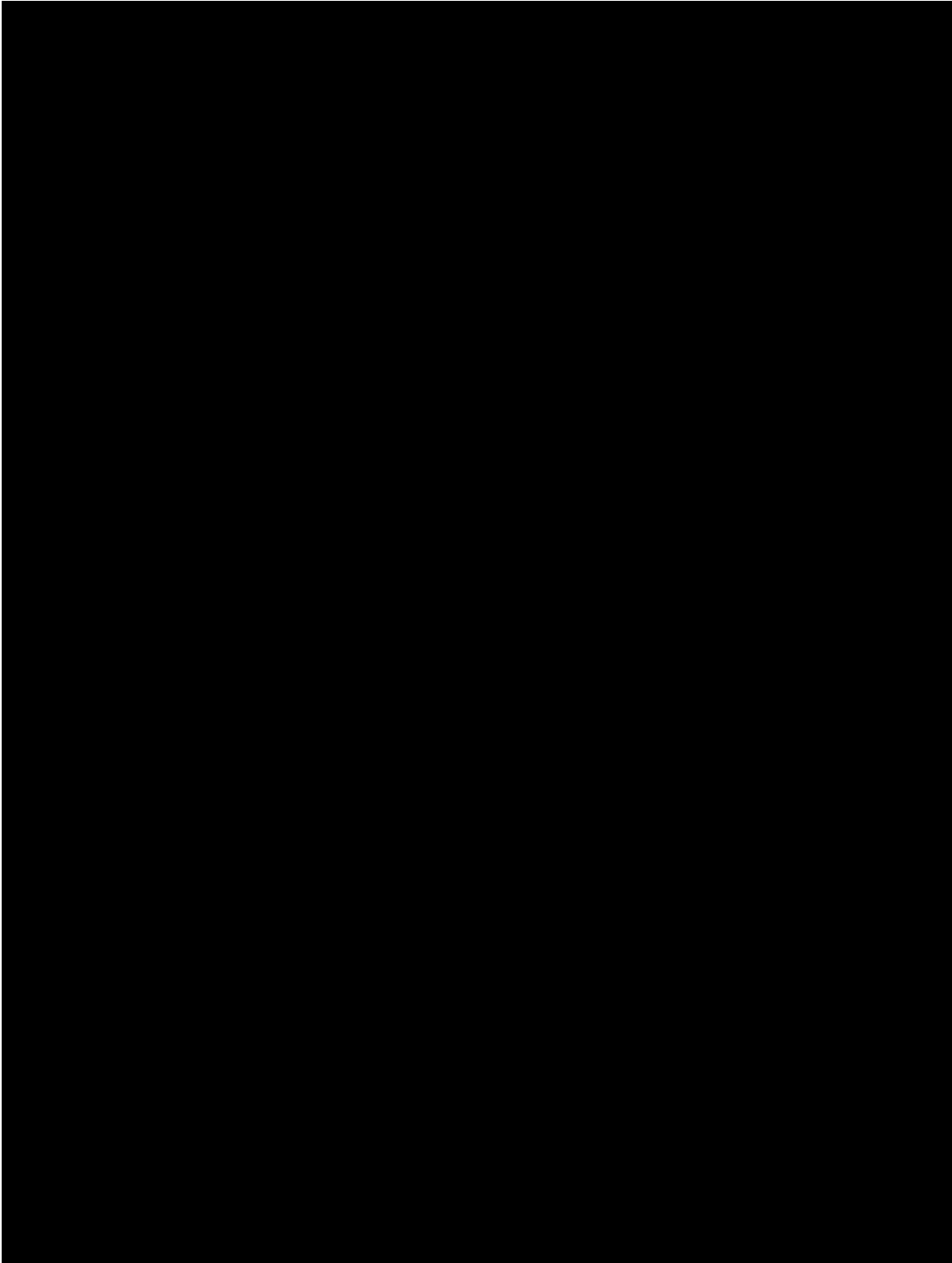
Figure 1-6 – Reference map showing the location of cross section B-B' (Figure 1-7) from west to east through the Orchard location (indicated by the black star).
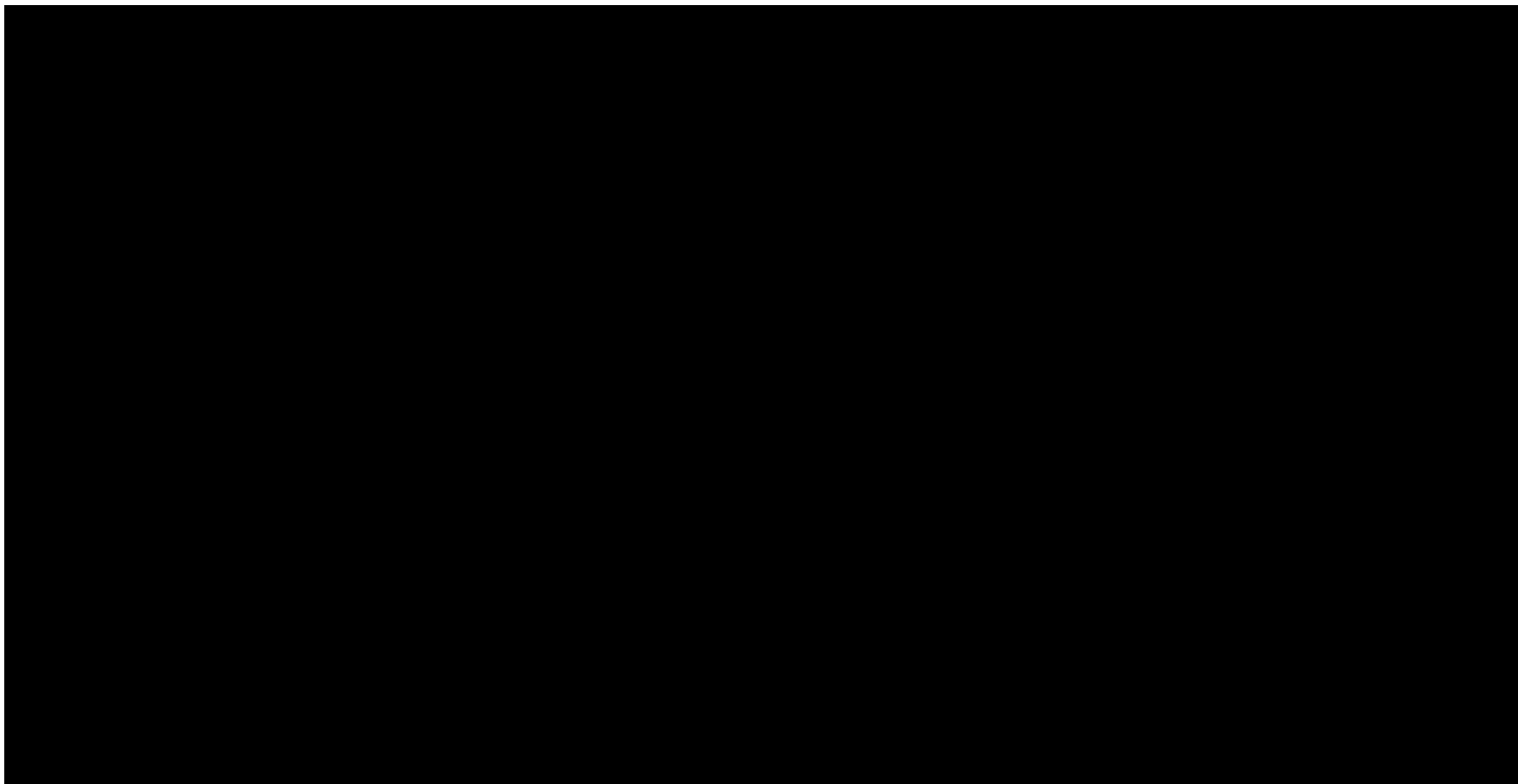
Figure 1-7 – A west-to-east cross section illustrating the change of lithofacies and stratigraphy in the ███████████████████████████████ ███████████████████████████████
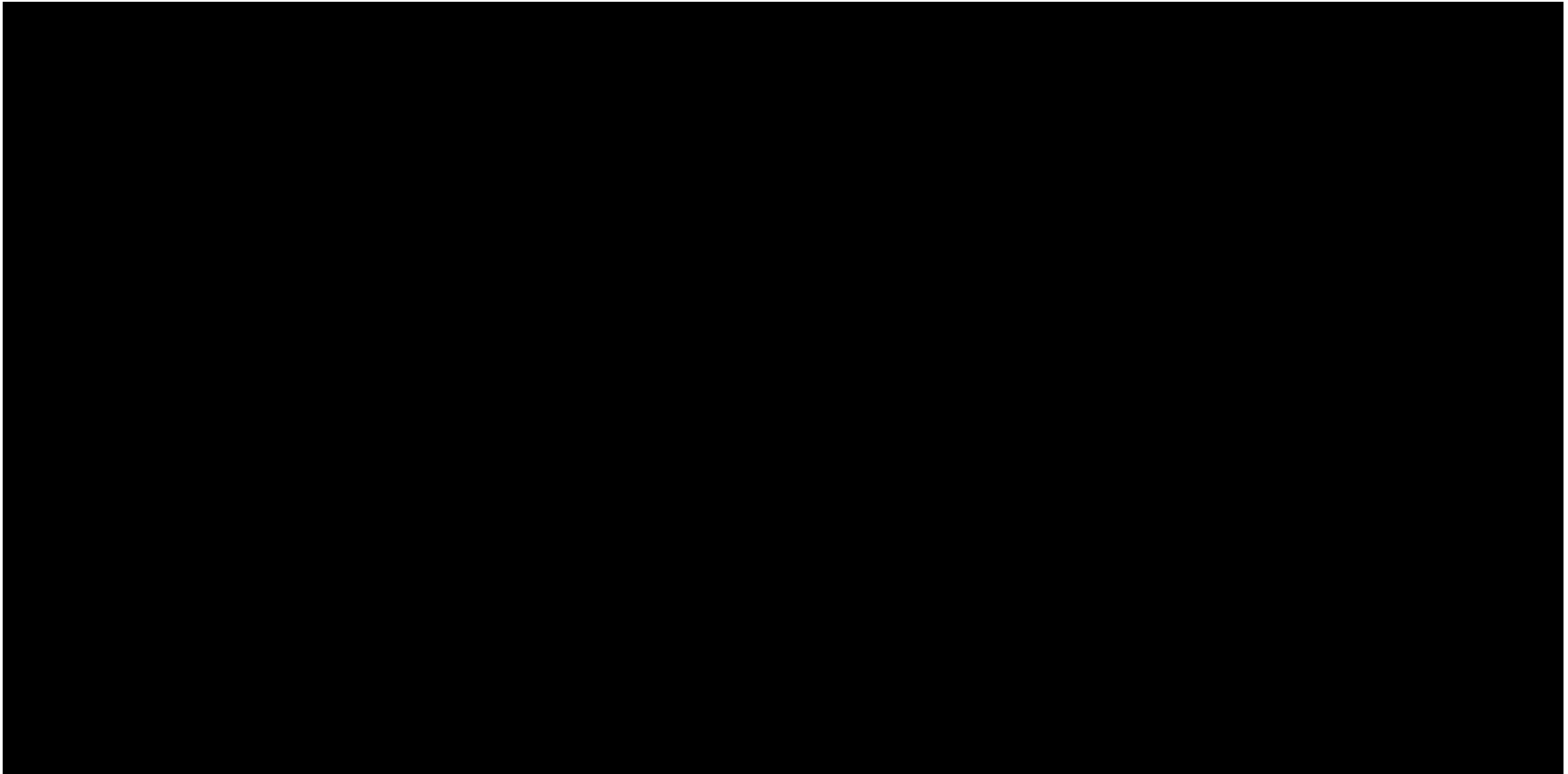
Figure 1-8 – Base map showing the location of the Orchard Project (black star) and the ████████████████████████████████

Figure 1-9 – A simplified depositional facies model relative to the position on
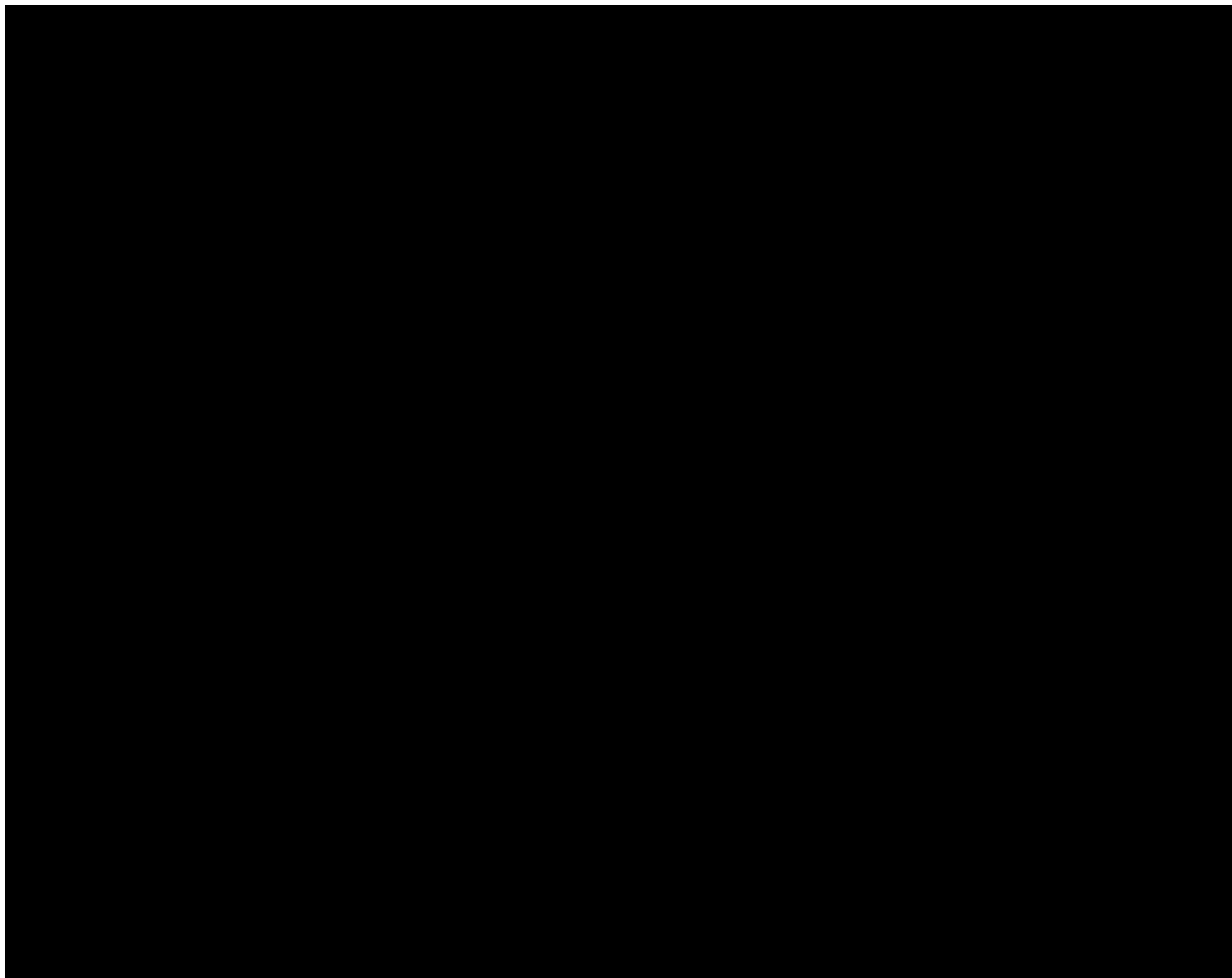
Figure 1-10 –
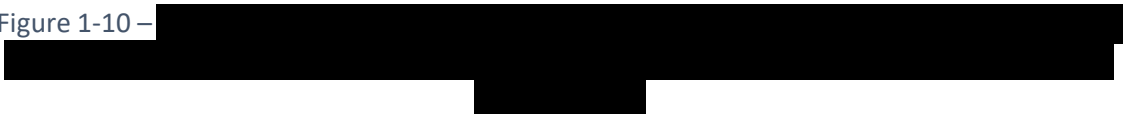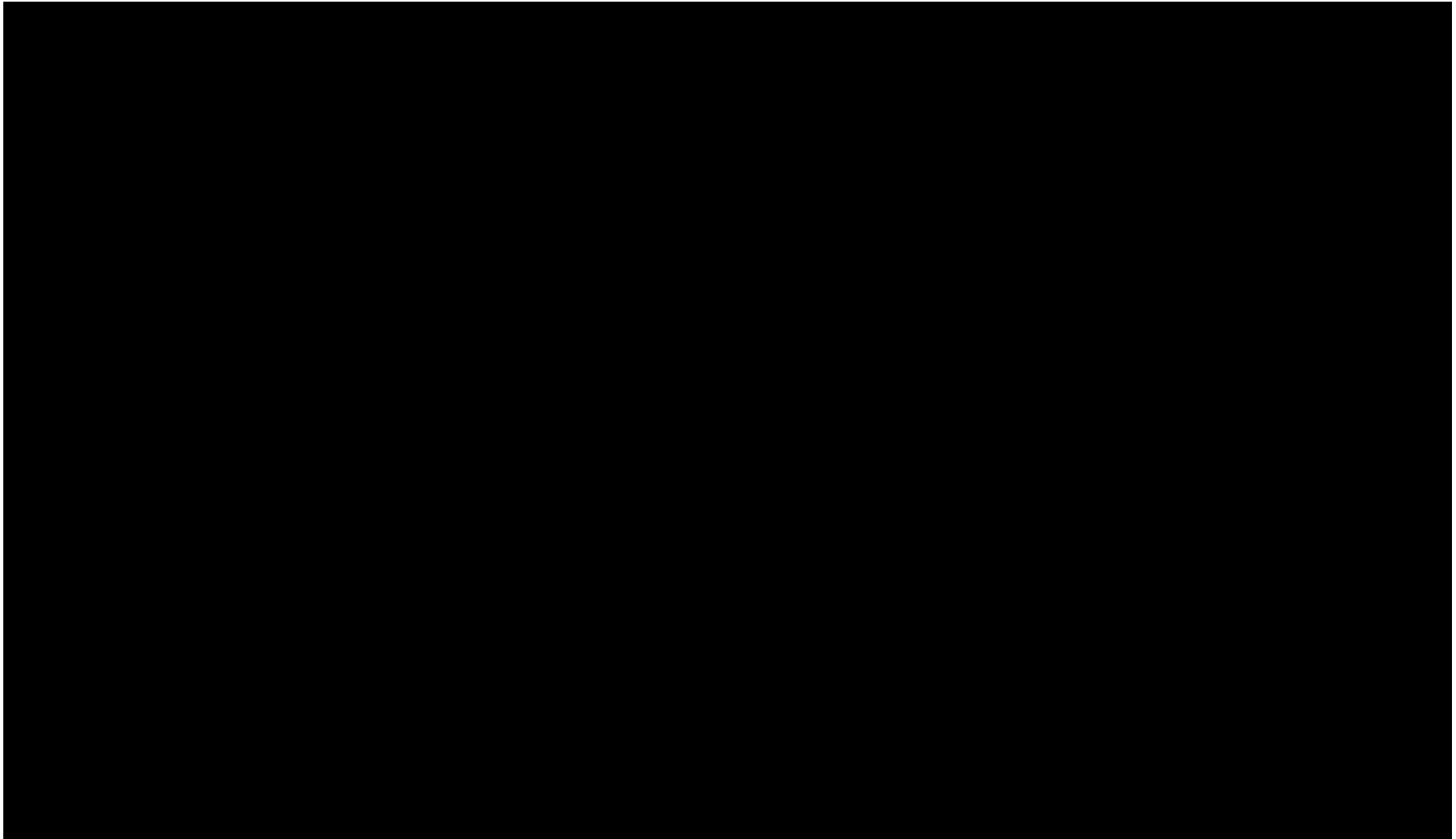
Figure 1-11 – Schematic cross section showing the hierarchy of composite/high-frequency sequences for the ▮▮▮▮▮▮▮▮▮▮▮▮
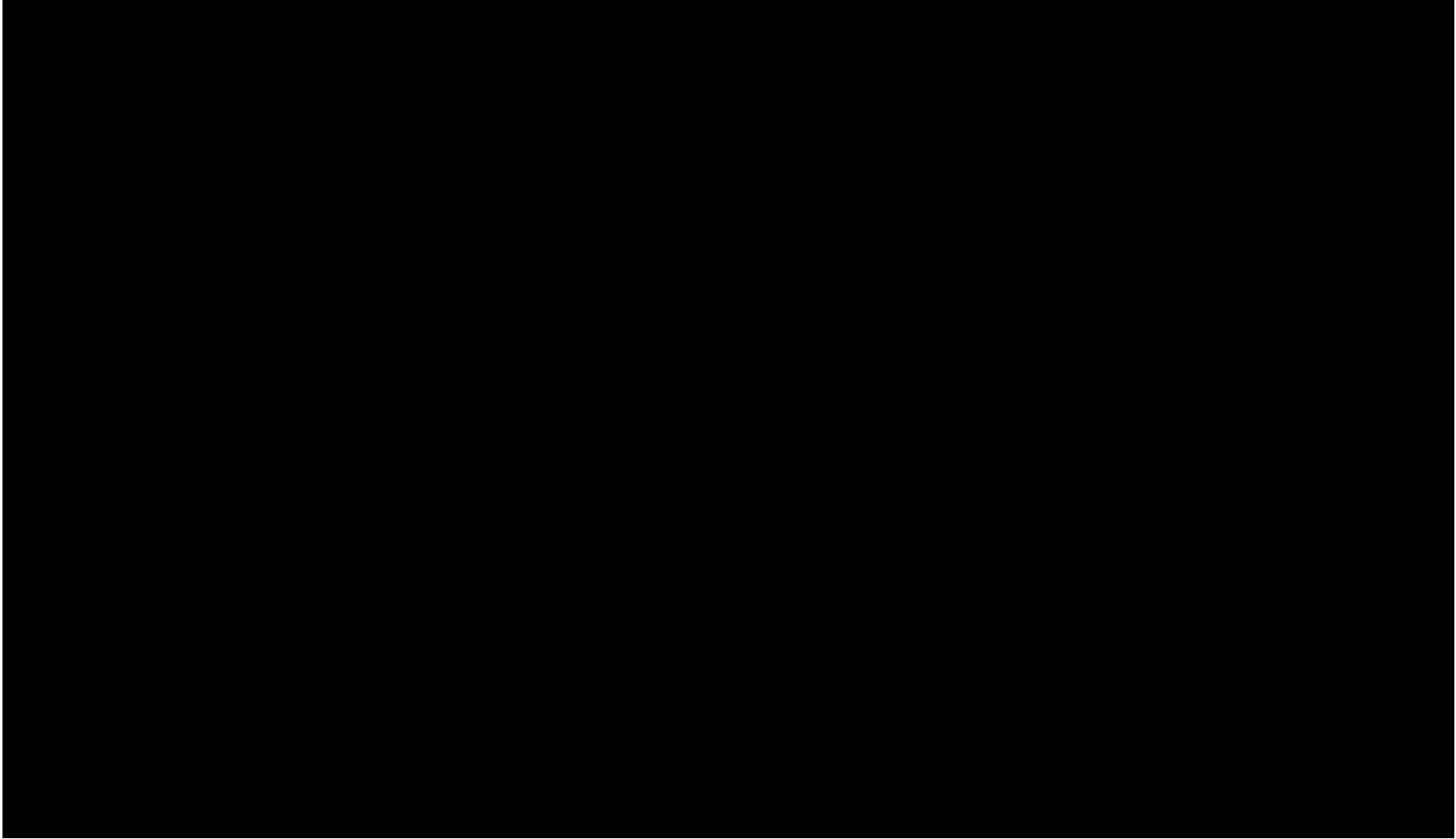
Figure 1-12 – A schematic cross section of the dominant lithofacies across the high-frequency cycles shown previously, based on observations from several regional ███.
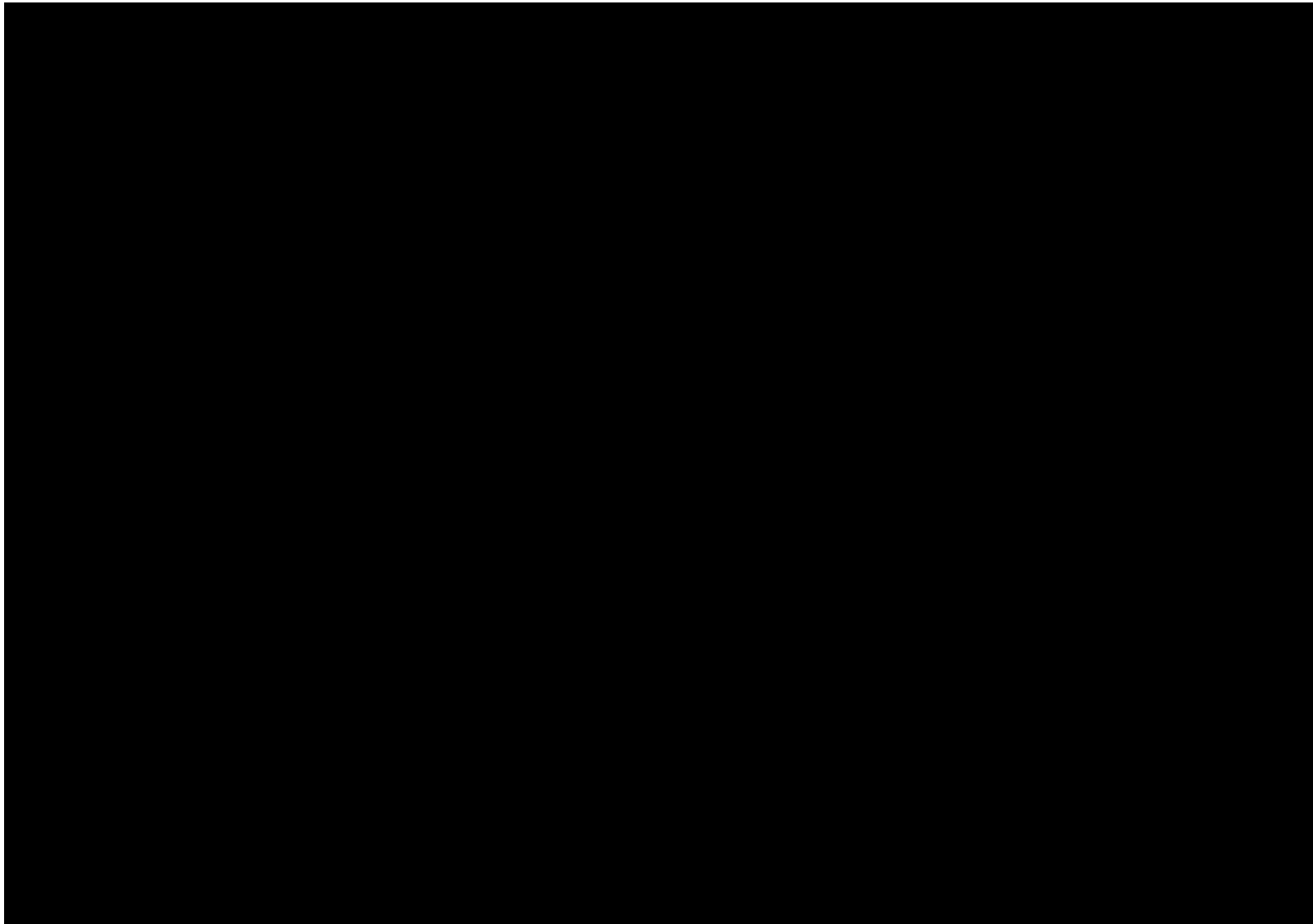
Figure 1-13 – Map of hydrocarbon-producing play areas associated with the ████████████████ relative to the Orchard No. 1–No. 7 locations (indicated by the blue diamonds) and the wider area around them (black dashed polygon).
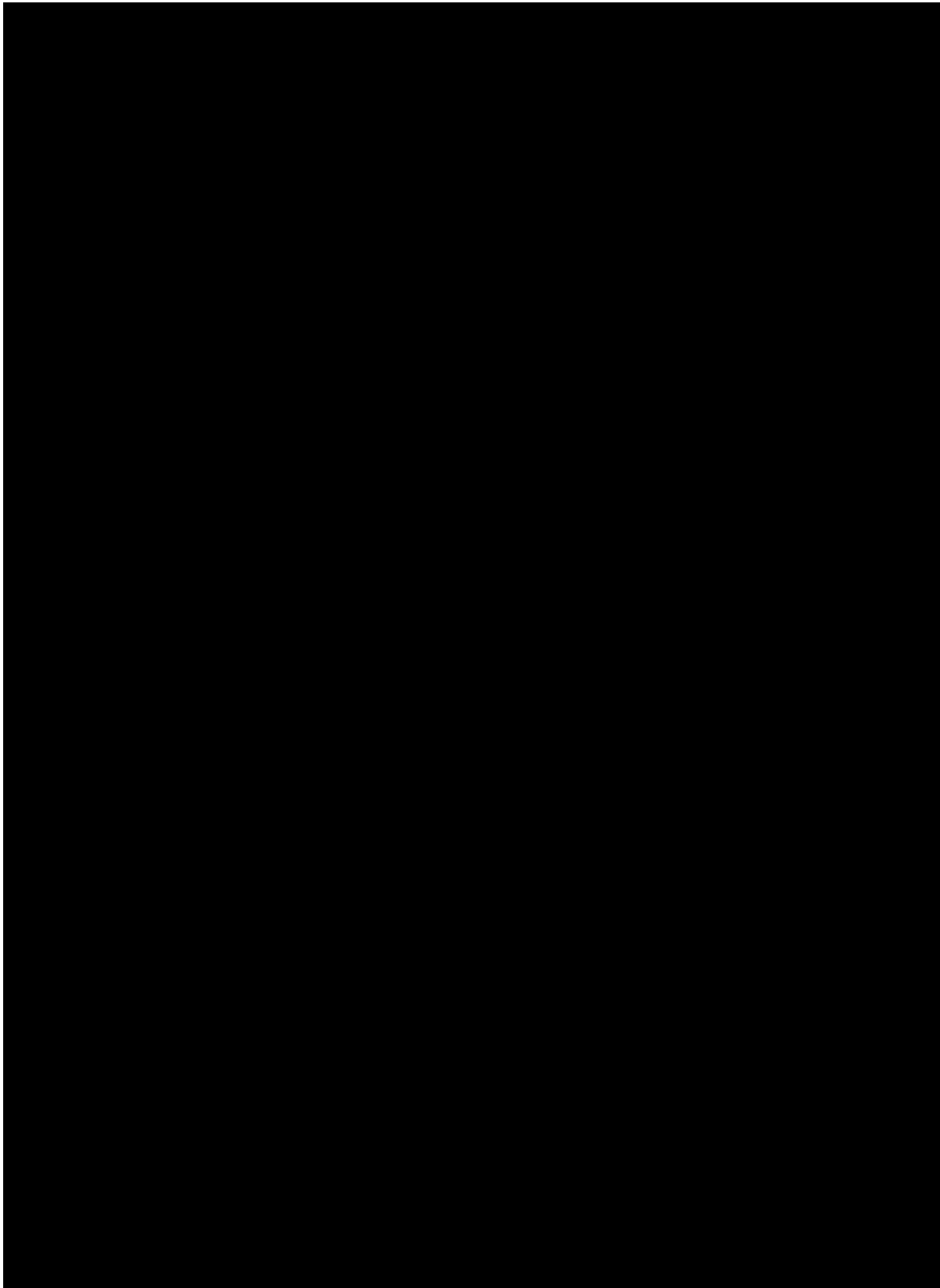
Figure 1-14 – Simplified map highlighting the regional patterns of dominant lithologies in the confining zone part of the ███████████████████████████████████████

1.3. Site Geology

The proposed Orchard No. 1–No. 7 site is located ███████████████████████ ███████████████████████ Gaines County, Texas. The wider area around the proposed site provides multiple data types that increased the accuracy of this site characterization. Figure 1-15 shows a map of the individual locations of Orchard No. 1 through No. 7 relative to existing wells within the wider area and associated with hydrocarbon-producing play areas.
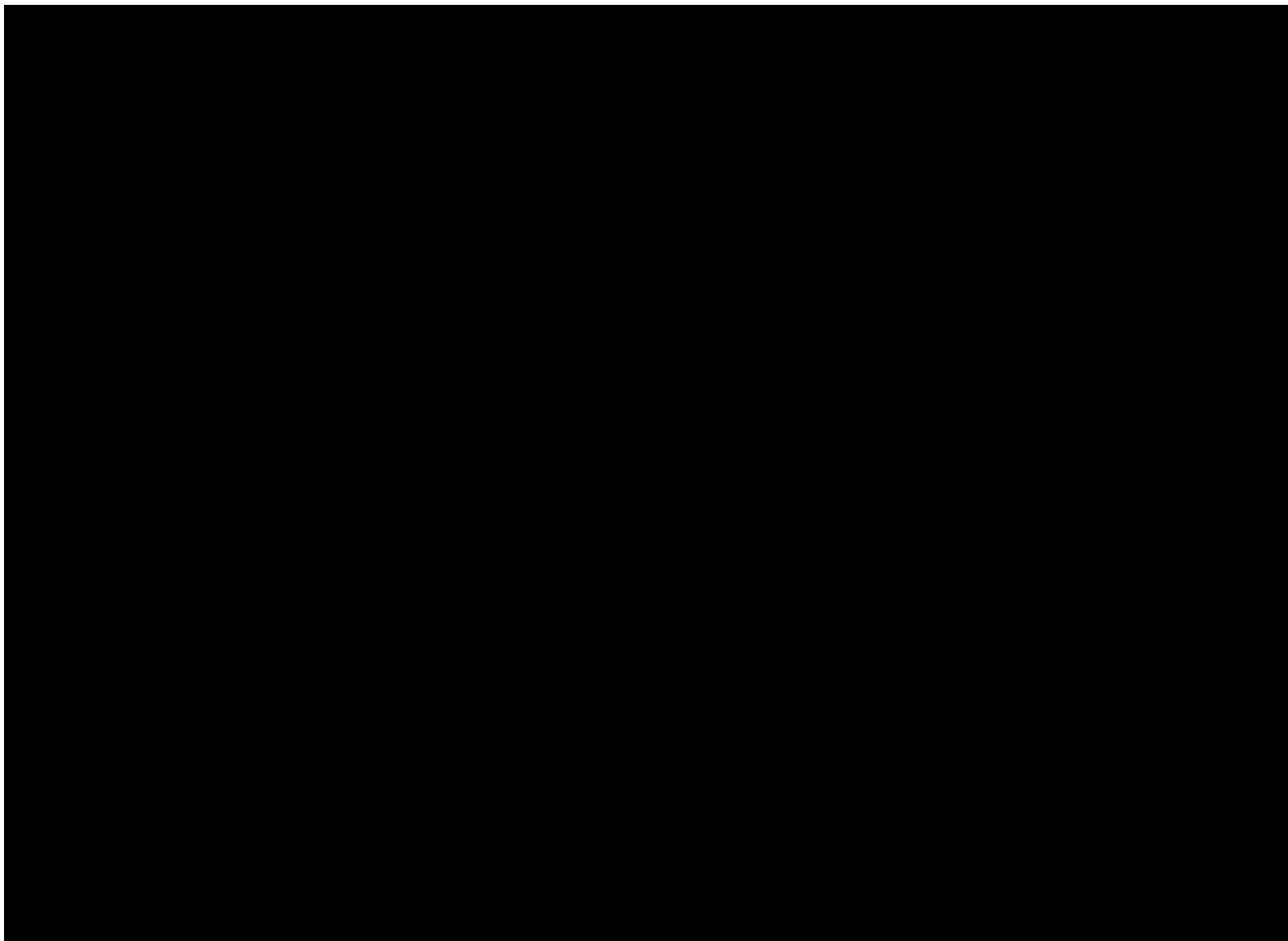
Figure 1-15 – Map of the Orchard No. 1–No. 7 locations (indicated by the blue diamonds) relative to existing wells within the wider area (black, dashed outline) and associated with hydrocarbon-producing play areas.

Subsurface data and analysis from several wells drilled in the area were incorporated into this site evaluation for the major stratigraphic units. These wells—all dry holes—provide sources of core, wireline logs, and mud logs, plus injectivity and productivity data over several decades.

Furthermore, 2D seismic data is available in the Orchard Project area and has been integrated into the subsurface analysis. The seismic data and offset well data have helped to reduce subsurface uncertainty and risk for the project. The resulting interpretations of the project site and broader area, together with the regional geologic model, were used to create a 3D model discussed in *Section 2 – Plume Model.*

Figure 1-16 shows a map of the Orchard No. 1–No. 7 locations, available subsurface data used for this site characterization, and nearby well-known hydrocarbon-producing play areas.
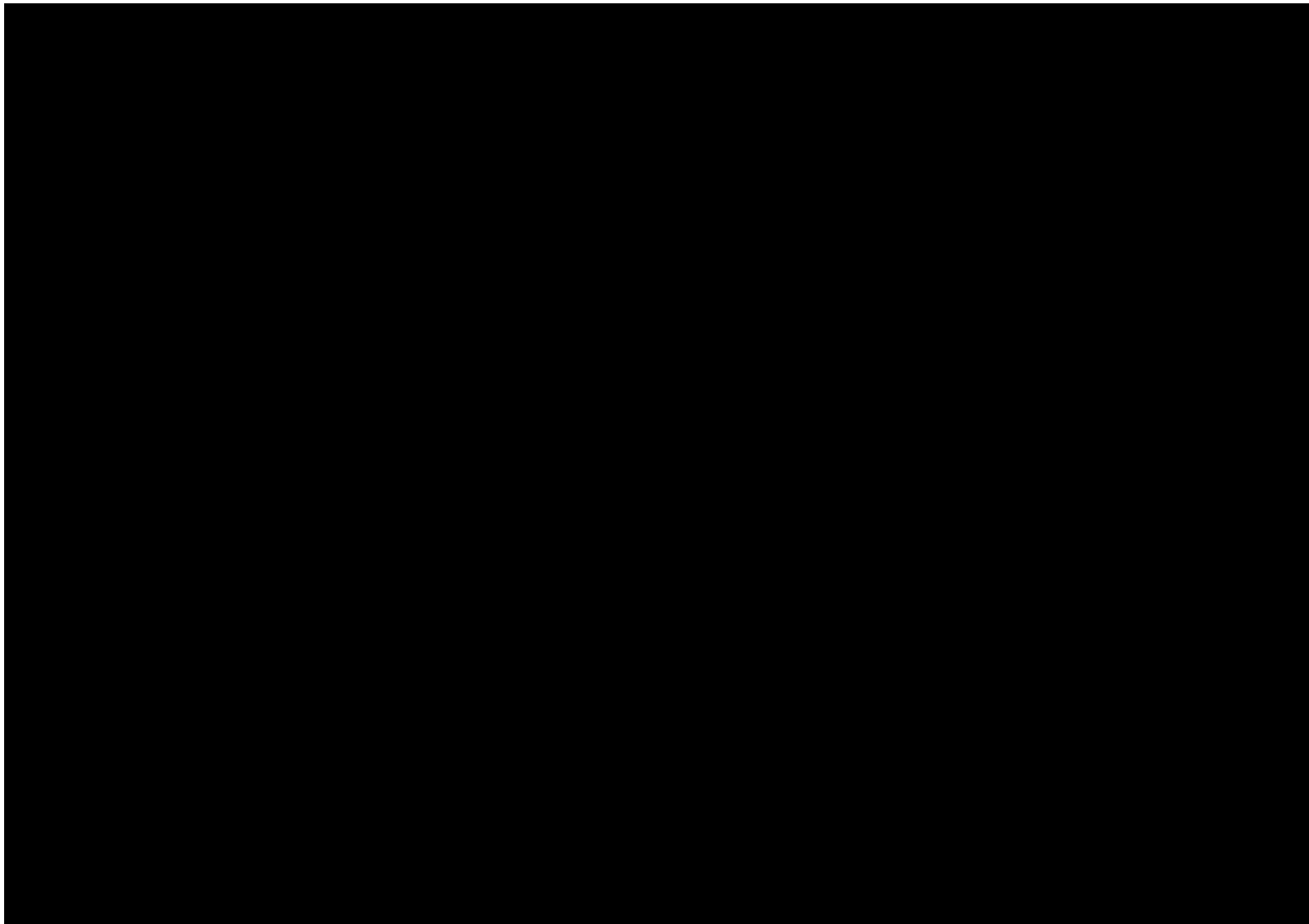
Figure 1-16 – Map of the Orchard No. 1–No. 7 locations (indicated by the blue diamonds), available subsurface data used for the site characterization, and nearby well-known hydrocarbon-producing play areas. The red line indicates the 2D seismic line evaluated.

1.3.1 Subsurface Data and Methods

<u>Well Logs</u>

Digital well log files (.las file format) were used for several site characterization tasks, including stratigraphic top determinations, petrophysical calculations, integration to the core and seismic data, and creation of a 3D conceptual and numerical model ("geomodel"). These well logs were the primary source for understanding vertical and lateral rock quality changes in the injection and confining zones. Several wells drilled after 1980 have high-quality electric wireline logs suitable for quantitative lithology, porosity, permeability, and fluid-type derivations via petrophysical analysis. It is important to note that some of those wells do not penetrate the entire ███████████████████.

Thirty-three wells within the Orchard Project area were identified as having a complete suite of well logs for petrophysical analysis. Neutron and density logs were critical to quantitatively deriving porosity and lithologic information for the injection and confining zones. These wells were selected based on their relatively consistent spacing throughout the project area and to provide a picture of the subsurface without heavily biasing one location. Table 1-1 shows select well-log data used for this site characterization. The digital .las and .pdf files are included in Appendix K.

Table 1-1 – Select well-log data described by log curve type and logged depth intervals, used for this site characterization.

Well API Number	Log Curves	Logged Interval (ft)	KB (ft)	Run Date
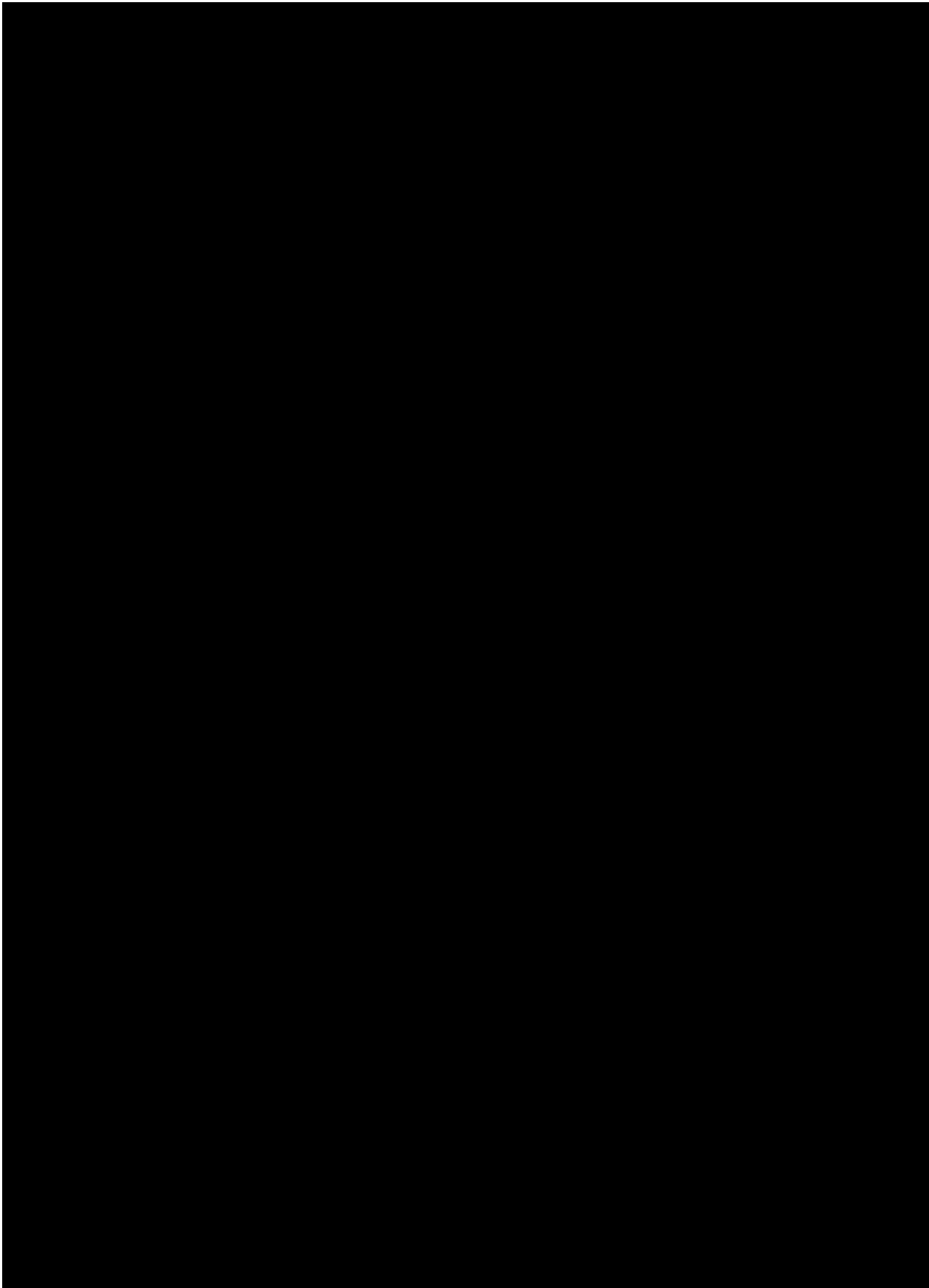
A few of these wells did not have a sufficiently complete suite of well logs for petrophysical analysis but provided qualitative understanding of the injection and confining zones. Two mud logs containing gas readings, and one with a detailed lithological description of all major stratigraphic units, were available. The mud log for the ███████████████████ ████ is included in Appendix K.

The current well tops incorporate elements of lithostratigraphy and regional sequence stratigraphy. The major sequence boundaries were identified and used to create the 3D conceptual and numerical model.

Core

Two wells within the vicinity of the proposed Orchard No. 1–No. 7 wells are sources of site-specific core—from the top of the injection zone and base of the upper confining zone, respectively. Slabbed cores from two ███████████████████████ ███████████████████████████ ere observed, plugged, described, and used for laboratory testing, courtesy of the Texas Bureau of Economic Geology. Table 1-2 provides a list of the cored intervals and testing program completed by Core Lab Houston. The Core Lab Final Core Reports are included in Appendix J-1 and J-2.

Table 1-2 – Cored Intervals and Testing Program
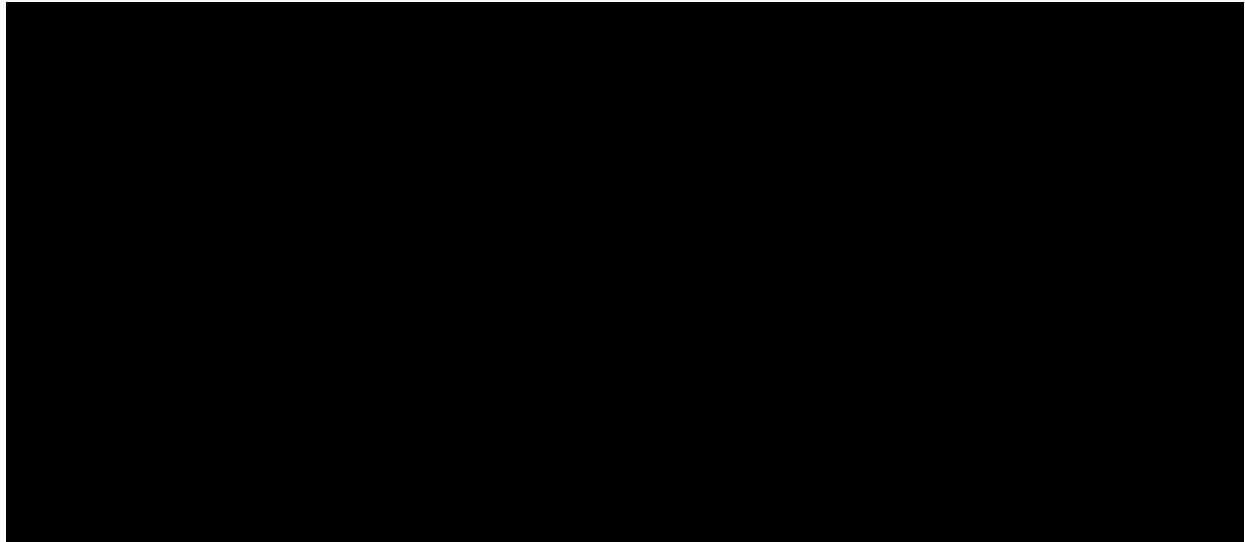
<u>Seismic</u>

Two-dimensional seismic data (post-stack time migrated) provided an additional data source to help understand the stratigraphic and structural variations across the Orchard Project area and tie into the regional and local geologic framework. The 2D seismic line, shown in Figure 1-16, was licensed from a third-party data provider, ███████████████████████████████ ████   The seismic line is ███████████████████████████████   through the project area.

1.3.2   Injection Zone
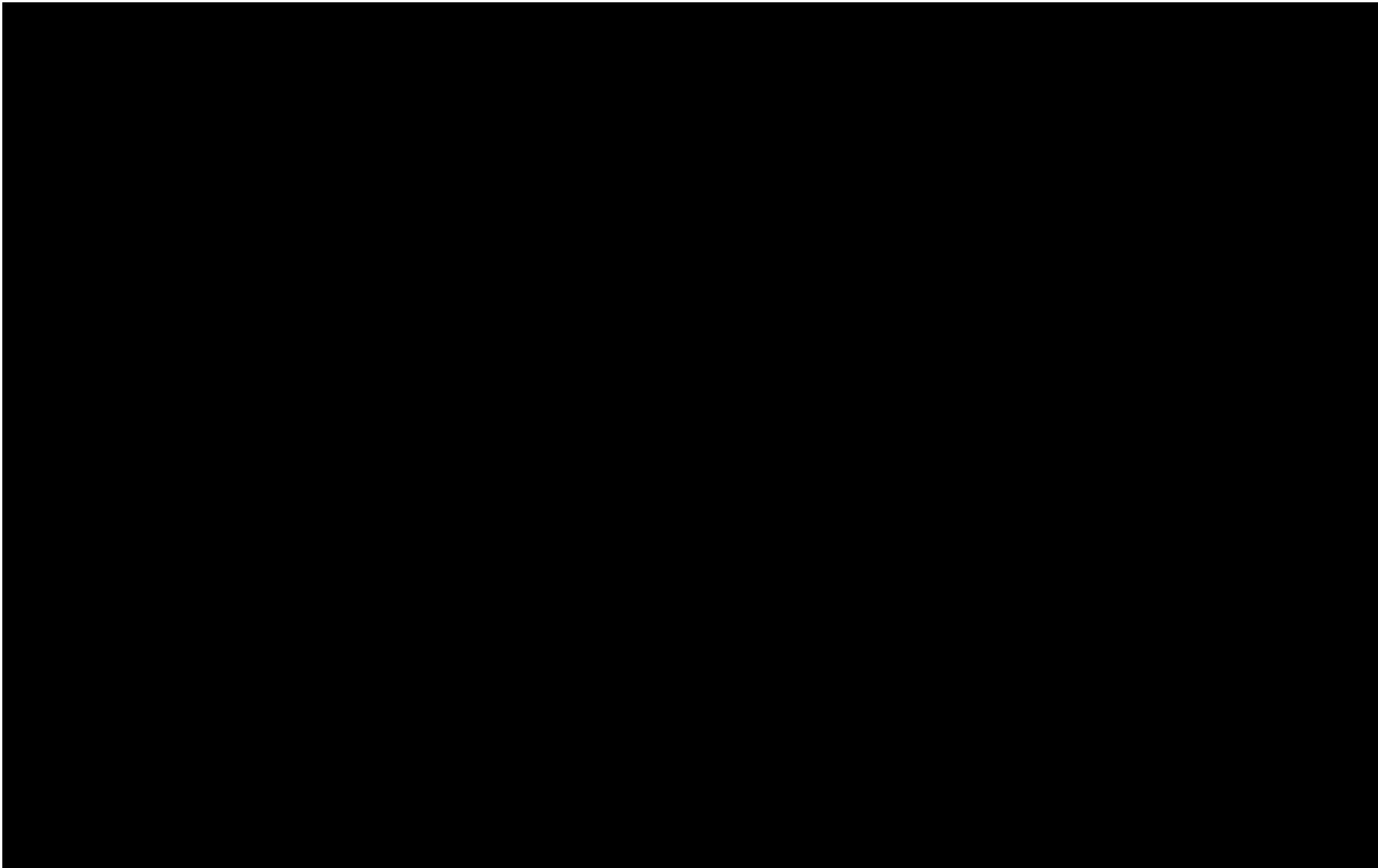
Figure 1-17 – Depth structure map (TVD SS) for the top of the injection zone in the ████████████████.
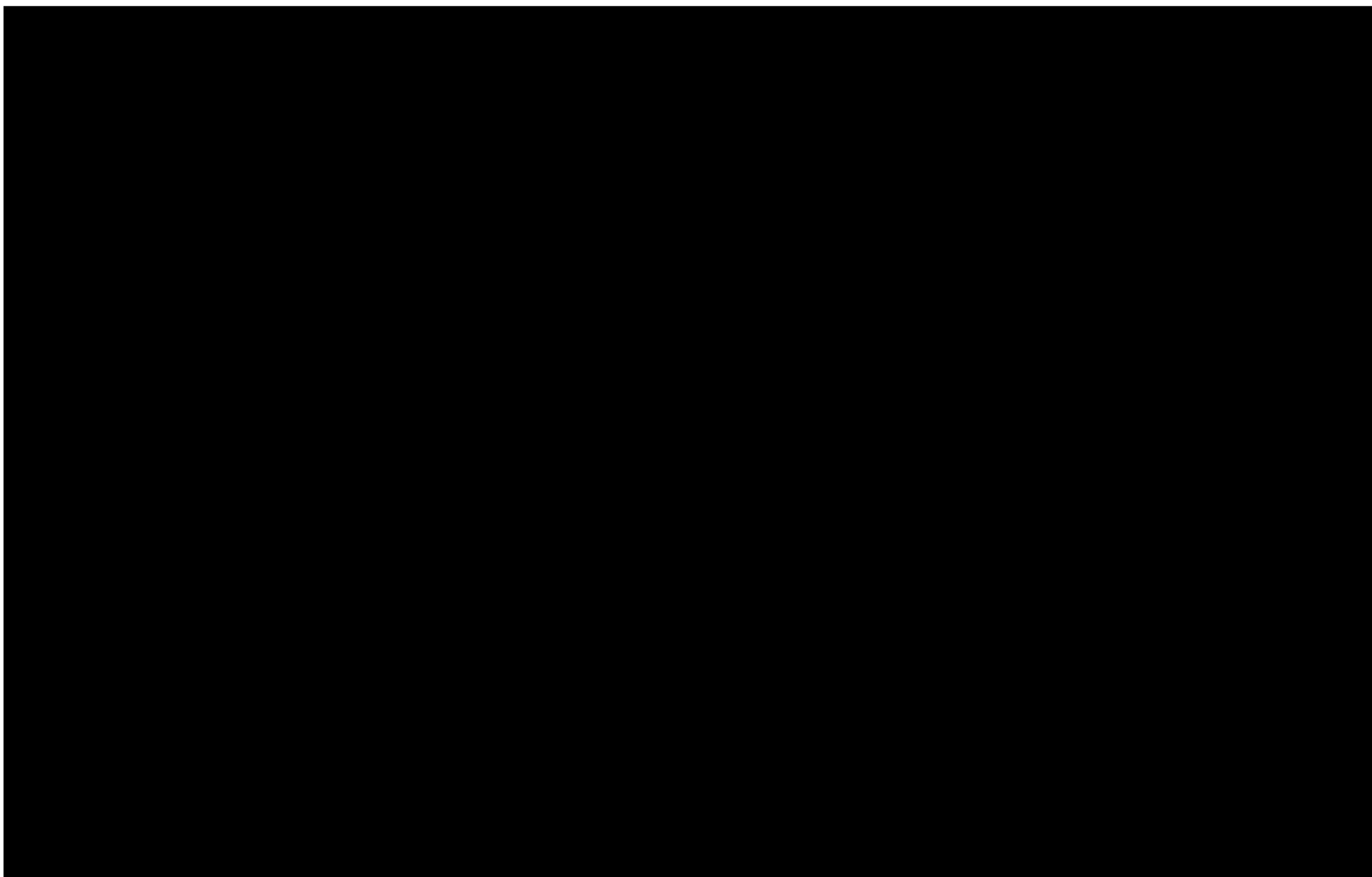
Figure 1-18 – Depth structure map (TVD SS) for the base of the injection zone in the ███
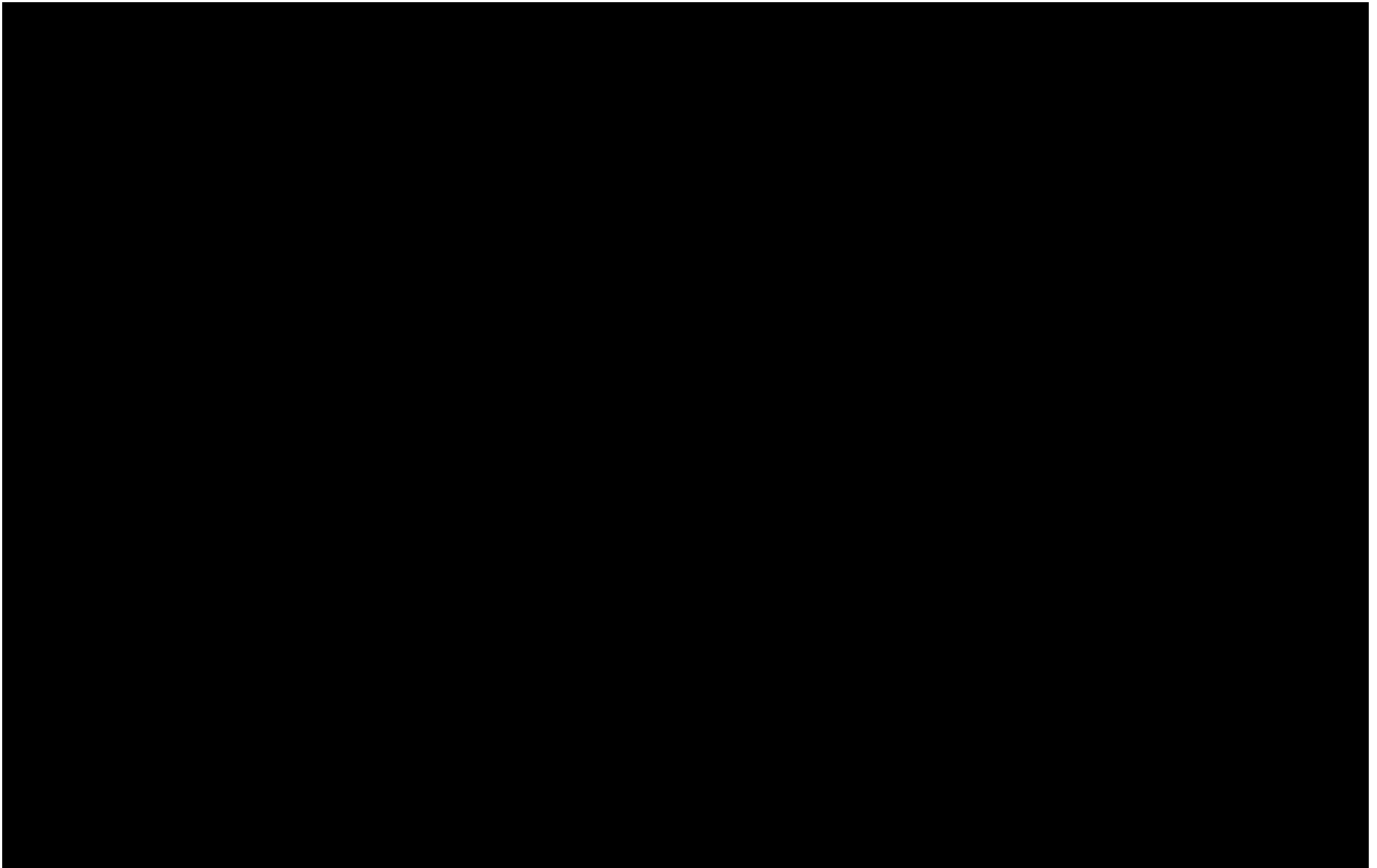
Figure 1-19 – Thickness map (ft) of the injection zone within the ▮▮▮▮▮▮▮▮▮▮▮▮▮▮.
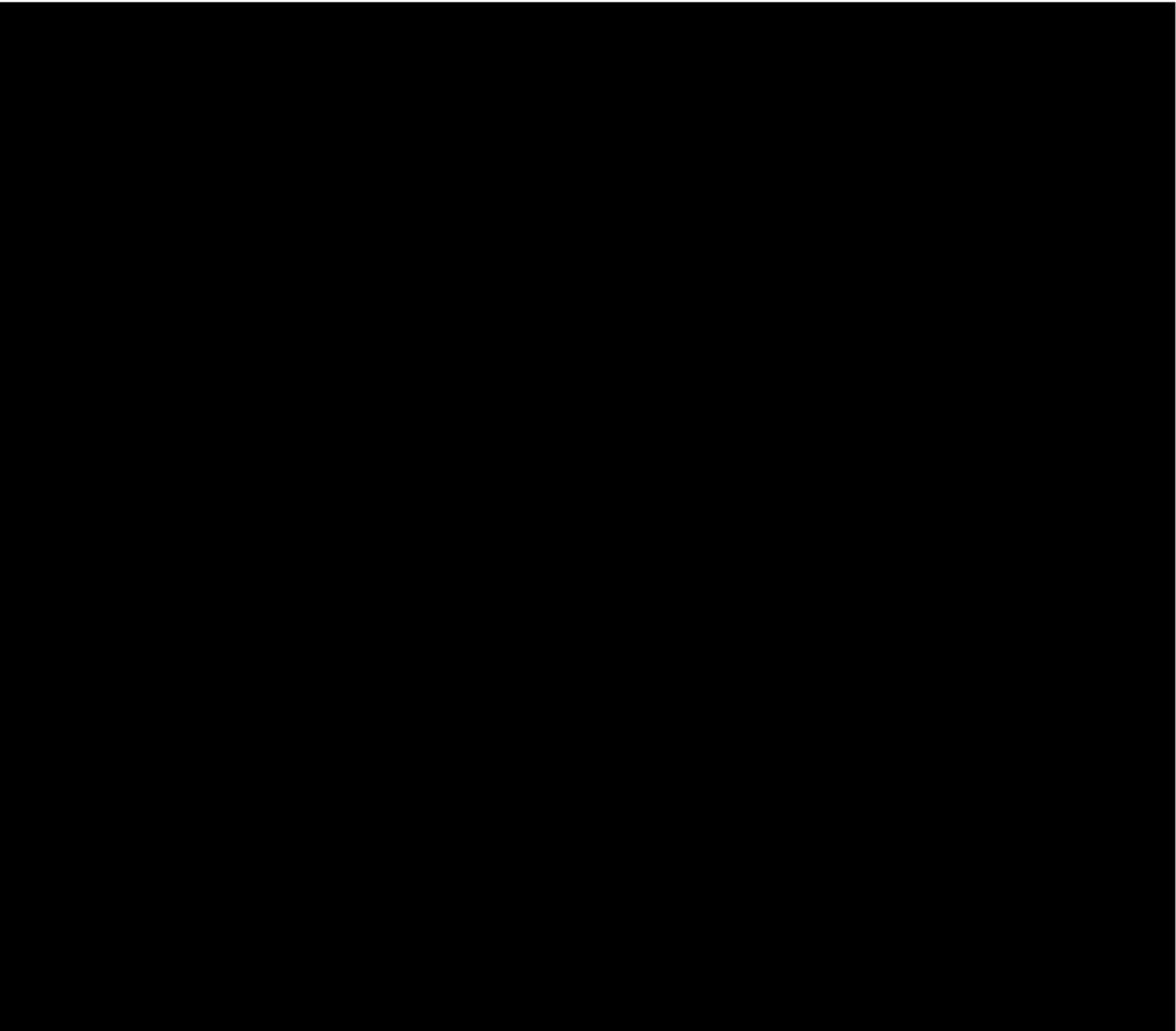
Figure 1-20 – Well log data and petrophysical analysis for the confining zones and injection zone from the type well for the Orchard Project area ████████████████. This well is ███████████ Orchard No. 1–No. 7 by approximately ████. Track 1: @IGR is potassium-thorium (GAPI), and Track 8: v is Poisson's ratio, G is Shear modulus, E is Young's modulus, Sh is horizontal stress, Kb is Bulk modulus, and Biot is Biot's coefficient.
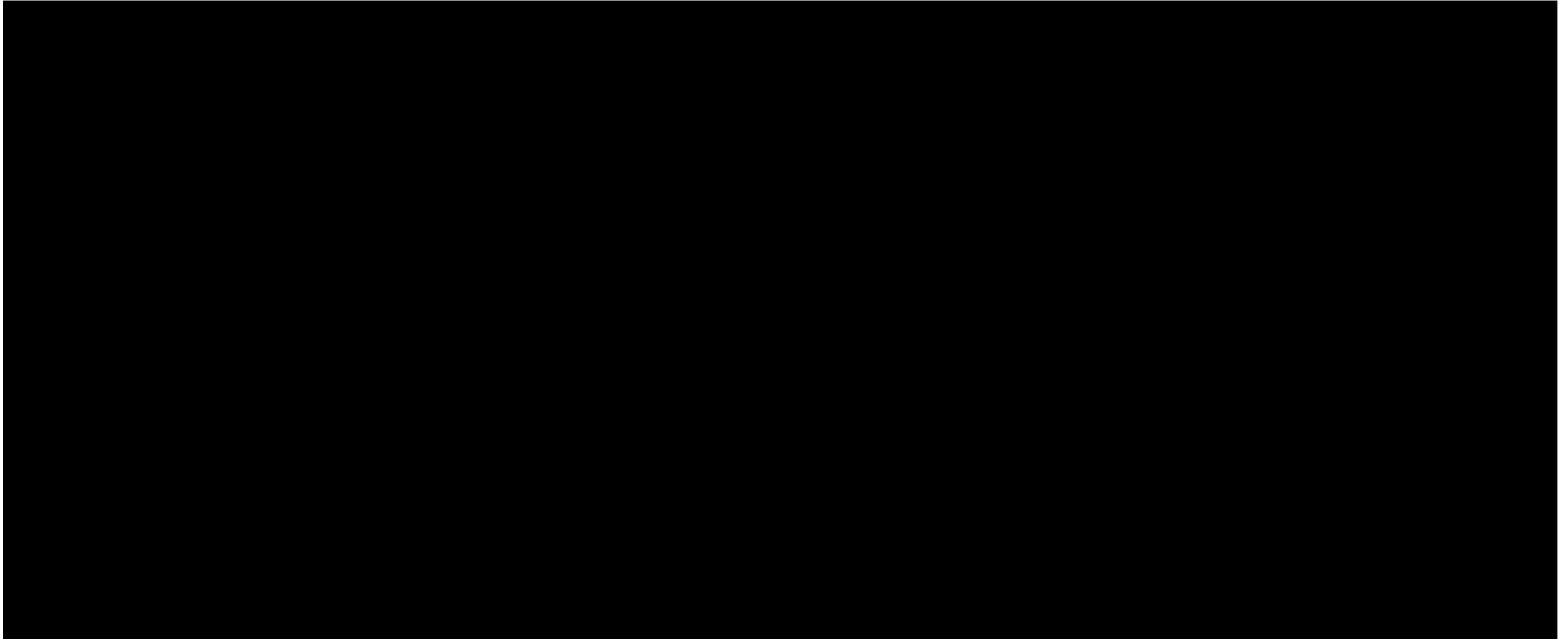
Figure 1-21 – A north-south cross section of well log data from five wells (Figure 1-23 shows the well locations).
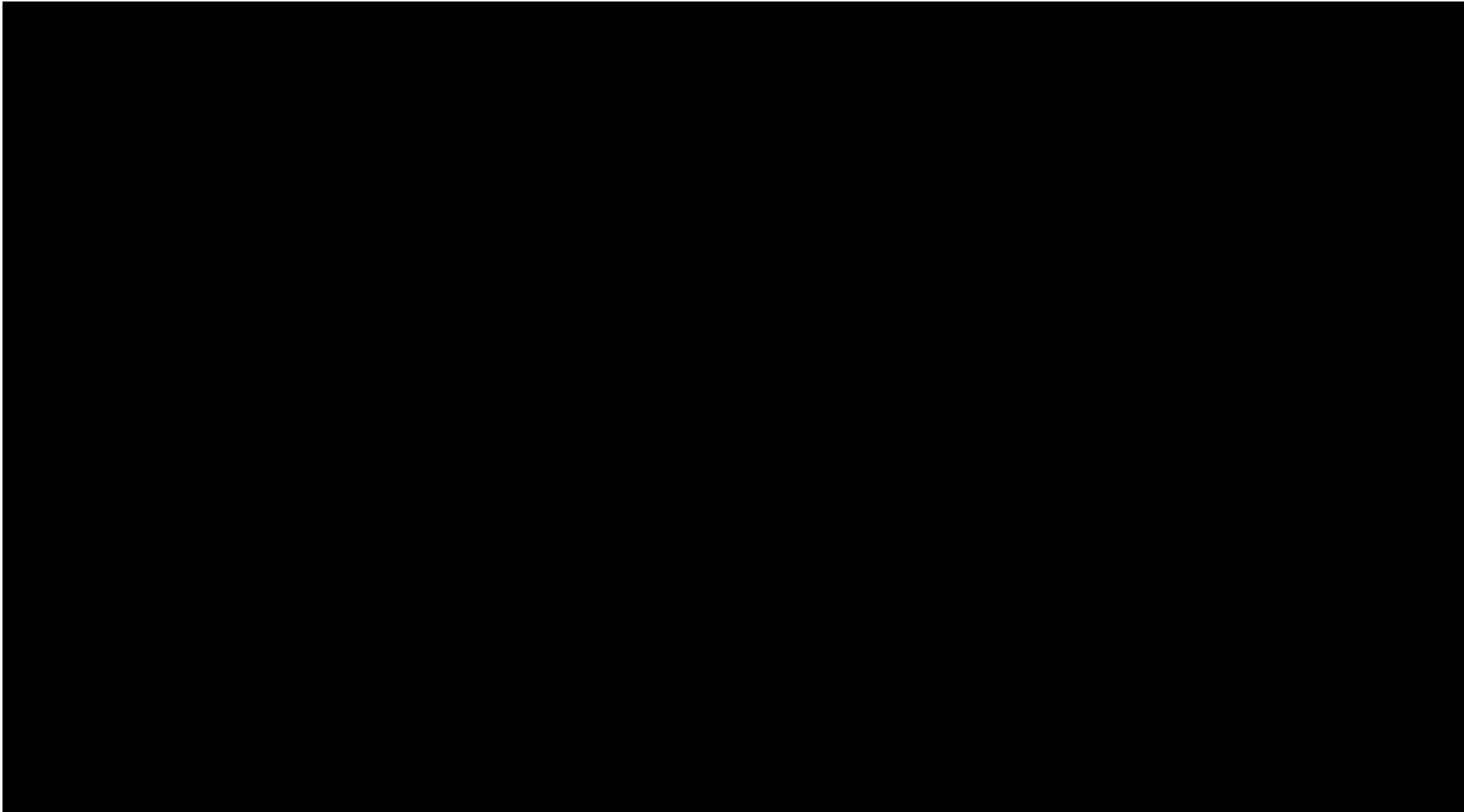
Figure 1-22 – A west-east cross section of well log data from six wells (Figure 1-23 shows the well location
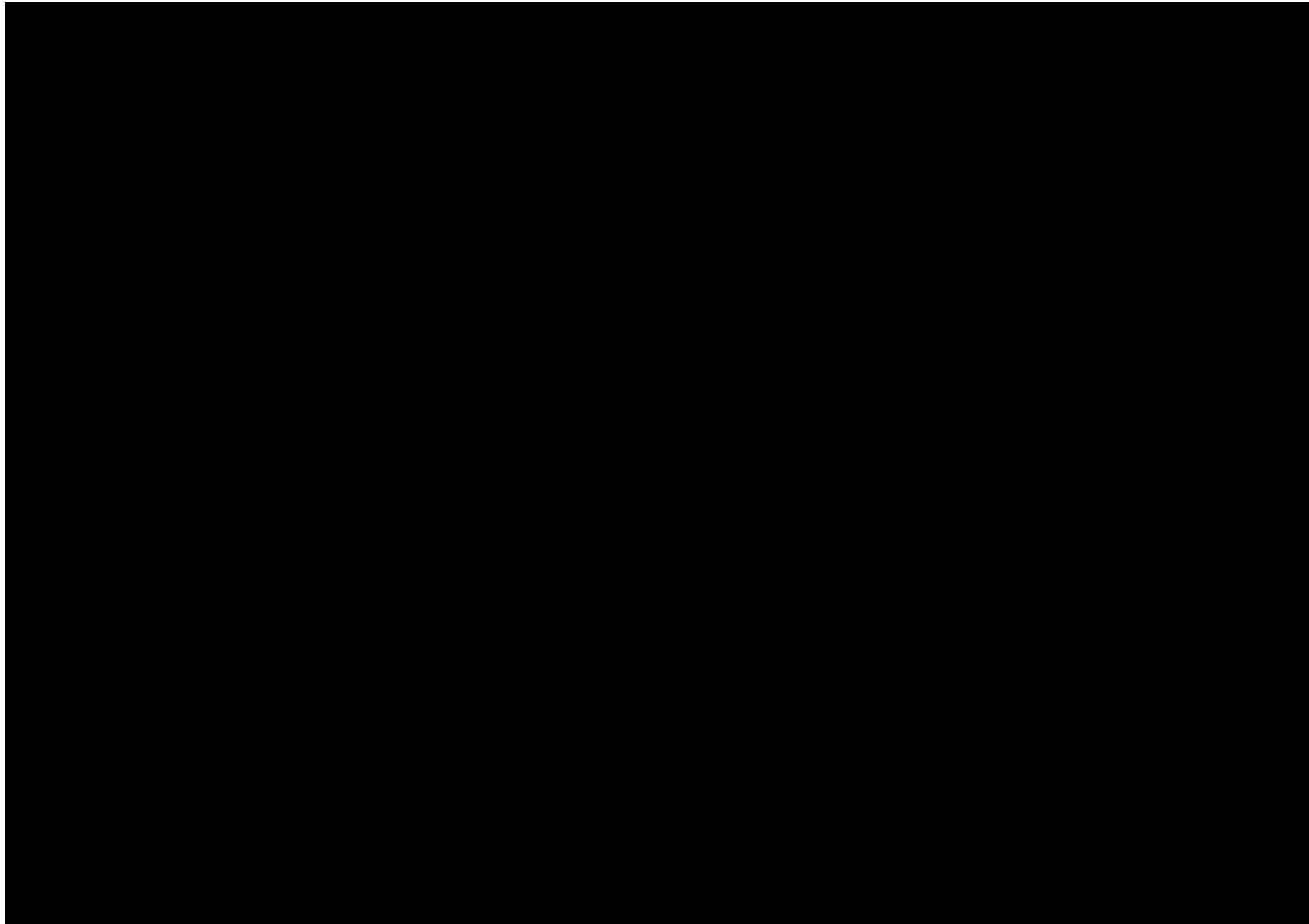
Figure 1-23 – Reference map showing the two cross sections in Figure 1-21 (indicated by the blue dashed line) and Figure 1-22 (green dashed line). The red vertical line indicates the location of the 2D seismic line.

Well tops were selected for the top of the injection zone, primarily where a pronounced inflection of the neutron-density log curves occurred and could be correlated to a neighboring well. This inflection marks the point of significant increase of porosity through to the base of the injection zone compared to the confining zone above. Well tops ██████████████████████████ were commonly selected where the gamma ray increased. A small inflection on the neutron-density log curves indicated a probable sequence boundary. The base of the injection zone was identified by a pronounced decrease of rock quality based on neutron-density changes, increase of (and lack of separation between) resistivity curves, and increasing gamma ray.

Lithology

██
██
██
███
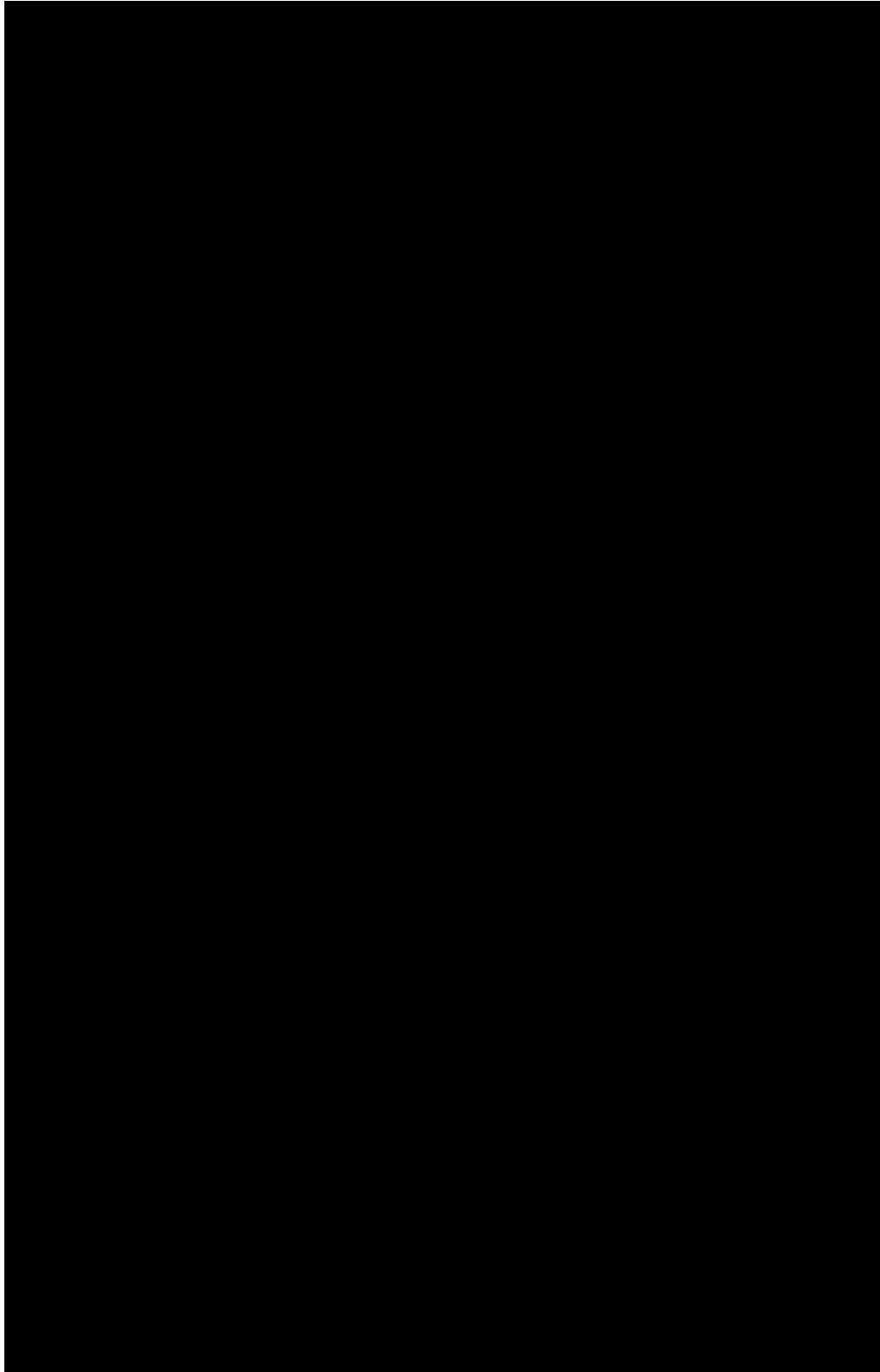
Figure 1-24 – Well log and core data for well ███████████████. Core plugs measured porosity and permeability (air) (indicated by white dots), core "rock types" (multi-colored bands), and mini-permeameter measured permeability (air) (black dots).

General rock types, based on depositional texture and mineralogy observed in the nearby core and fitting into the regional geologic framework, are as follows:
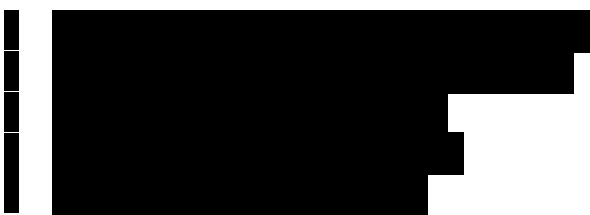
Figures 1-25 to 1-29 show thin-section photographs and interpretations.
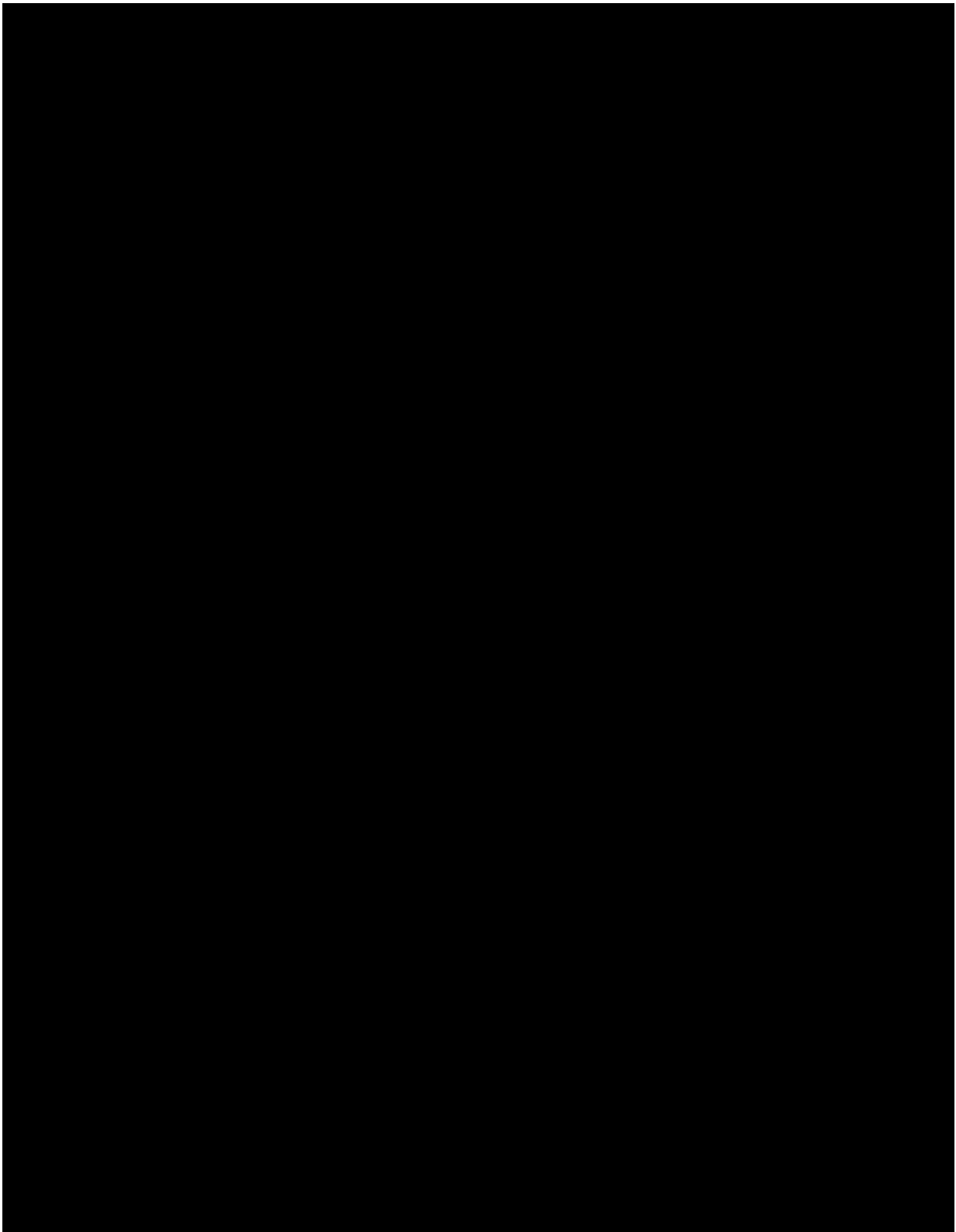
Figure 1-25 – Thin section from well ██ .

Figure 1-26 shows a thin section from
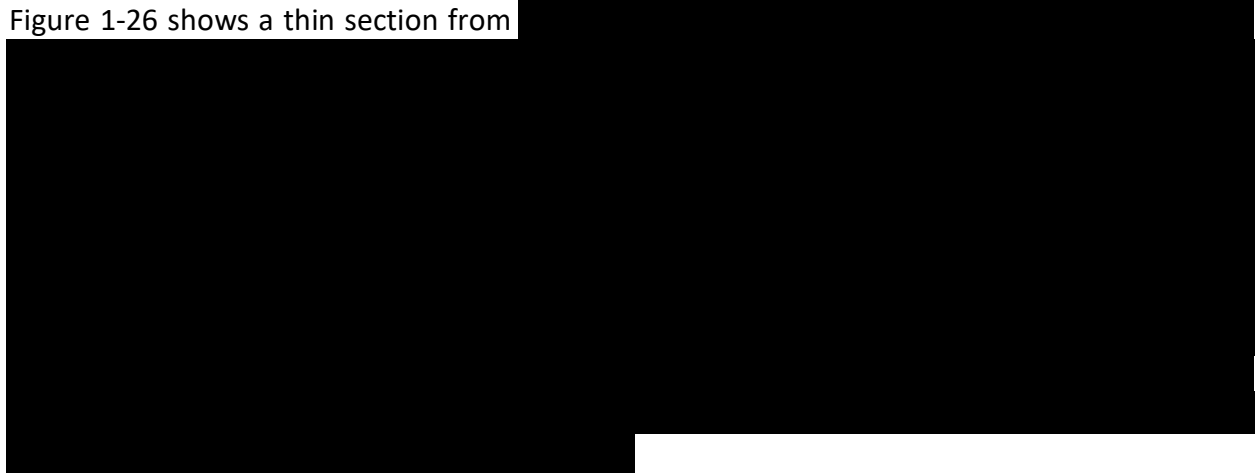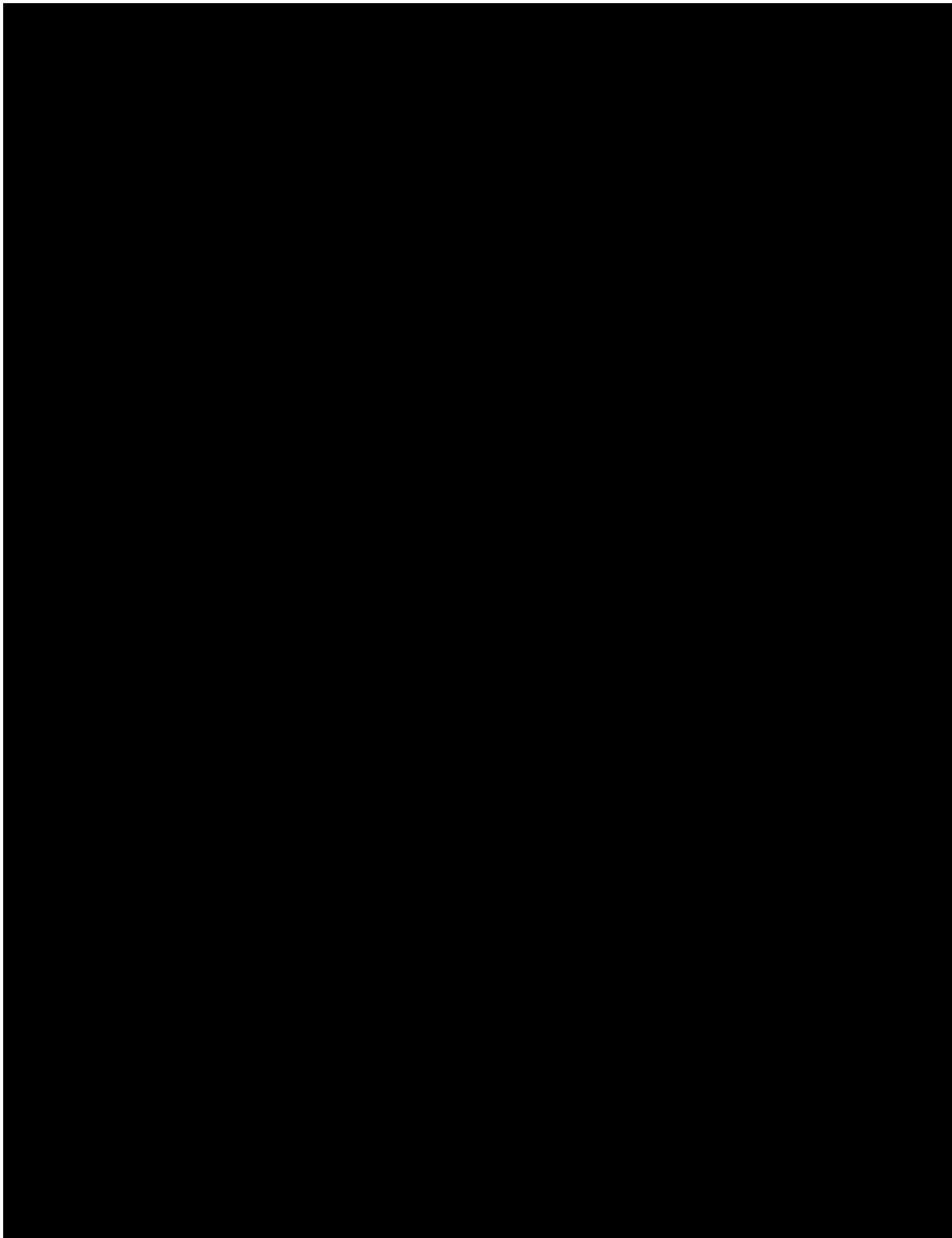
Figure 1-26 – Thin section from well   .

Figure 1-27 shows a thin section from well
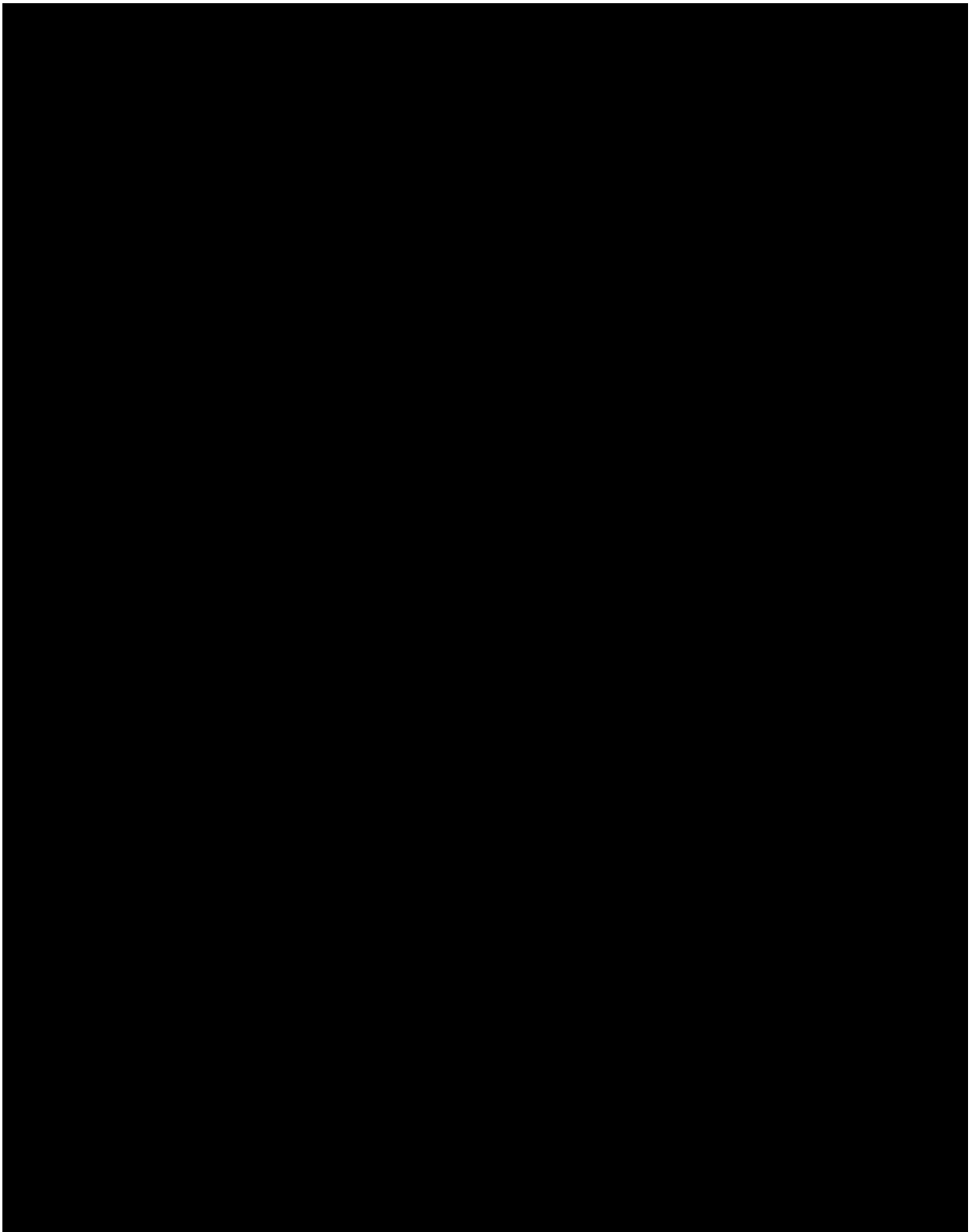
Figure 1-27 – Thin section from well ███.

Figure 1-28 shows a thin section from well
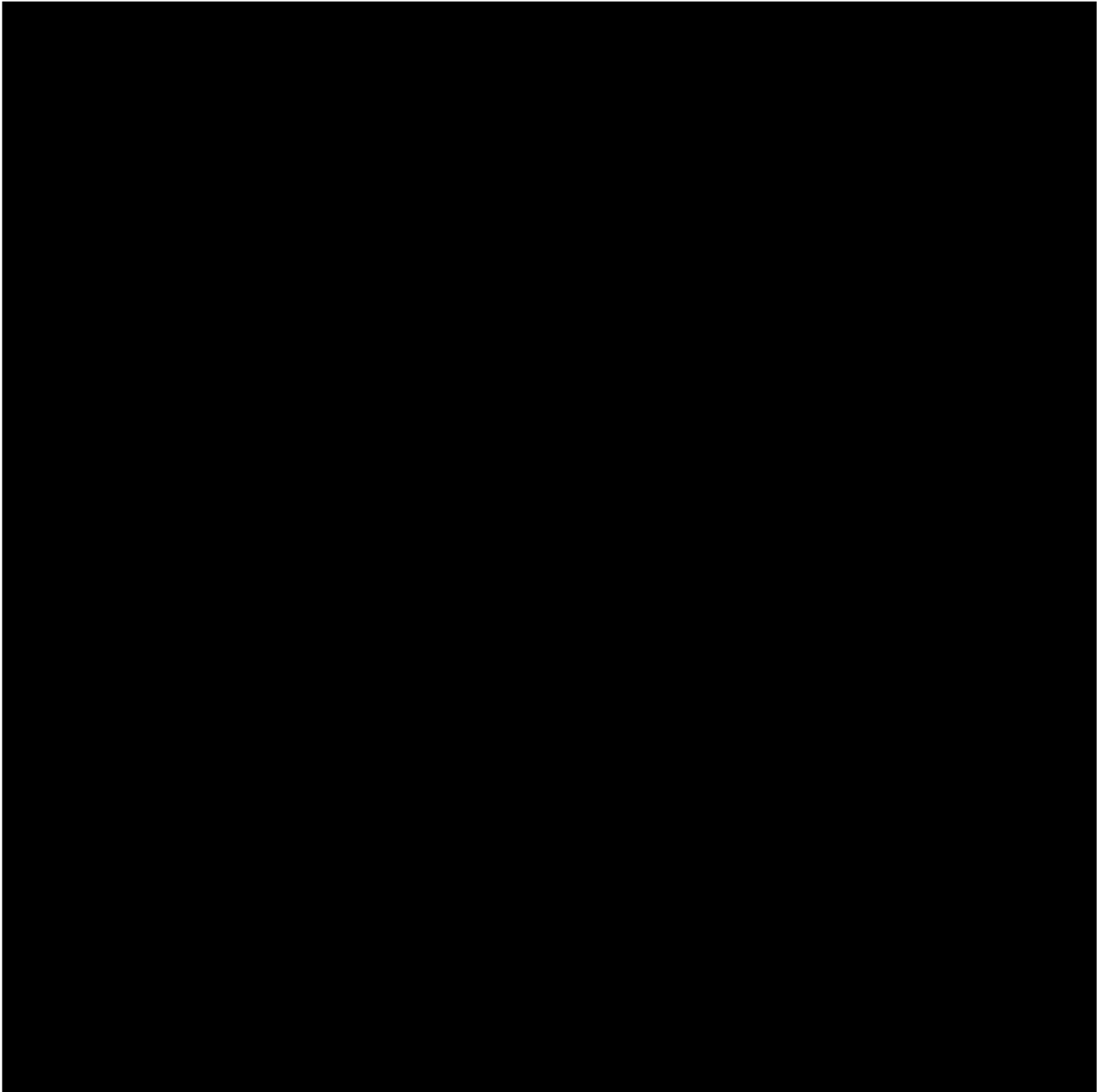
Figure 1-28 – Thin section from well ██████████████████████████████

Figure 1-29 shows a photographed thin section from well
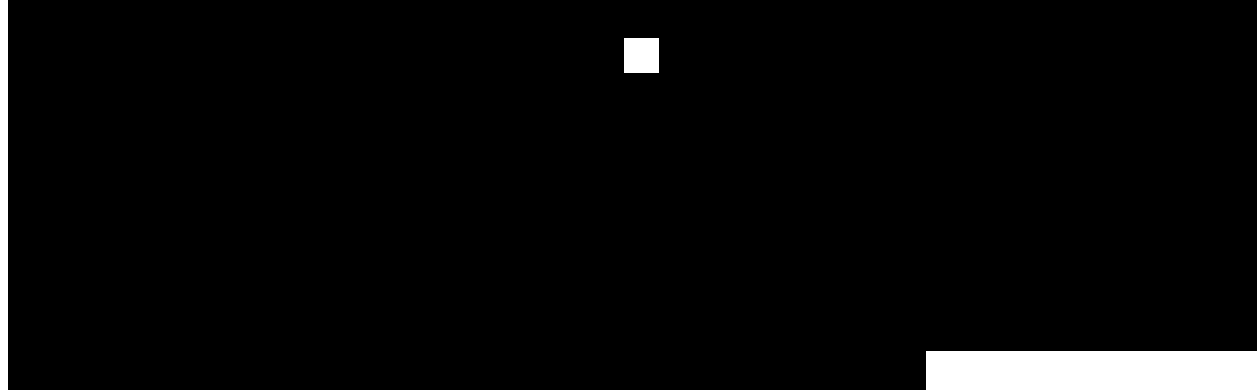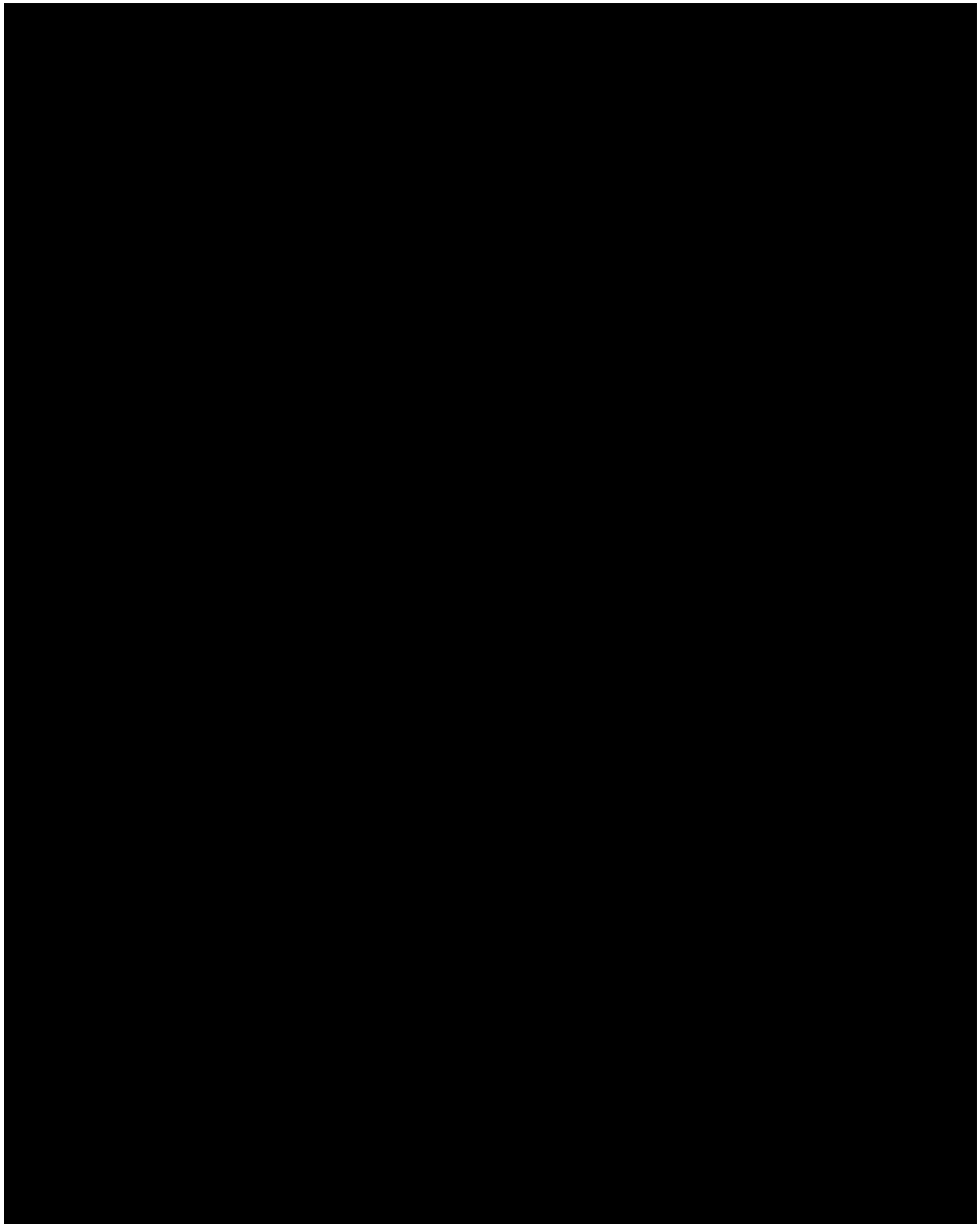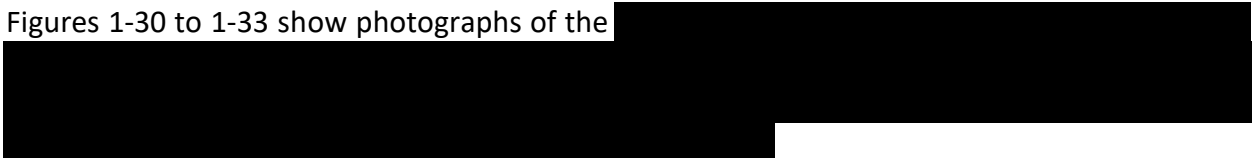
Figure 1-29 – Thin section from well ███.

Figures 1-30 to 1-33 show photographs of the ███████████████████████████████████
██
███
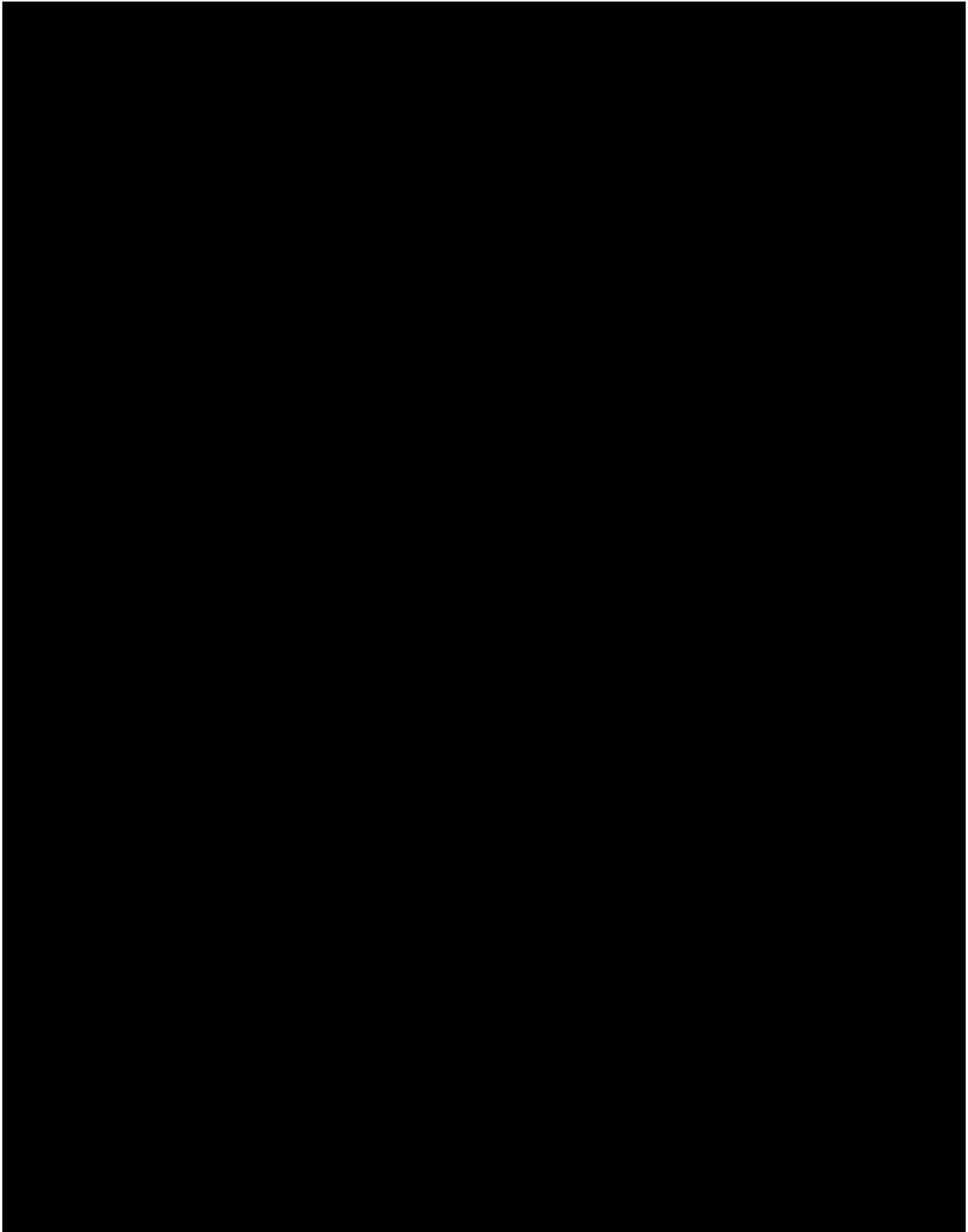
Figure 1-30 – White-light photograph of slabbed core of well ███████████████████
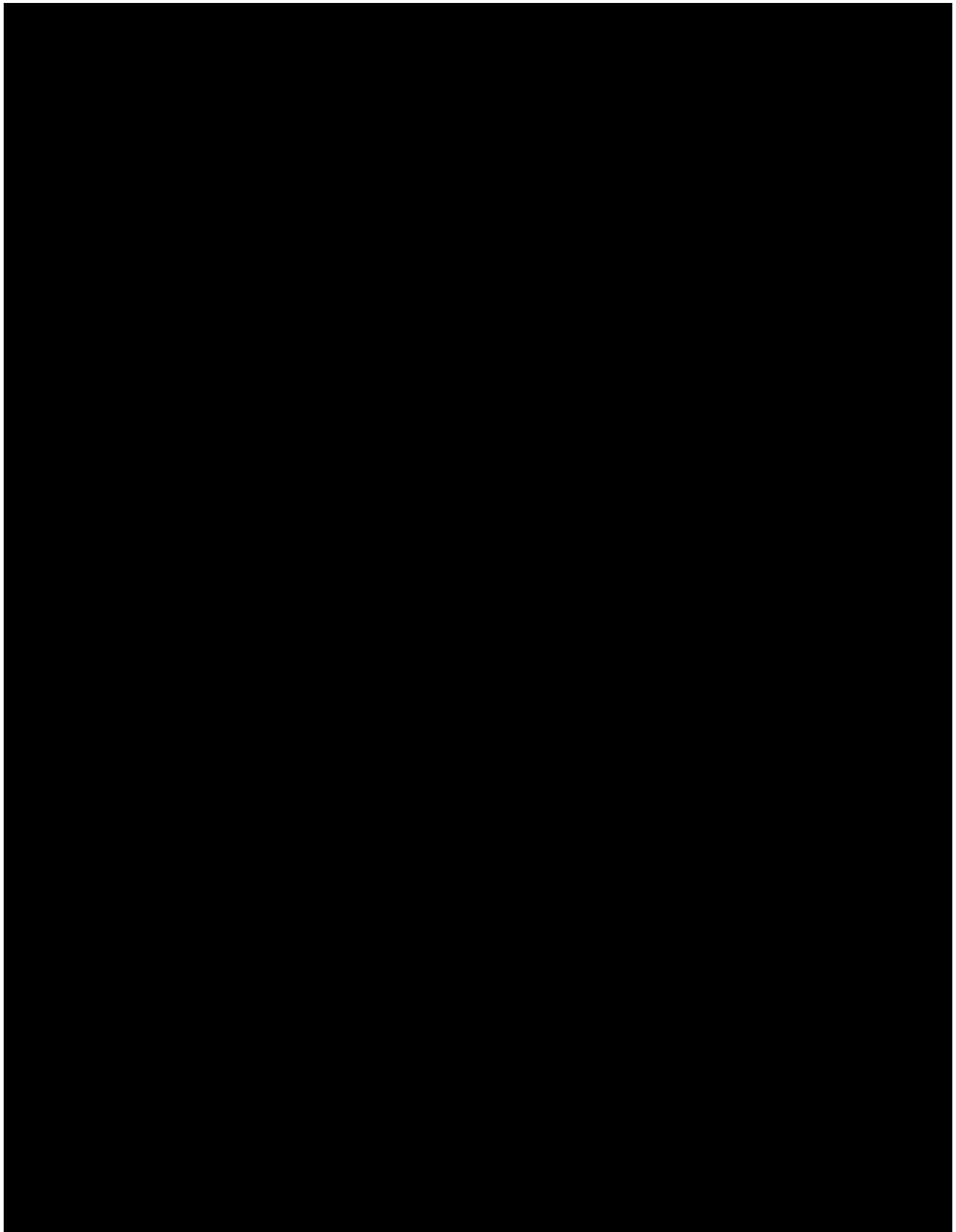
Figure 1-31 – White-light photograph of slabbed core of well ▮▮▮▮▮▮▮▮▮▮▮▮▮▮▮▮▮▮▮▮▮▮▮▮▮▮▮▮▮▮▮▮
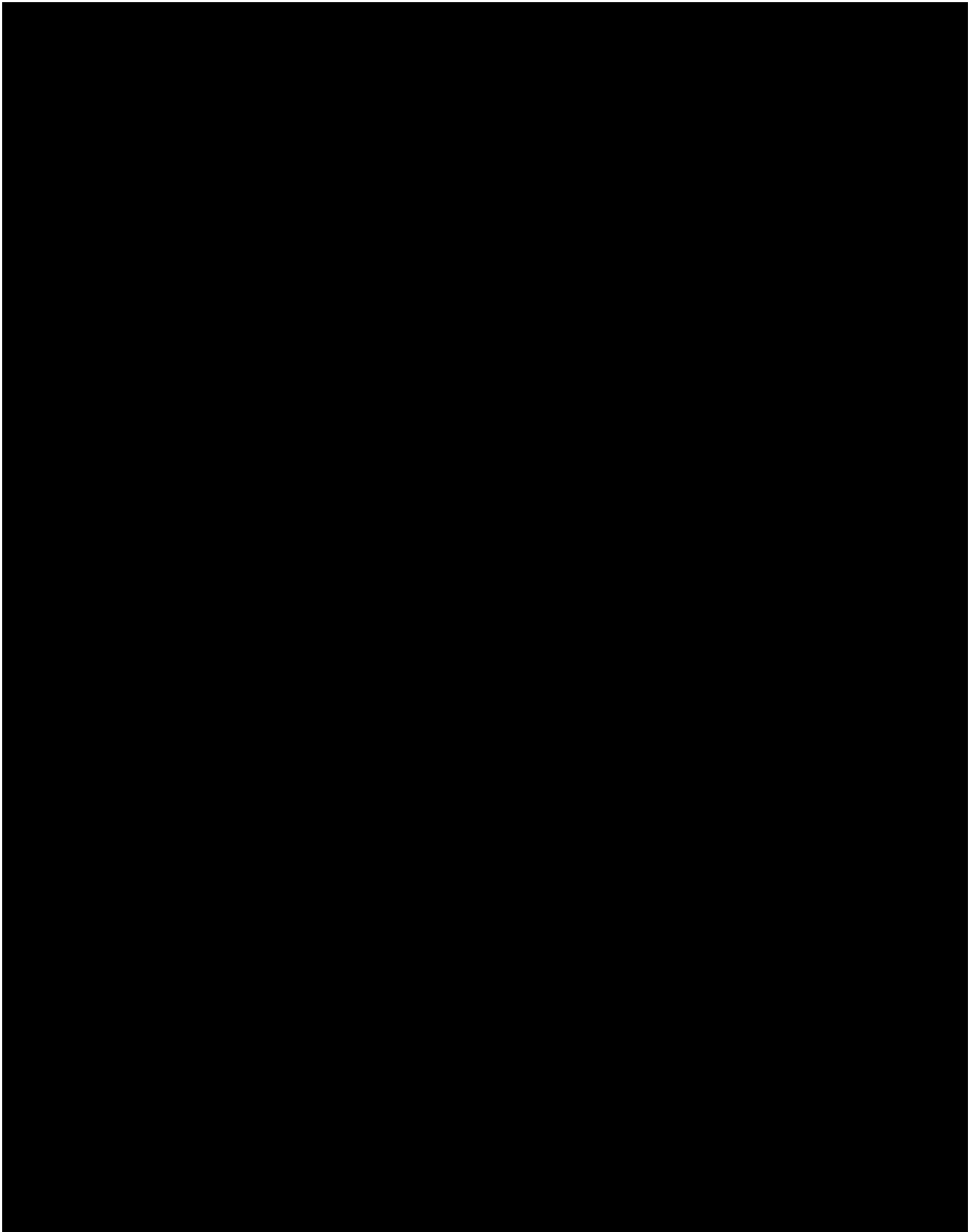
Figure 1-32 – White-light photograph of slabbed core of well ▮▮▮▮▮▮▮▮▮▮▮▮▮▮▮▮▮▮▮▮
▮▮
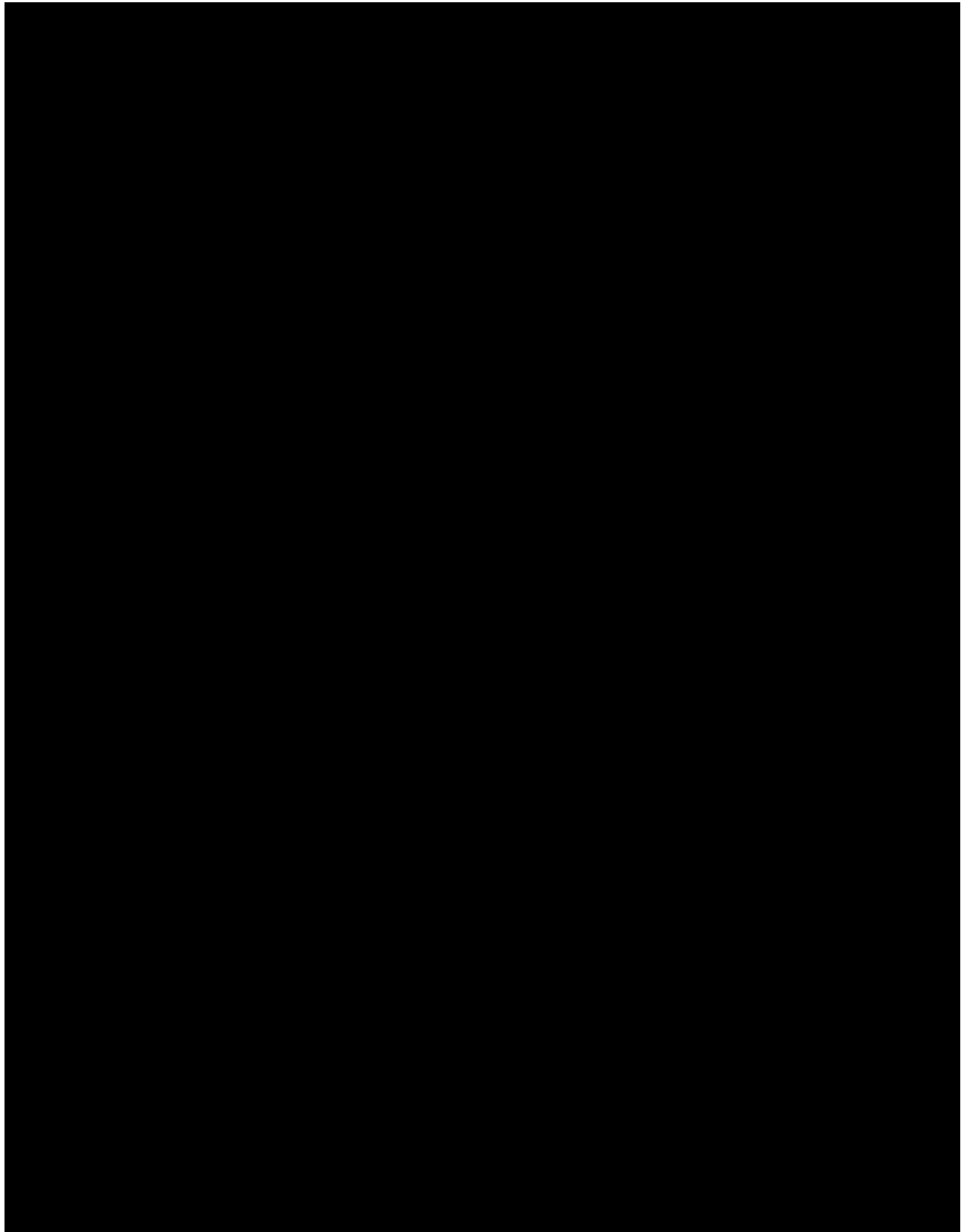
Figure 1-33 – White-light photograph of slabbed core of well ███████████████████████

Well log data shown in the type well ███████████████ was quantitatively used to understand the dominant lithology in the ██████████. Other well data were used to qualitatively understand whether the dominant lithology in the injection zone is ██████████████. These learnings came from observing the neutron-density separation and overlap and the photoelectric factor log curve (where available).

Further refinement of the petrophysical model to derive dominant lithology or facies is discussed in *Section 1.10.*

Porosity
Density porosity was derived using the bulk density log and an estimated matrix density for the

██
██
██
█████████████████████████████████

Minimal correction was needed for shale (i.e., clay and silt) effects based on the very low potassium-thorium gamma ray log values. Uranium is the main driver for relatively higher (10-30 GAPI) gamma ray values (i.e., total and effective porosity are treated similarly). Uranium is often diagenetic and unrelated to depositional facies or rock fabric (Lucia, 2007).

██
██. For comparison purposes only, the mineralogy log curves generated for the type well were used to calculate an effective porosity (PHIE). Shale proportions based on gamma ray and generic corrections were applied to PHIE before calculating XPHI. The resulting average well-log porosity for the type well is █████████████████████████████ injection interval.

Figure 1-34 shows an average porosity map for the ████████████████████ injection zone. This interval (as shown in *Section 1.2.4*) is the main target for CO_2 injection, based on having a higher pore volume than the ██████████████. The spatial distribution of porosity was mapped using the XPHI well log. The porosity within the Orchard Project area is expected to be relatively consistent based on observations between wells surrounding the project area (e.g., █████████ ████████████████████████████████ This average porosity map was extracted from the 3D numerical model, created via kriging methodology to distribute porosity between upscaled well log data, as discussed in *Section 3 – Area of Review and Corrective Action Plan*.
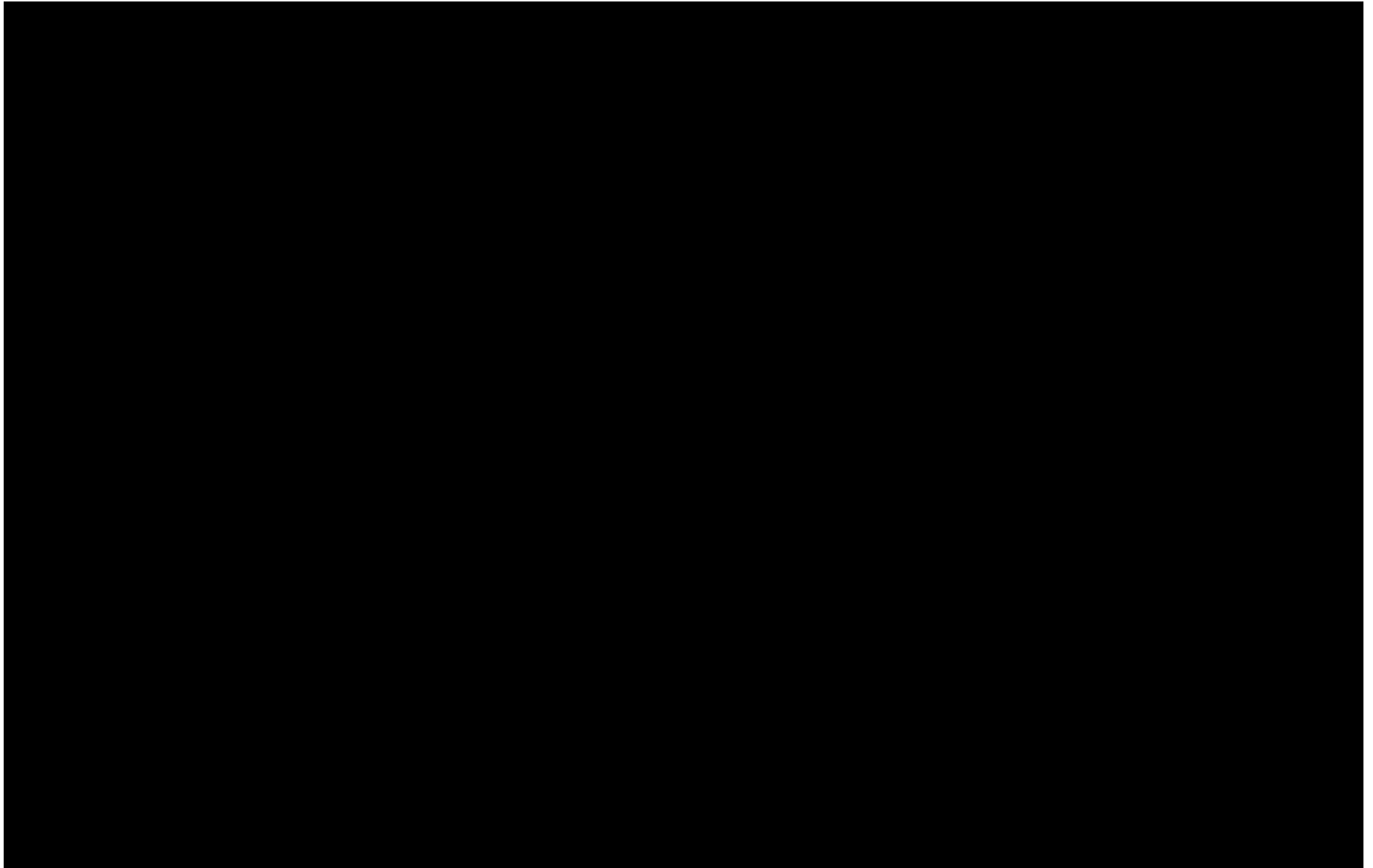
Figure 1-34 – Average porosity map of the ███████████████████ injection zone.

The average porosity map indicates several changes outside of the Orchard Project area. ■■

■■■
■■■
■■

Core plugs were acquired, and 28 conventional porosity and permeability measurements (in both ambient and stressed conditions) were taken in the Orchard Project area. Table 1-3 shows the results of conventional plug analysis for well ■■■■■■■■■■. Samples ■■■■■■■■ are vertical plugs, and the remainder are horizontal. The complete core analysis report for this well is provided in Appendix J-2.

Table 1-3 – Results of conventional plug analysis for well ■■■■■■■■■ (Appendix J-2, pg 22).

X-ray diffraction results showed ██████████████████████████████████████ ████████████████████ injection zone. This may correlate to the low total gamma ray well-log expression observed in the cored well and other nearby wells. Discussion of rock mineralogy continues in *Section 1.6*.

██
██
██
██████████████████████████████ No major dissolution porosity, connected vuggy pore types, or preexisting large-scale fracture porosity is predicted to interfere with CO_2 injection in the project area.

Permeability (Horizontal)
The average calculated matrix permeability for ████████████████████████████ ██. Permeability was derived using ████████████████████████████ estimation method. A continuum of rock-fabric numbers, or petrophysical classes, can relate interparticle porosity and permeability using a global transform representative of grain size and sorting for ████████████████████████████ ████ This permeability estimate will be confirmed once the wells are drilled.

Figure 1-35 shows the continuum of rock fabrics and associated porosity-permeability transforms: ██
██
██
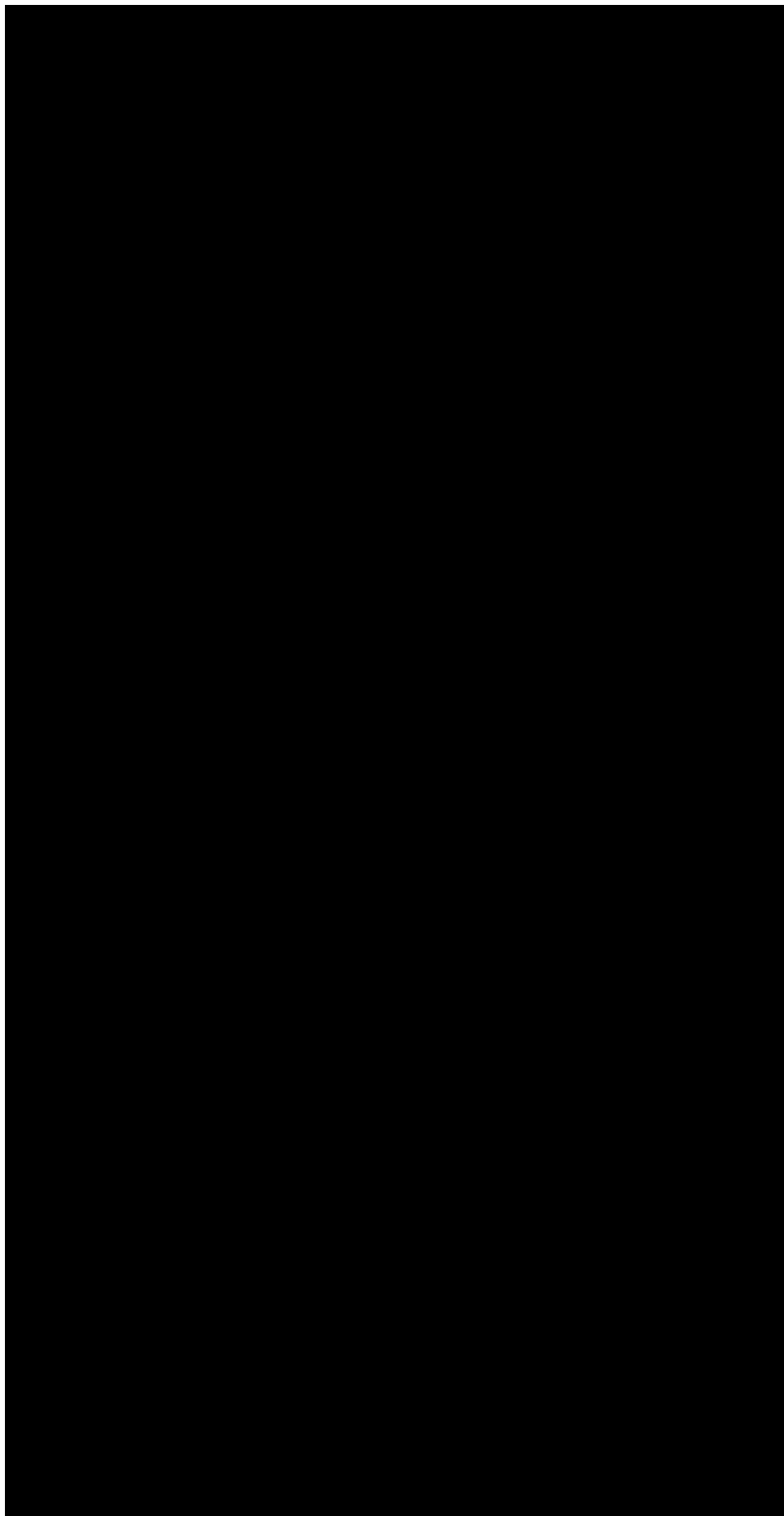
Figure 1-35 – The continuum of rock fabrics and associated porosity-permeability transforms:

The basis for designing two permeability scenarios was the regional geologic model for the possible range and dominant lithofacies expected in the ███████████████████████ ███ █████████████████

Figure 1-36 shows a chart of core-plug porosity versus permeability (air) measurements for well ████████████████ Points are colored by "rock type" interpretations from the slabbed core description. Table 1-4 shows the permeability, determined using the pressure-decay profile permeameter (Core Lab Houston).
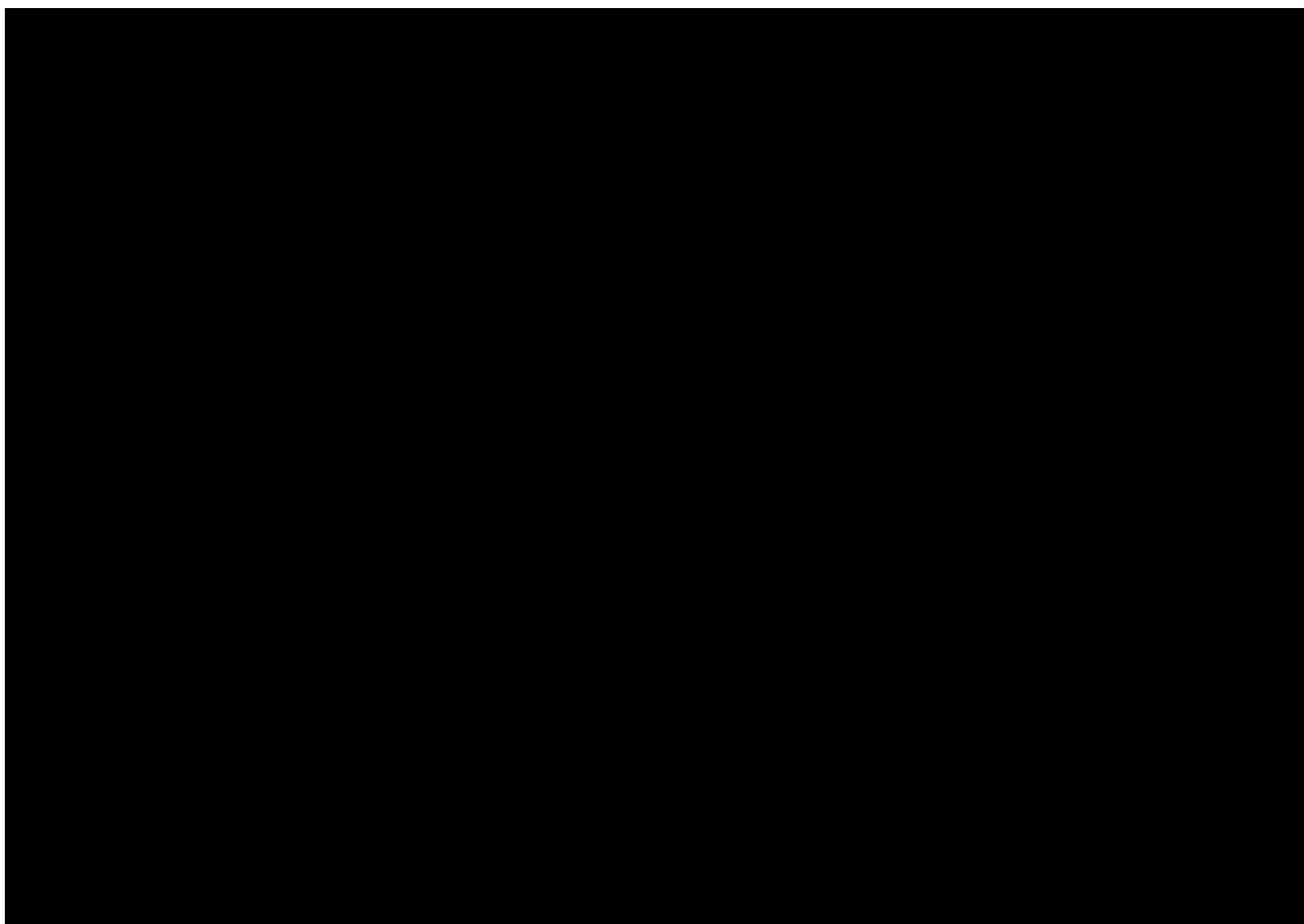
Figure 1-36 – A chart of core-plug porosity versus permeability (air) measurements for well ███████████████. Points are colored by "rock type" interpretations from the slabbed core description.

Table 1-4 – Permeability determined using the pressure-decay profile permeameter ████████

Depth (ft)	Ka (mD)	Core	Oil-Staining Intensity (0 is lowest)

The ████████ for the 3D numerical model permeability for area of review (AOR) delineation was ██ No correction was applied to porosity used for calculating permeability ████████████████ as porosity is treated as equal to interparticle porosity. ████████████████████

Permeability measurements using the pressure-decay profile permeameter provided an understanding of the possible permeability ranges for the 60 ft of the available core at the top of the injection zone. Samples were taken every 2 ft along the slabbed core. ██████████

██
██
██████████

Residual oil staining was observed in person on the core as well as in the white-light photographs. These "high intensity" oil-staining occurrences correlate to the core description of the rock types, where grain-rich rocks represent higher permeability than mud-rich sections.

Conventional porosity and permeability measurements of 22 plugs (28 measurements total) demonstrated a similar set of results as was described in Table 1-3. Permeability measurements (both stressed and unstressed) plotted closer to ██████████, based on their measured porosity values. Most samples reflect lower porosity than average well-log-derived values for the ██████████, which may be attributable to the core being from the lower porosity 60 ft at the top of the injection zone. ███████████████████████████████████
██, based on well logs in the Orchard Project area.

Permeability (Vertical)
Vertical permeability is an order of magnitude lower than horizontal permeability in ████████
███
██████████. The ratio between vertical and horizontal permeability (kv/kh) for ████████
██
███ Permeability estimates will be confirmed once the wells are drilled.

██
██
██████████████████████

Water Saturation
The Orchard Project area is absent hydrocarbon production due to the migration of hydrocarbons out of the area, therefore leaving behind a residual oil zone. Water saturation was derived using Archie's methodology as follows:

$$Sw^n = ((a*Rw)/(Rt*phi^m))$$

    Where:
    Sw = water saturation
    n = saturation exponent

a = tortuosity factor

m = cementation exponent

Rw = resistivity of formation water at formation temperature

Rt = resistivity of the formation.

Figure 1-37 shows the mud-log gas readings and the petrophysical water-saturation well log derived using that Archie equation, while Figure 1-38 shows a snapshot of the mud-log sample description and gas readings for well ▮▮▮▮▮▮▮▮▮▮▮.
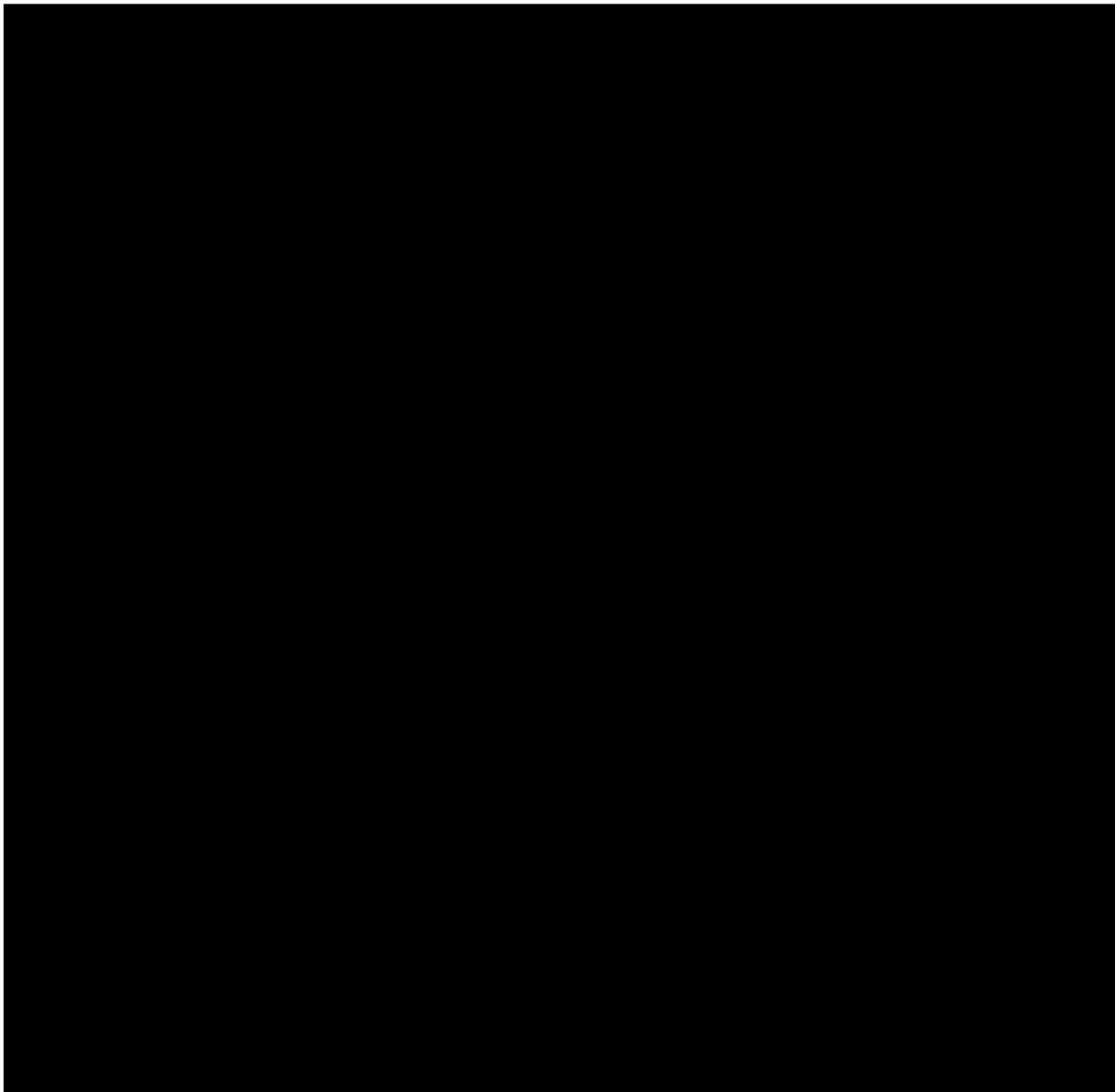
Figure 1-37 – Mud log gas readings (second track from the right) and the petrophysical water-saturation well log derived using Archie's methodology (last track) for well ███████████.
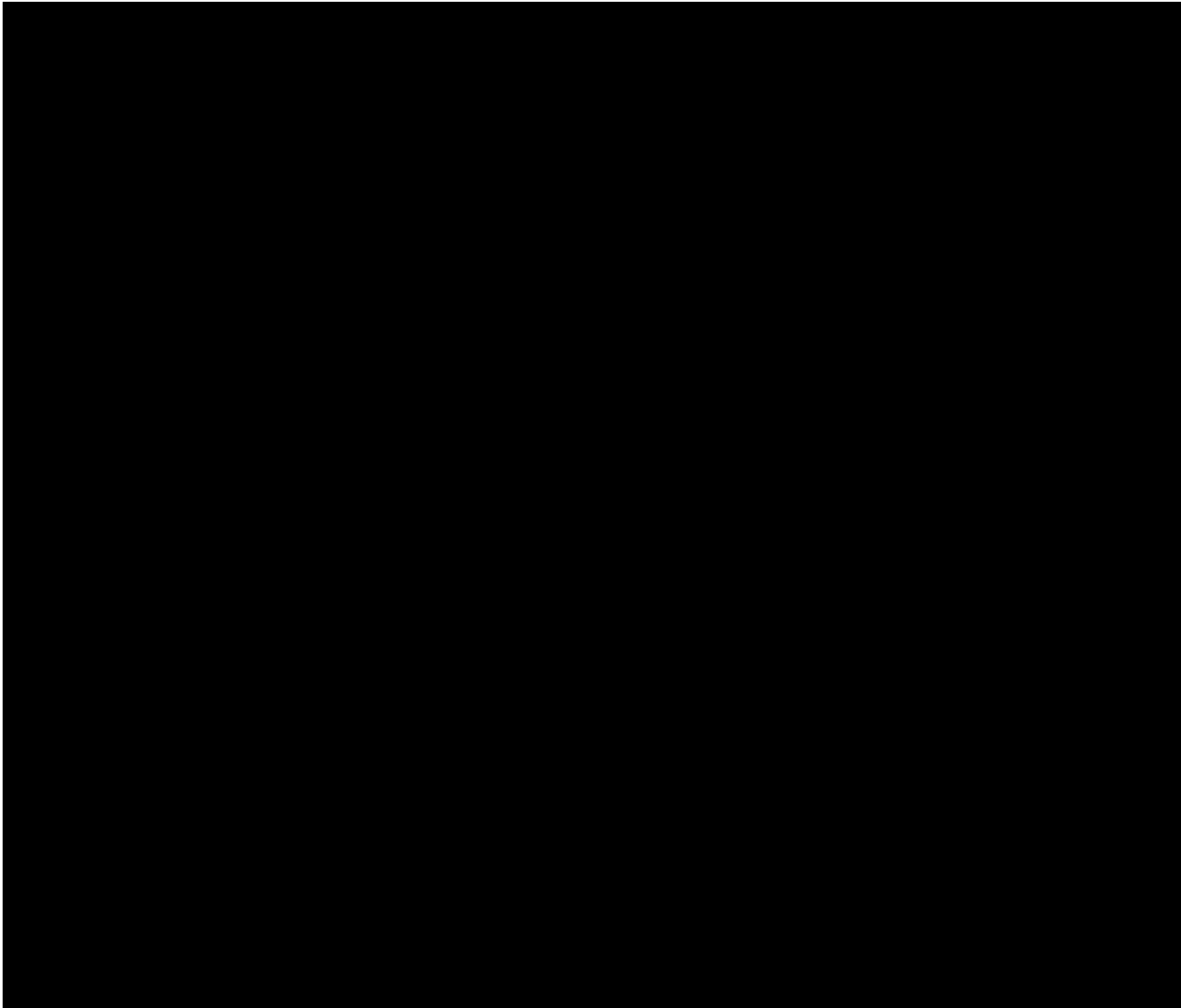
Figure 1-38 – A snapshot of the mud-log sample description and gas readings for well ███████████████ .

The average water saturation in the ████████████████████ injection zone is approximately 60% based on the petrophysical calculation. The rest of the San Andres injection is treated as having 100% water saturation based on the high calculated water-saturation values. ████████ ████████████████████████ correlate to the top portion of the injection zone having the lowest calculated water saturation. ████████████████████ ████████████████████████ of the Orchard Project area also show similar ████████████████████ in the equivalent interval in the ██ ████████ zone.

A discussion of how the water saturation is accounted for in the 3D numerical model is presented in *Section 3 – Area of Review and Corrective Action Plan*.

Table 1-5 compares the different sets of Archie parameters.

Table 1-5 – Comparison Between Two Different Sets of Archie Parameters

Archie Parameter	
a	
m	
n	
Rw	

1.3.3   Primary Upper Confining Zone

The top portion of the ██, comprise the primary confining zone overlying the injection zone. The combined thickness of the Upper ████████████████████ confining zone is ████████████████████ in the Orchard Project area. The top and bottom depths are approximately ████████████████████████, respectively.

Figure 1-39 shows a depth structure map for the top of the upper confining zone ████████████ ████████████████. (For reference, Figure 1-17 in *Section 1.3.2* showed a depth map of the base of the confining zone (top of the injection zone)). Figure 1-40 shows a thickness map of the ████

confining zone. Figure 1-41 is a structure map of ████████████████. Figure 1-42 shows a thickness map for the ████████ and Figure 1-43 is an isopach of the ████████████████ ████████████ confining zone.
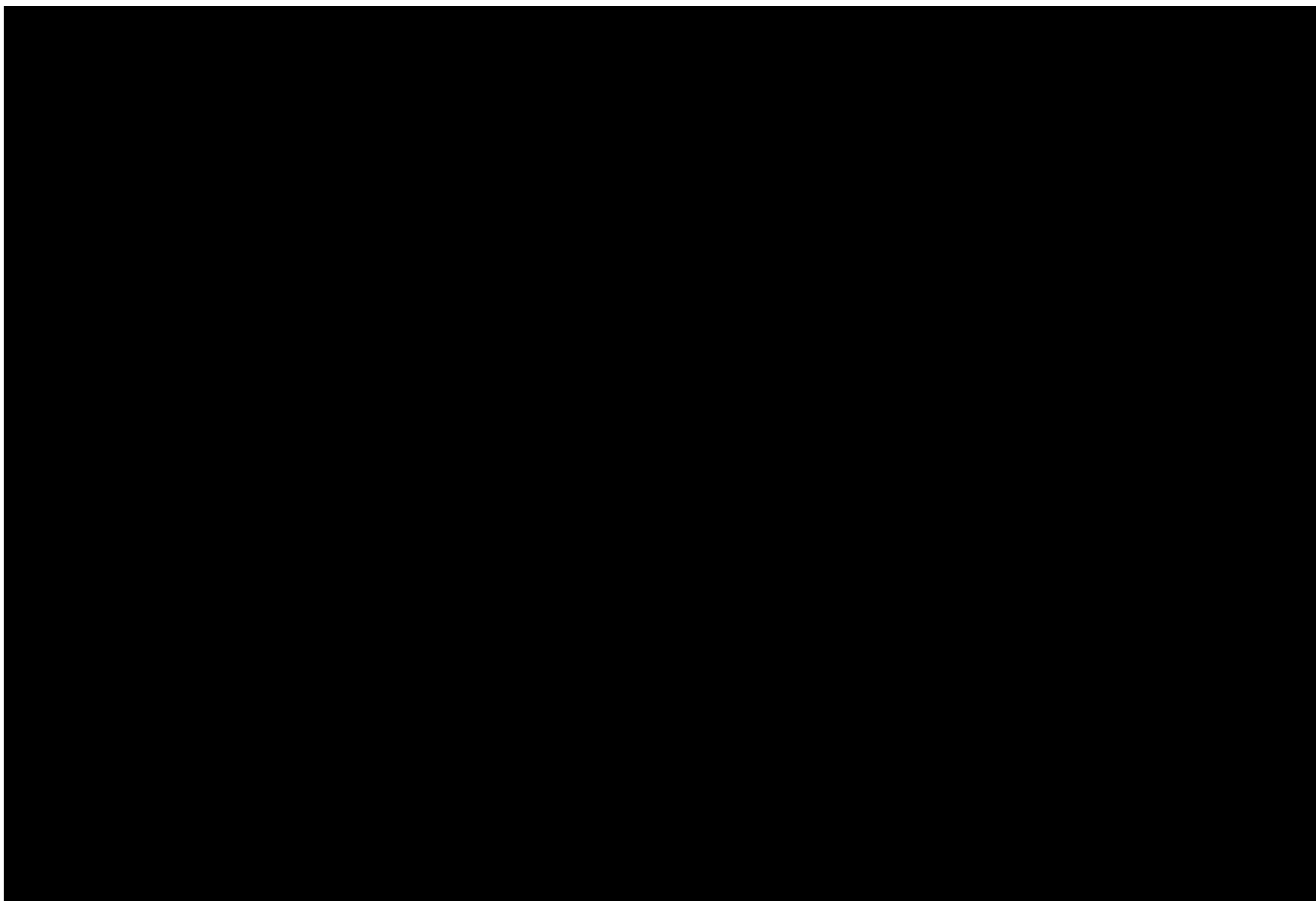
Figure 1-39 – Depth structure map (TVD SS) for the top of the upper confining zone ████████████████████████████
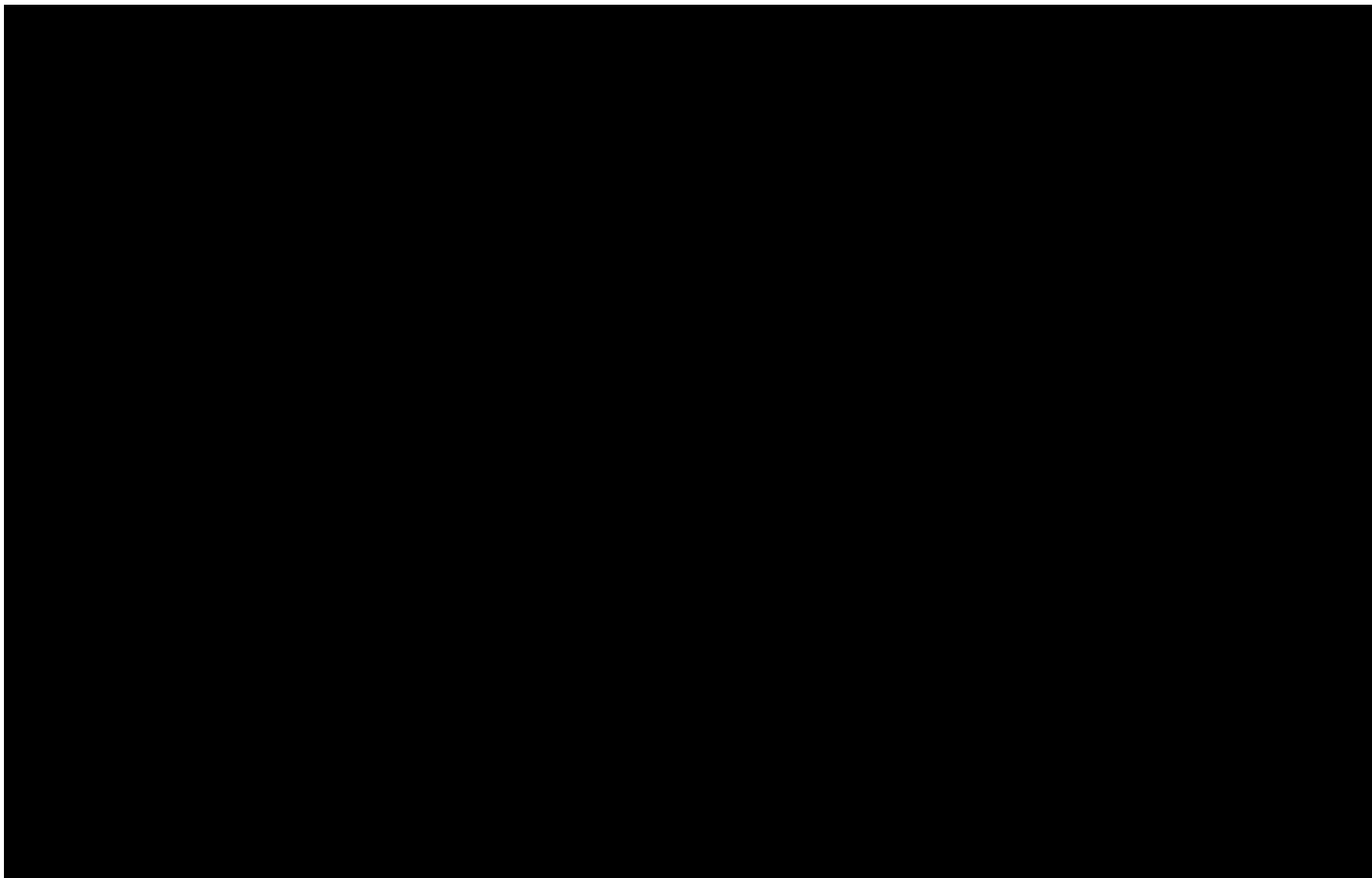
Figure 1-40 – Thickness Map of the Upper Confining Zone
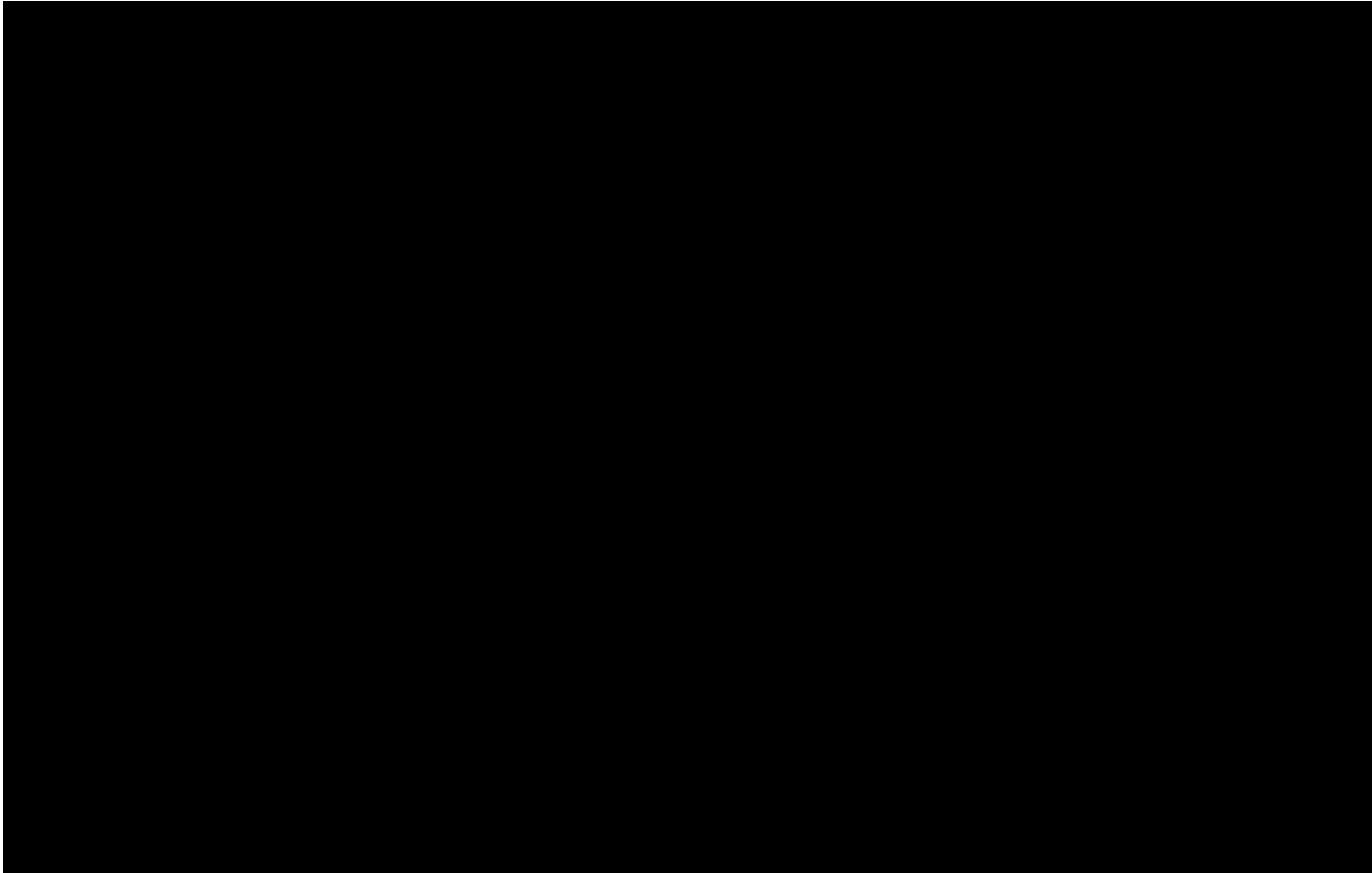
Figure 1-41 – Structure Map of the ███████
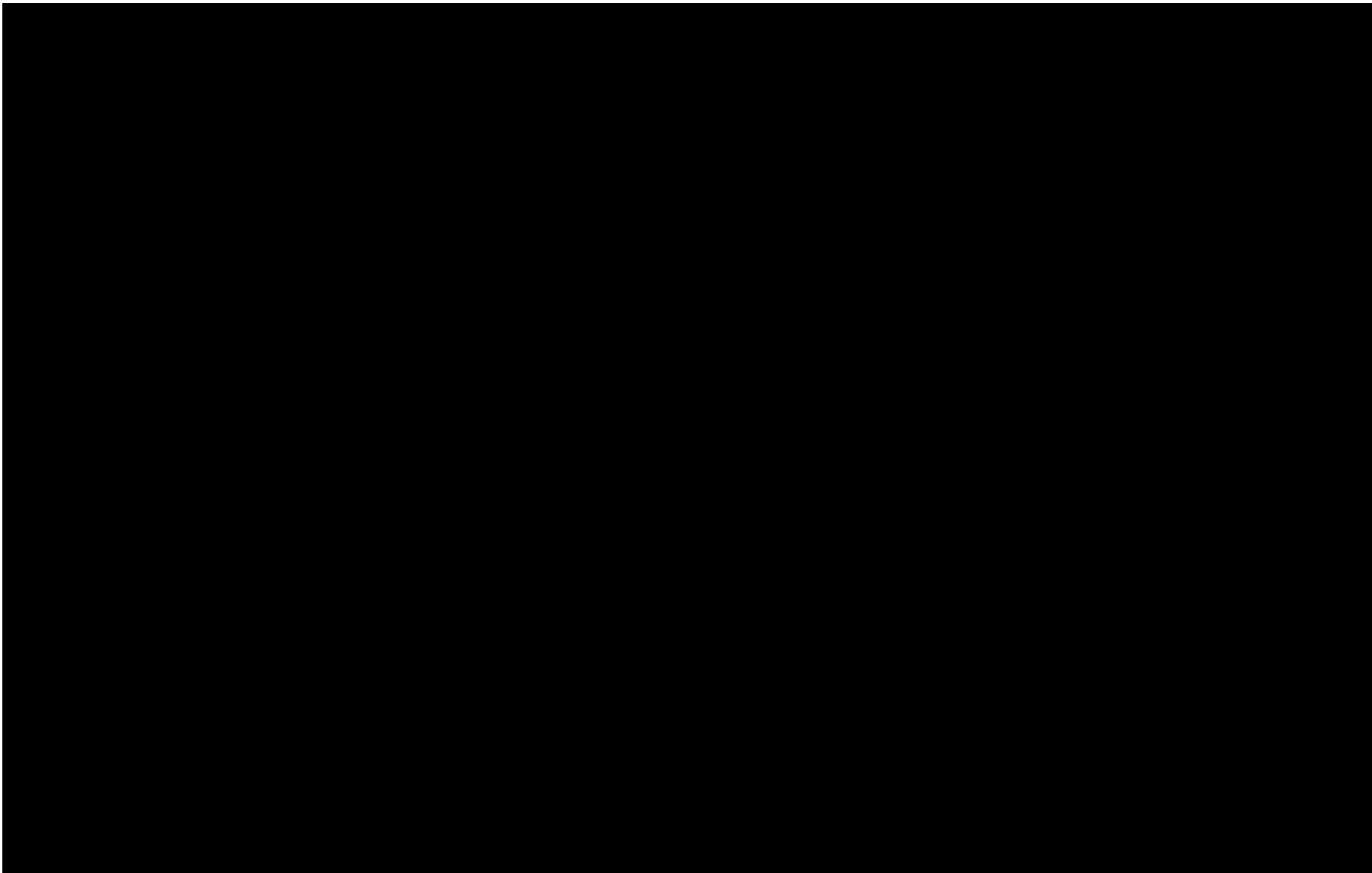
Figure 1-42 – Thickness Map of the ████████
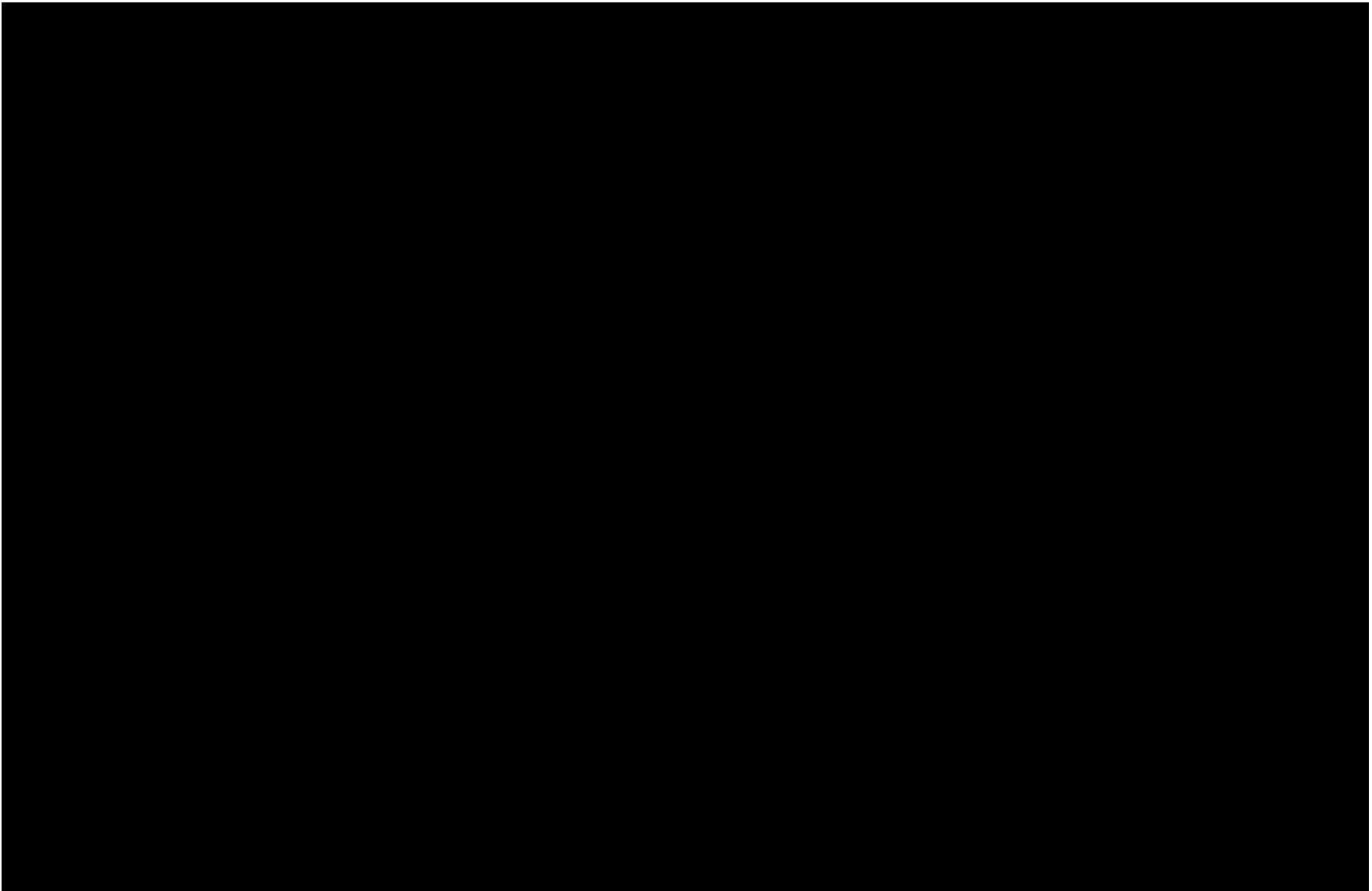
Figure 1-43 – Isopach Map of Combined █████████████████████████

<u>Lithology</u>

The primary upper confining zone in the Orchard Project area can prevent the migration of injected CO_2 from the injection zone to shallower geologic intervals and USDWs. The sealing integrity is high due to the dominant lithological characteristics based on core, well log, and subsurface analog data.

███████████████████████████████ combine predominantly ████████████████████

███████ . This interval is laterally homogenous and vertically heterogeneous over the region, indicating effective confinement wider than the scope of the project area.

██

███ The core in the lower part of the confining zone helps to demonstrate the transition of lithofacies from an injection zone to the beginnings of a confining zone. Figure 1-45 shows a map of the location of the cross section in Figure 1-44.
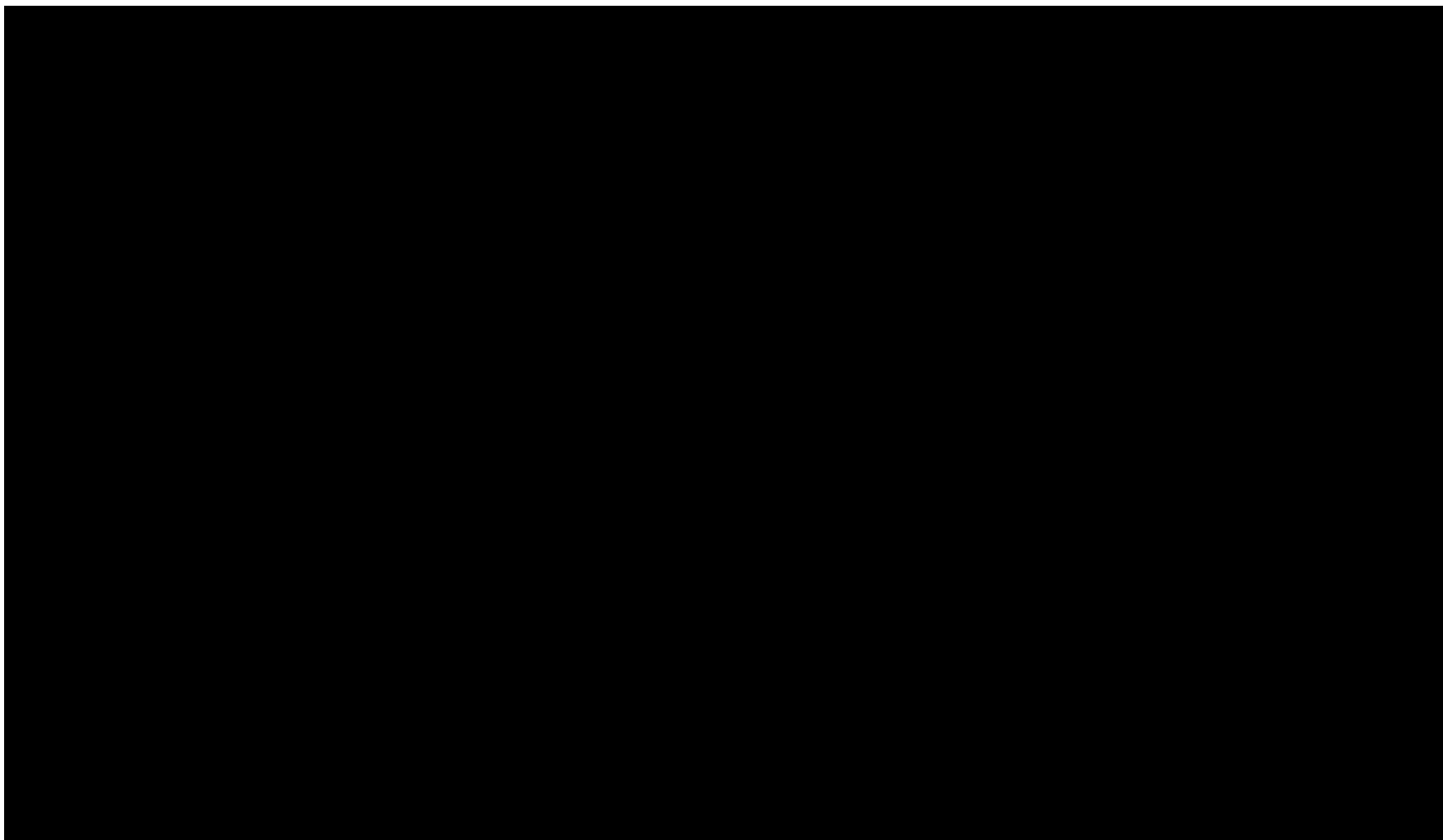
Figure 1-44 – A cross section of wells
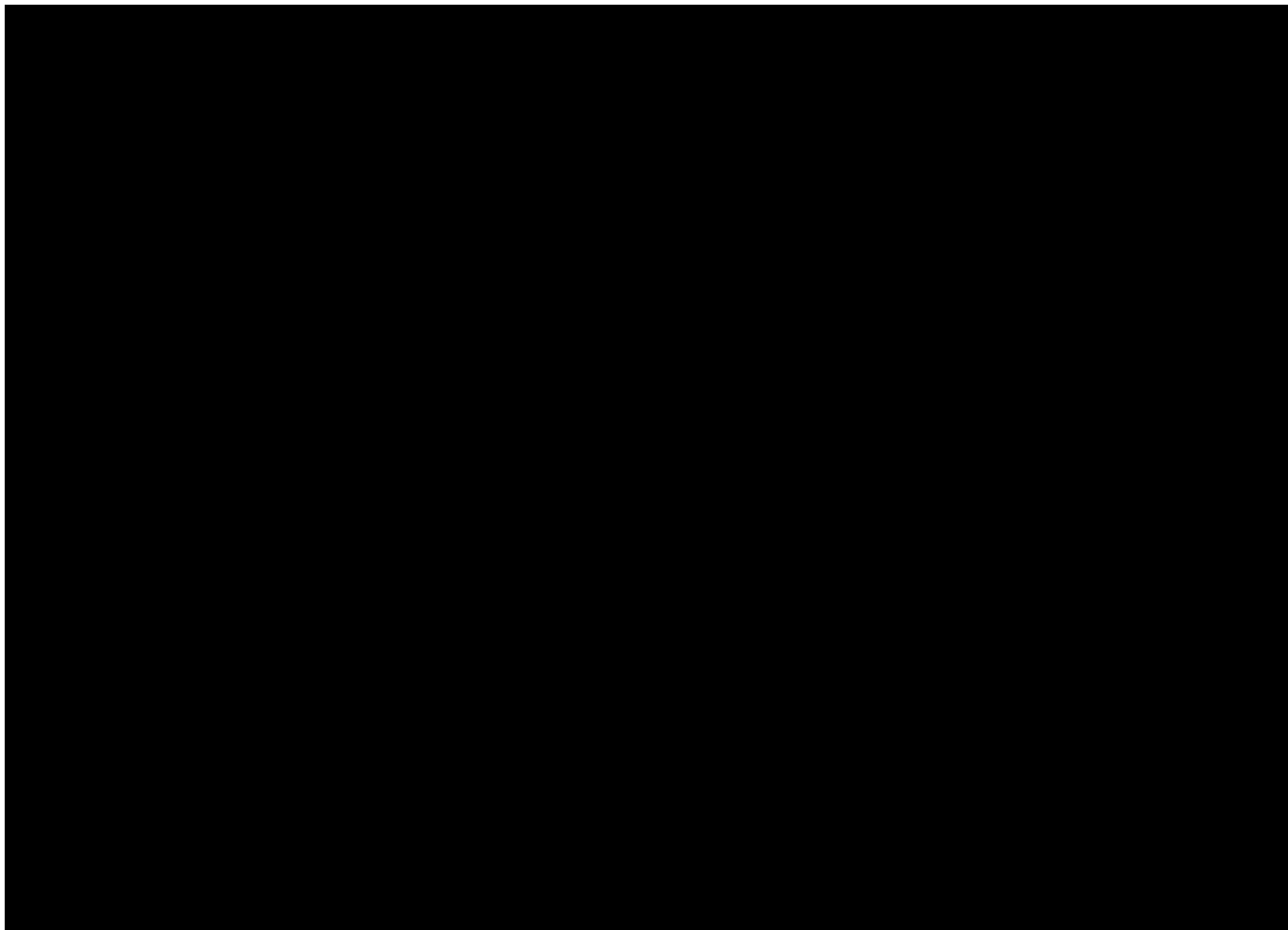
Figure 1-45 – Map showing the location of the cross section shown in Figure 1-44 (black dashed line) and the N-S 2D Seismic Line (A-A' in red color) shown on Figures 1-64, 1-65 and 1-66.

The site-specific slabbed core from ███████████████ was photographed, and six core plugs were acquired every 20 ft for Core Lab Houston to further analyze. No petrophysical analysis was performed. Although the neutron log was relatively old, it showed a transition between two wells to the north and south of the cored well. Higher neutron-count readings indicate lower porosity.

The location of the core on the southeastern side of the Orchard Project area ████████████
███
███
███

████████████████████████████████████ the Orchard Project ████████████████████████
███
████████████████████████████████ In the project area, however, the well logs exhibit more of a laterally consistent low-porosity lithofacies in the basal part of the confining zone and are likely representative of lower-energy settings, reflected in Figures 1-20 and 1-21 (in *Section 1.3.2*).

The six thin sections from the core were described, and the slabbed core was observed and photographed (shown in Figures 1-46 through 1-57). These vertical core plug samples demonstrate how the basal part of the confining zone to the █████ the Orchard Project area is highly heterogeneous and dominantly low porosity.

Figure 1-46 shows a thin section from ████████████████████████████████████
███
███
███
██
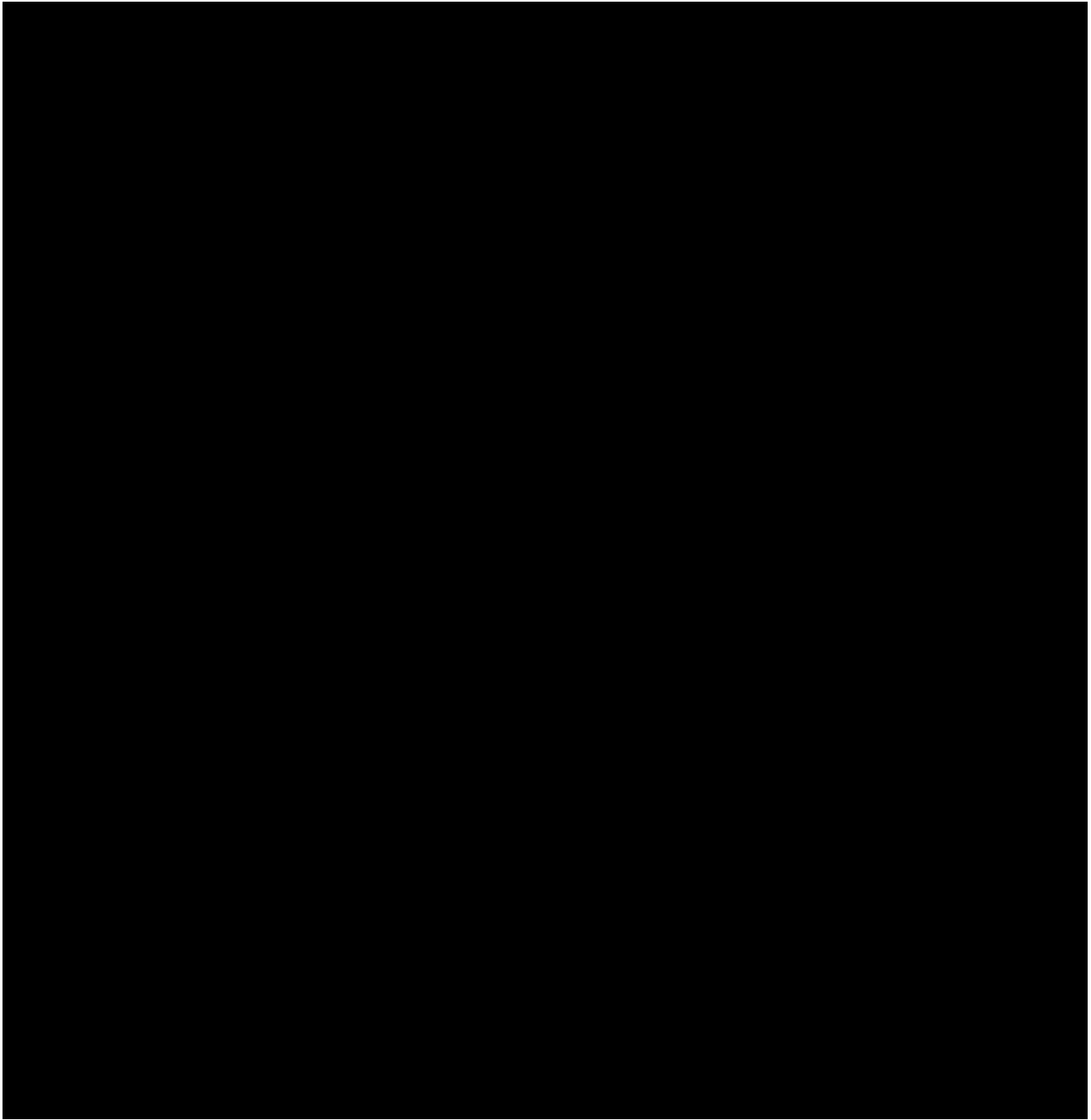
Figure 1-46 – Thin section from well ████████████████████████████████████
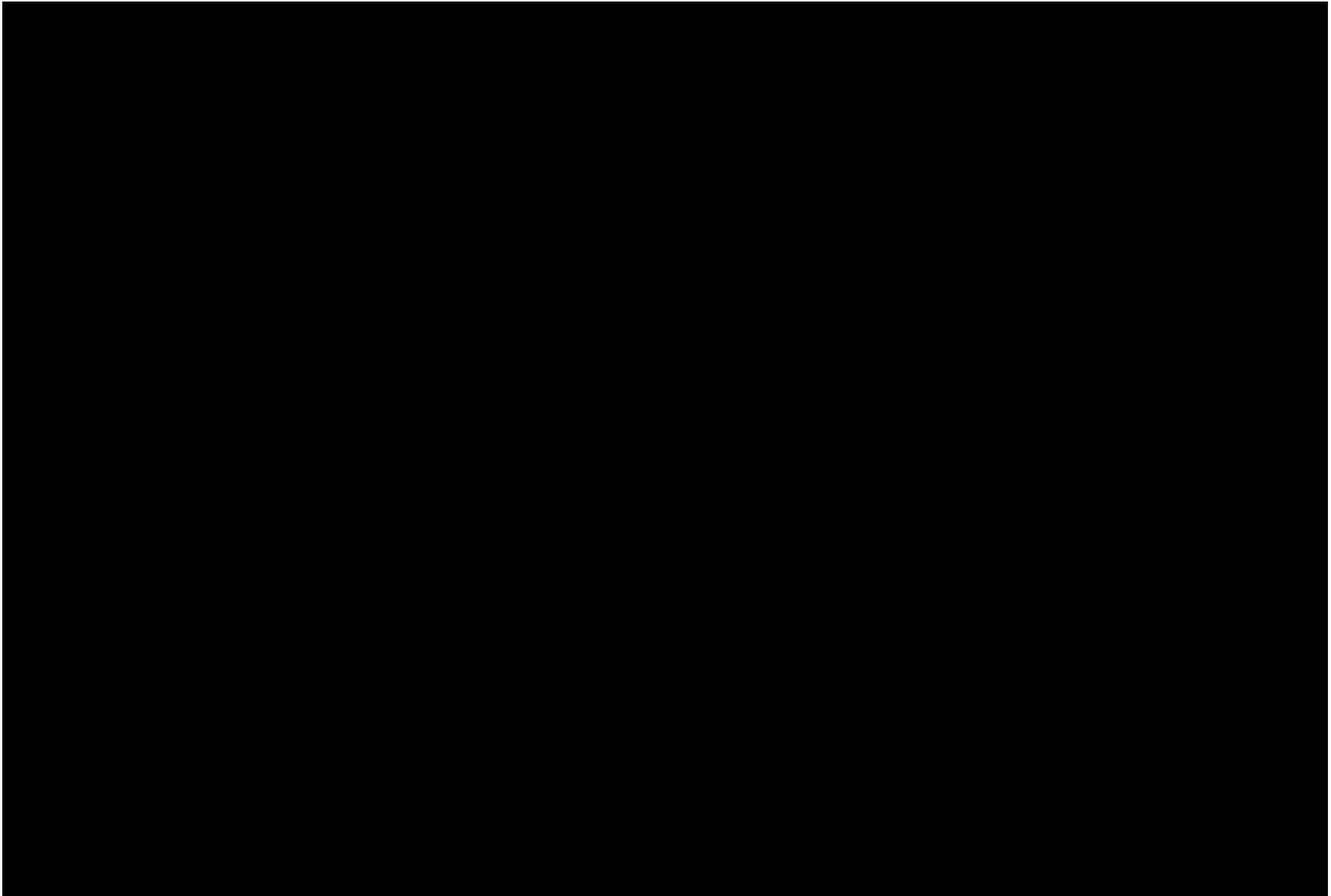
Figure 1-47 – Photograph of slabbed core for well ███████████████, where the thin section in Figure 1-47 was acquired.

Figure 1-48 shows a thin section from well
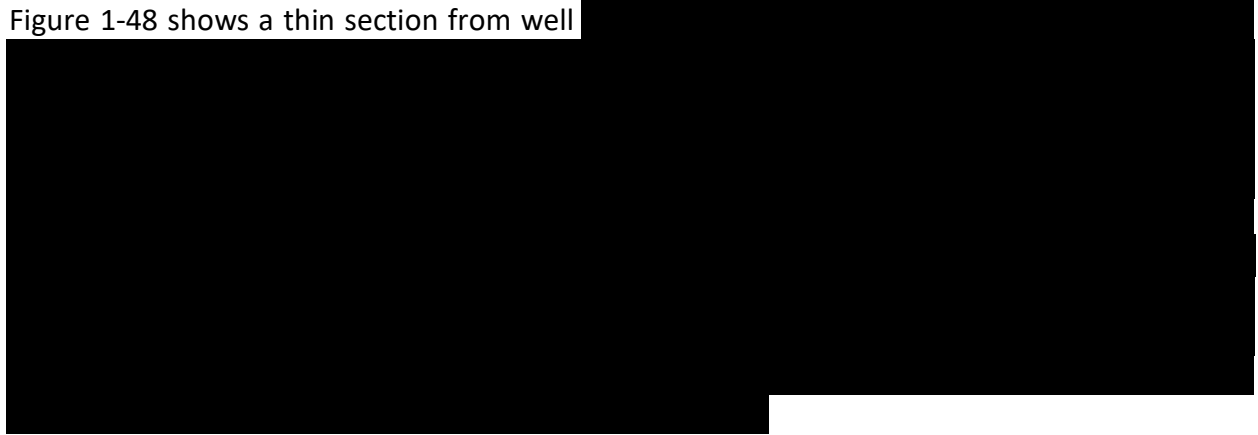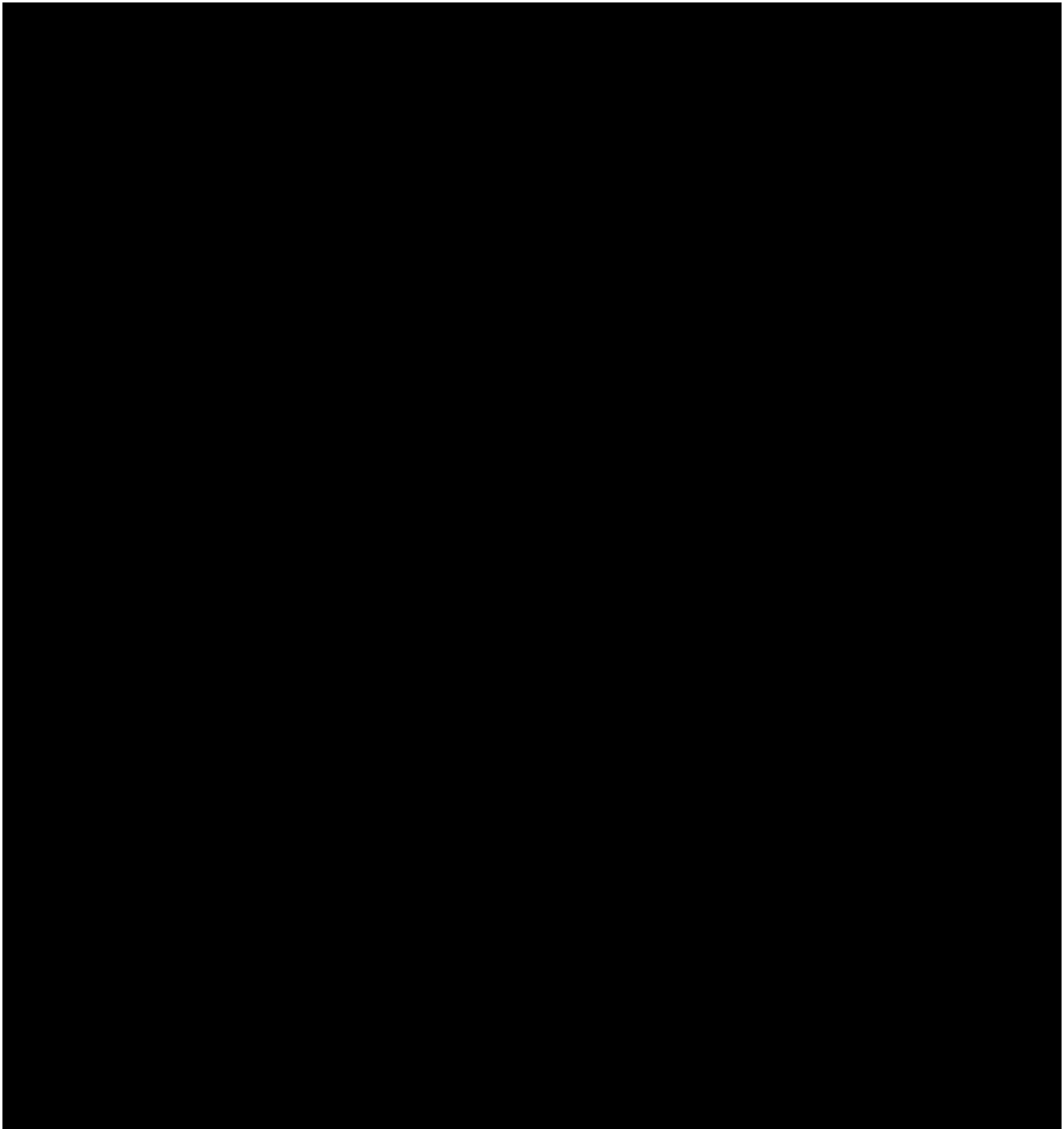
Figure 1-48 – Thin section from well ▮▮▮▮▮▮▮▮▮▮▮▮▮▮▮▮▮▮▮▮▮▮▮▮▮▮▮▮▮▮▮▮▮▮▮▮
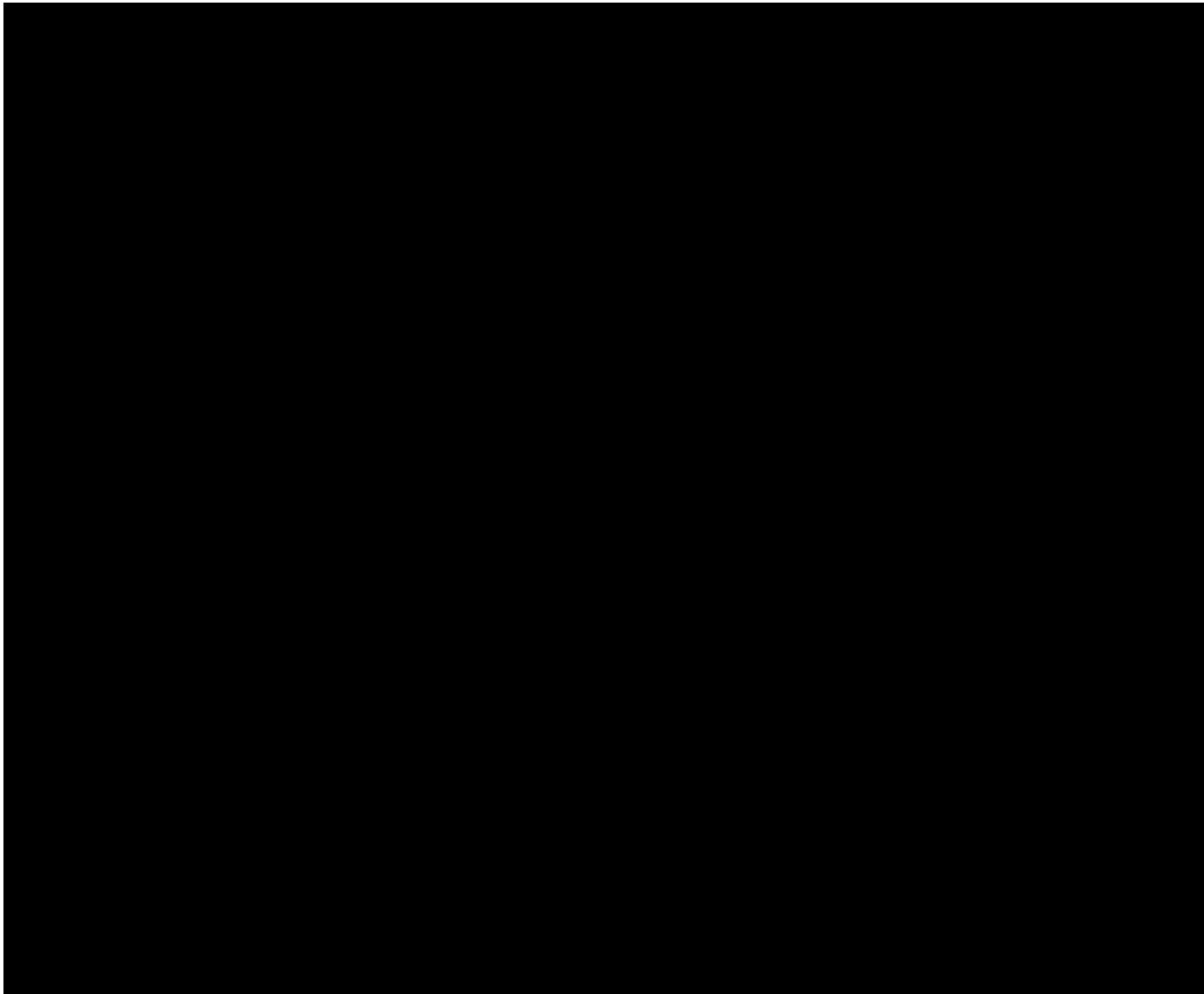
Figure 1-49 – Photograph of slabbed core for well ▮▮▮▮▮▮▮▮▮▮▮ , where the thin section in Figure 1-48 was acquired.

Figure 1-50 shows a thin section from well
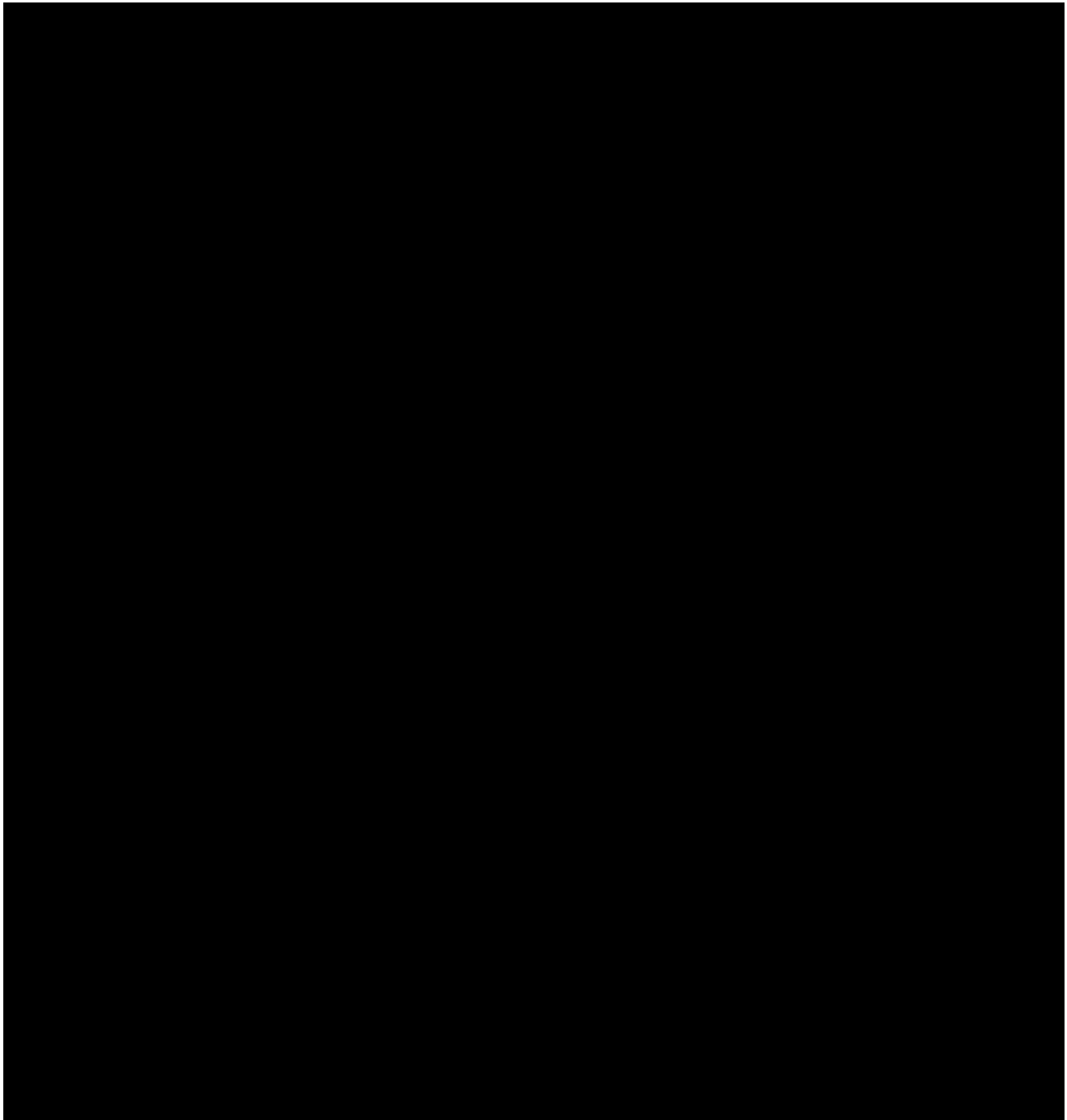
Figure 1-50 – Thin section from well ███████████████████████████████████████ .
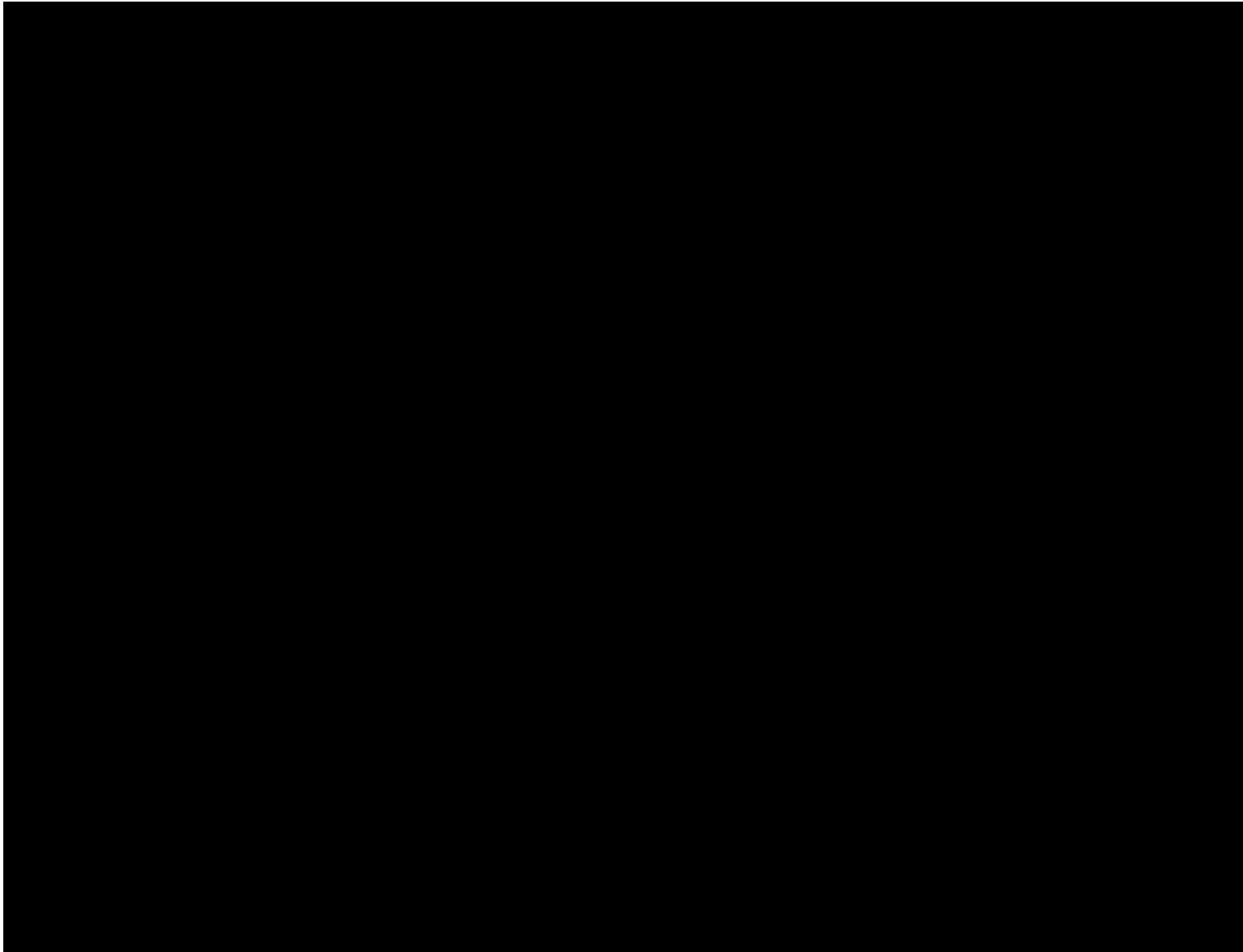
Figure 1-51 – Photograph of slabbed core for well ███████████████, where the thin section in Figure 1-50 was acquired.

Figure 1-52 shows a thin section from well
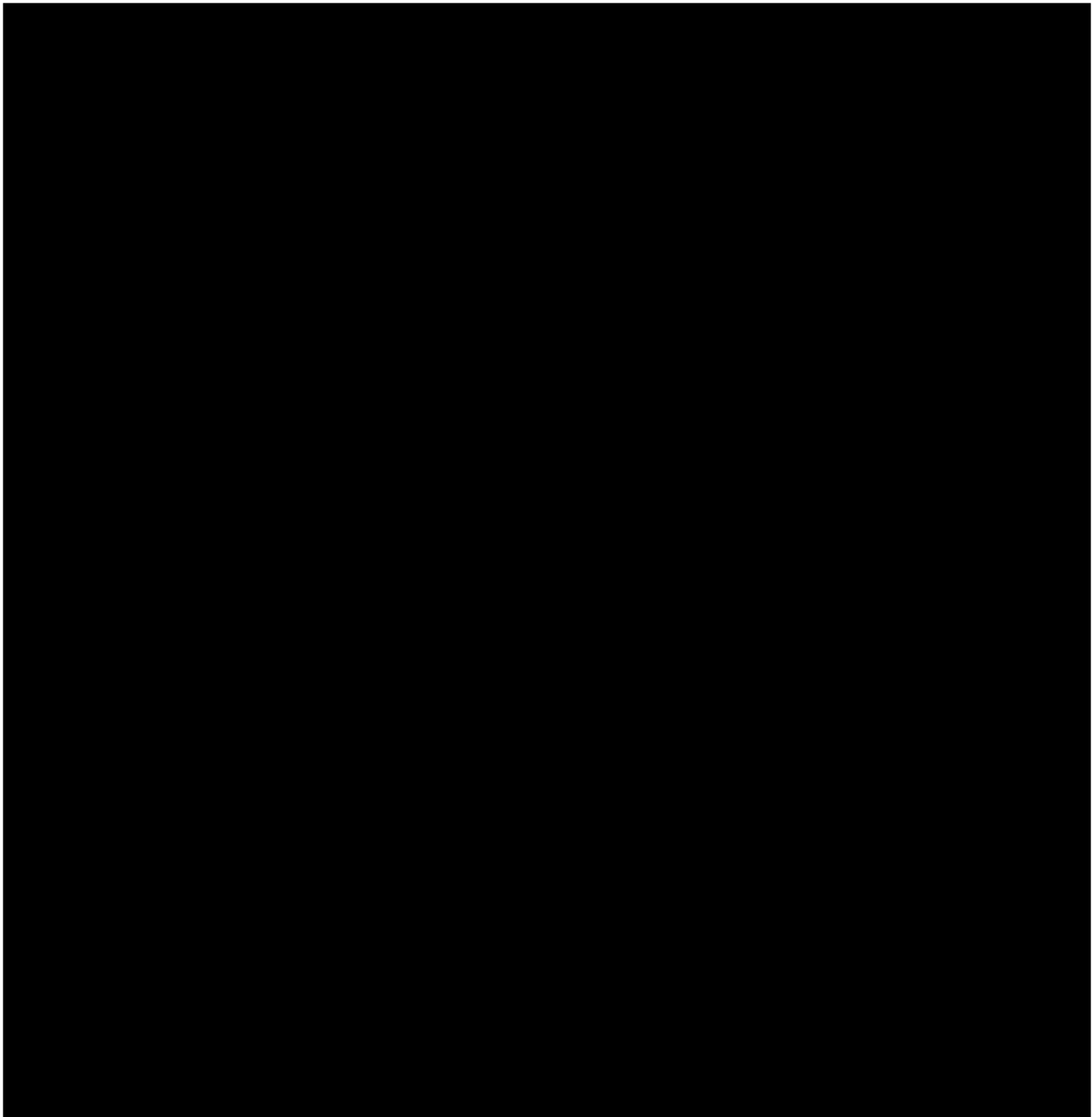
Figure 1-52 – Thin section from well ███.
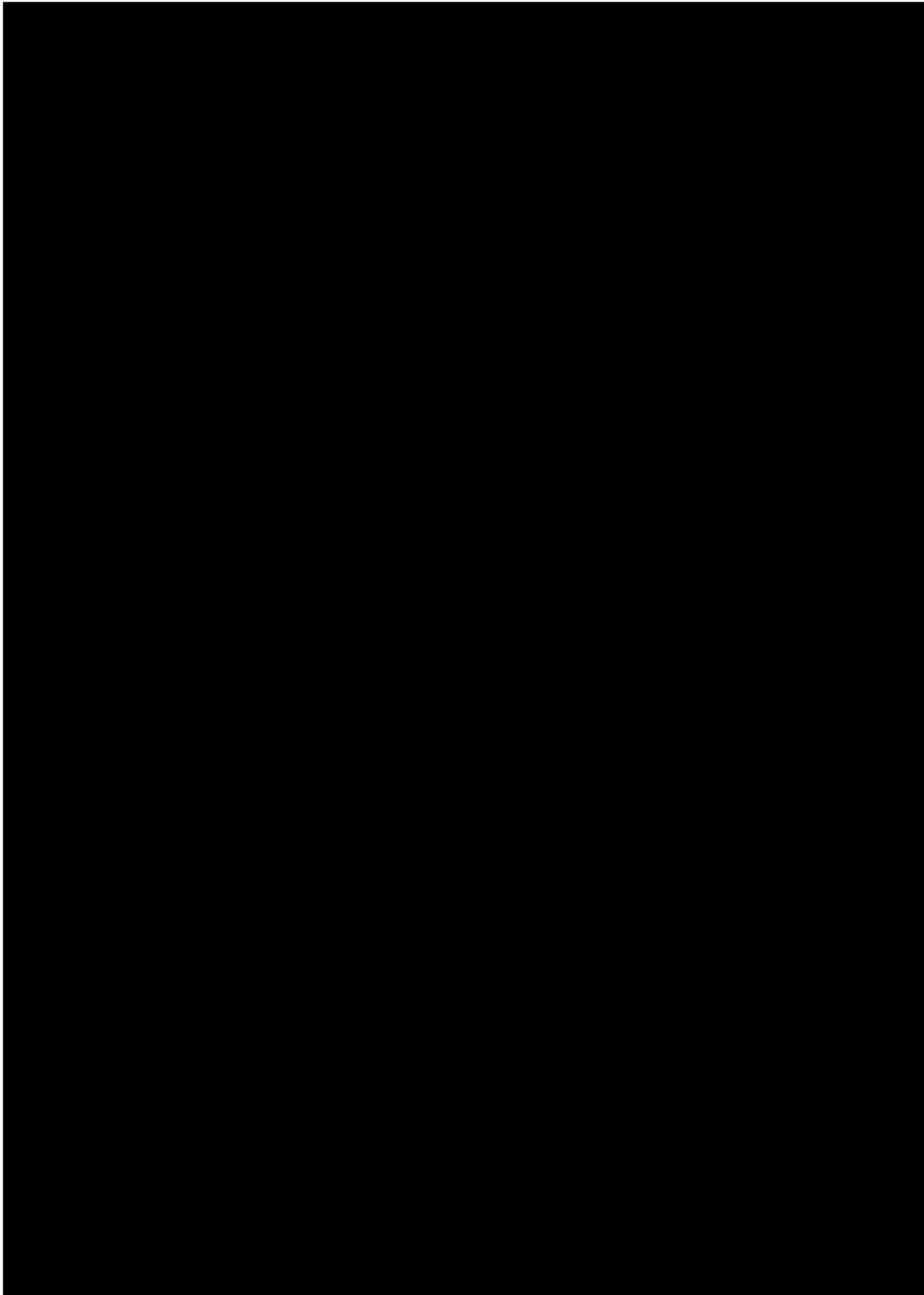
Figure 1-53 – Photograph of slabbed core for well ▮▮▮▮▮▮▮▮▮▮▮▮▮▮, where the thin section in Figure 1-52 was acquired.

Figure 1-54 shows a thin section from well
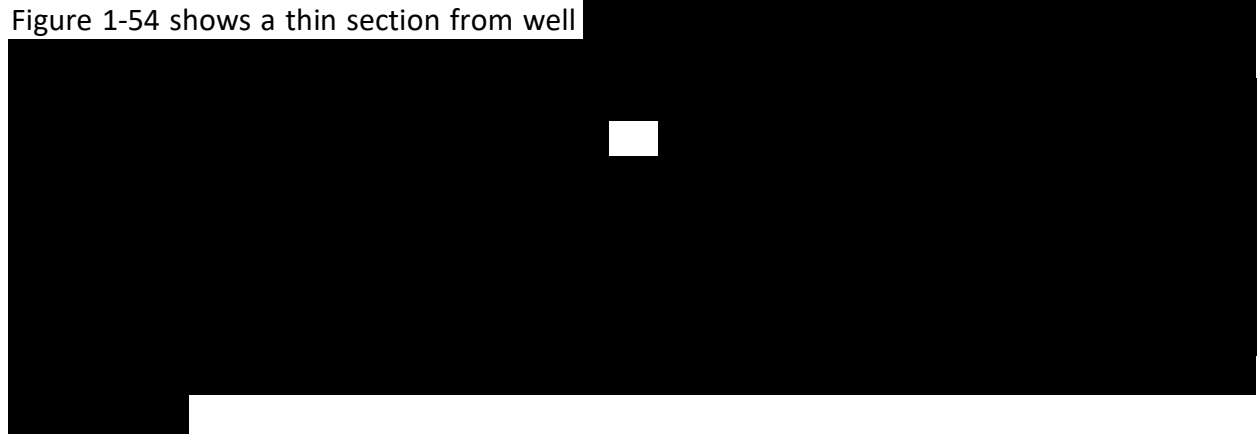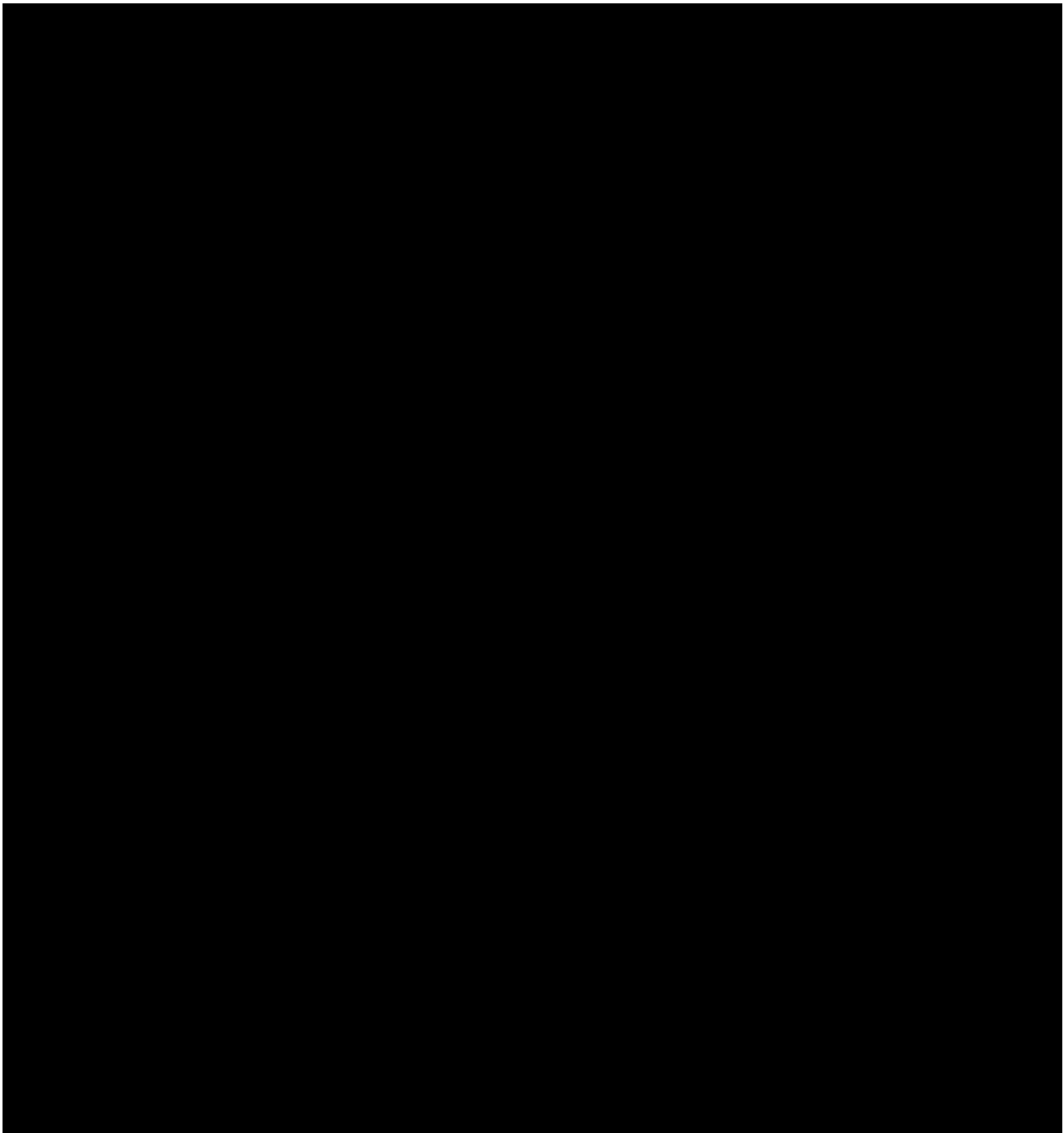
Figure 1-54 – Thin section from well
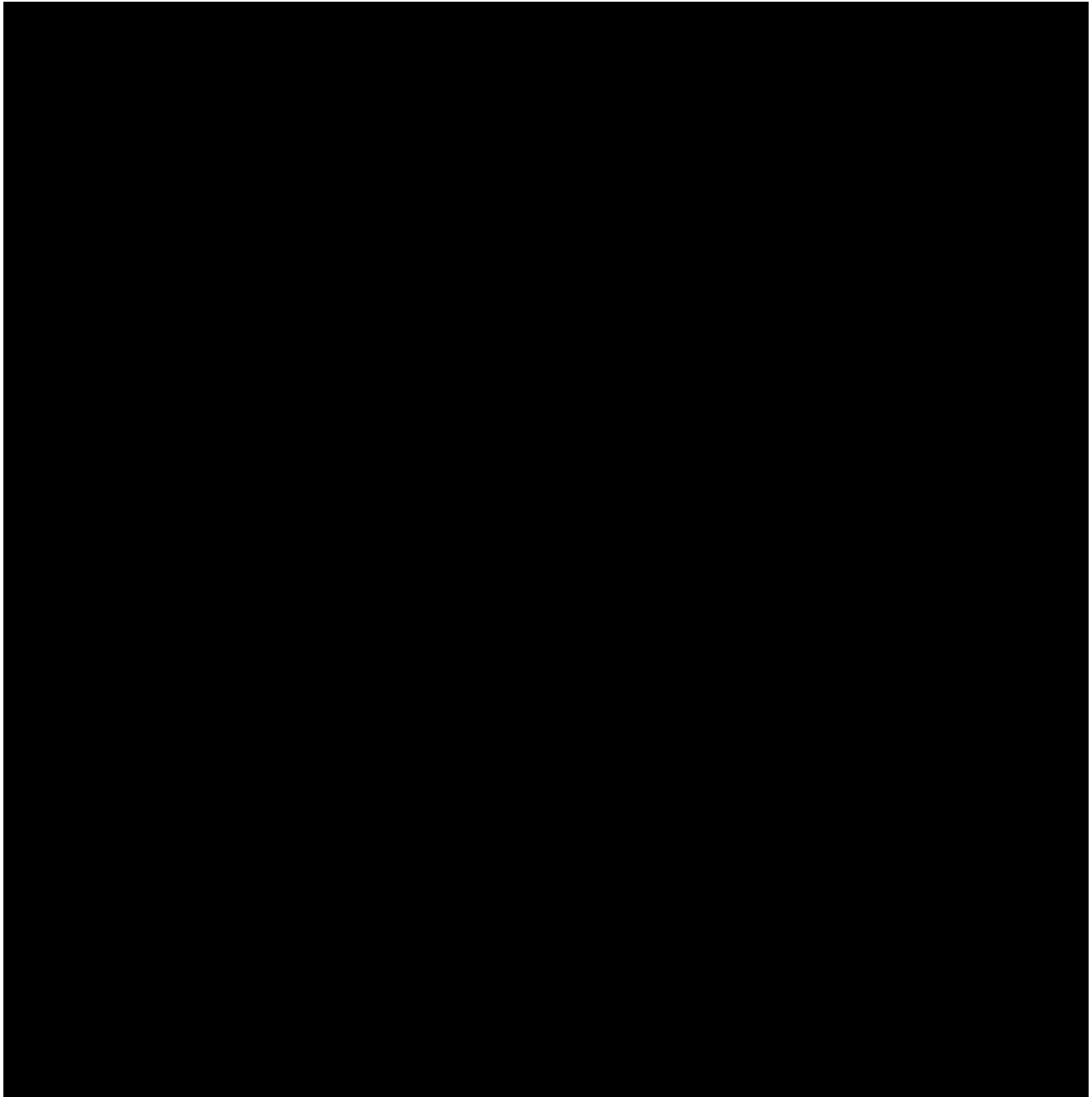
Figure 1-55 – Photograph of slabbed core for well ███████████████, where the thin section in Figure 1-54 was acquired.

Figure 1-56 shows a thin section from well
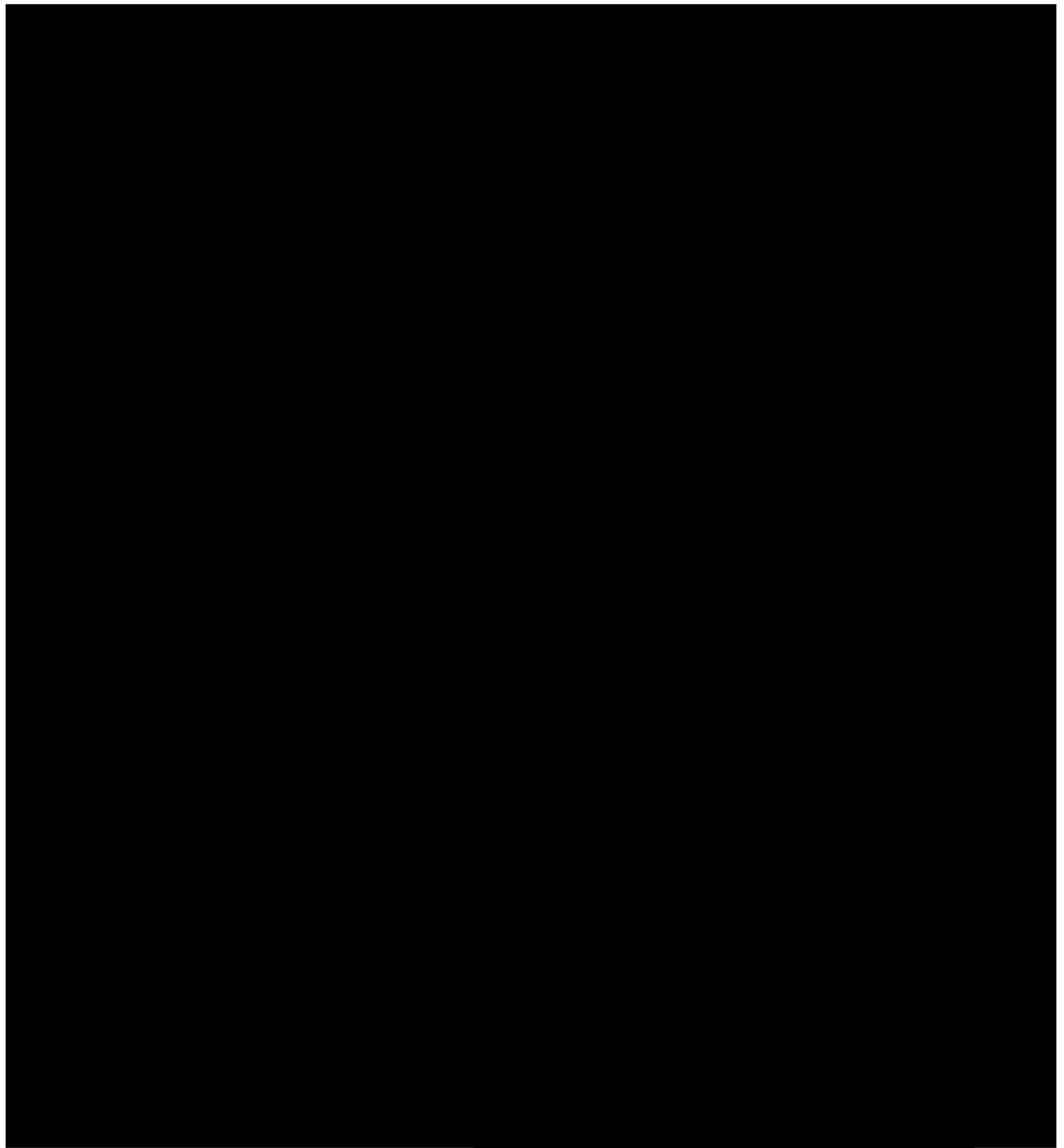
Figure 1-56 – Thin section from well ██.
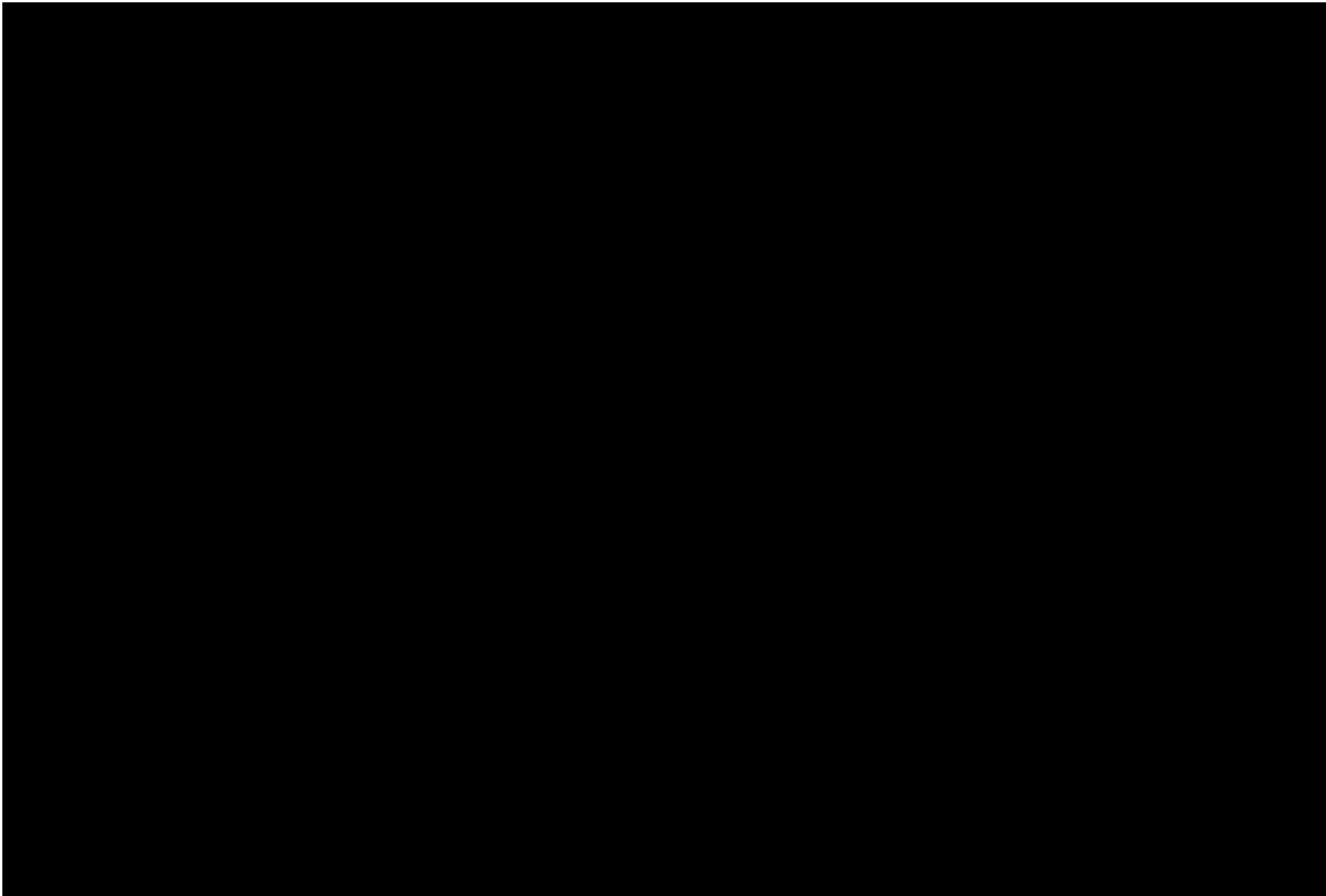
Figure 1-57 – Photograph of slabbed core for well ▓▓▓▓▓▓▓▓▓▓▓▓▓, where the thin section in Figure 1-56 was acquired.

The shallowest plug acquired from this core (as was shown in Figure 1-49) is helpful as representing the dominant lithofacies to expect within the Orchard area (from the base to the top of this confining zone). Thin sections showing ████████████████████████████ ██, as discussed above.

Furthermore, field-specific and regional-scale publications have featured this confining zone as a relatively thick interval with high sealing integrity, to prevent injected CO_2 (or in situ hydrocarbons) from migrating vertically into shallower formations.

<u>Porosity</u>
Density porosity was derived using the bulk density log and an estimated matrix density for the upper confining zone. The matrix density assumed a dominant mineralogy of ██████ ██ ██

██ ██ ██ ██

The average porosity derived from well logs using this approach is approximately ██ in the confining zone. The lowest porosity is in the upper half of the confining zone. No average map of porosity in this confining zone was created; however, low porosity was observed in wells surrounding the proposed Orchard No. 1–No. 7 locations ████████████████████████████ ██. Furthermore, the nearest well ████████ ██████████ provides a qualitative data point. Although no petrophysical analysis was completed due to a lack of neutron-density logs, the high resistivity values (and lack of separation between deep and shallow curves) look similar to adjacent wells and indicate low porosity rock.

Porosity was not visible within the slabbed core sample of well ██████████████████. No secondary porosity features that would breach the containment of CO_2 in the injection zone, such as major dissolution porosity or fractures (indicating shear fractures or fracture networks in the vicinity), were observed in the core.

<u>Permeability (Horizontal and Vertical)</u>
The average calculated matrix permeability for the confining zone is null, based on the average calculated porosity. ██ ██. The confining interval core analysis indicates a very low permeability, typical of suitable confining intervals. This confining zone permeability will be revisited once wells are drilled and new core is obtained in the confining interval.

A closer examination of the confining zone shows vertical heterogeneity causing well log porosity to vary significantly. Further work to characterize these beds via conceptual and numerical modeling is discussed in *Section 1.10*.

Figure 1-58 shows the
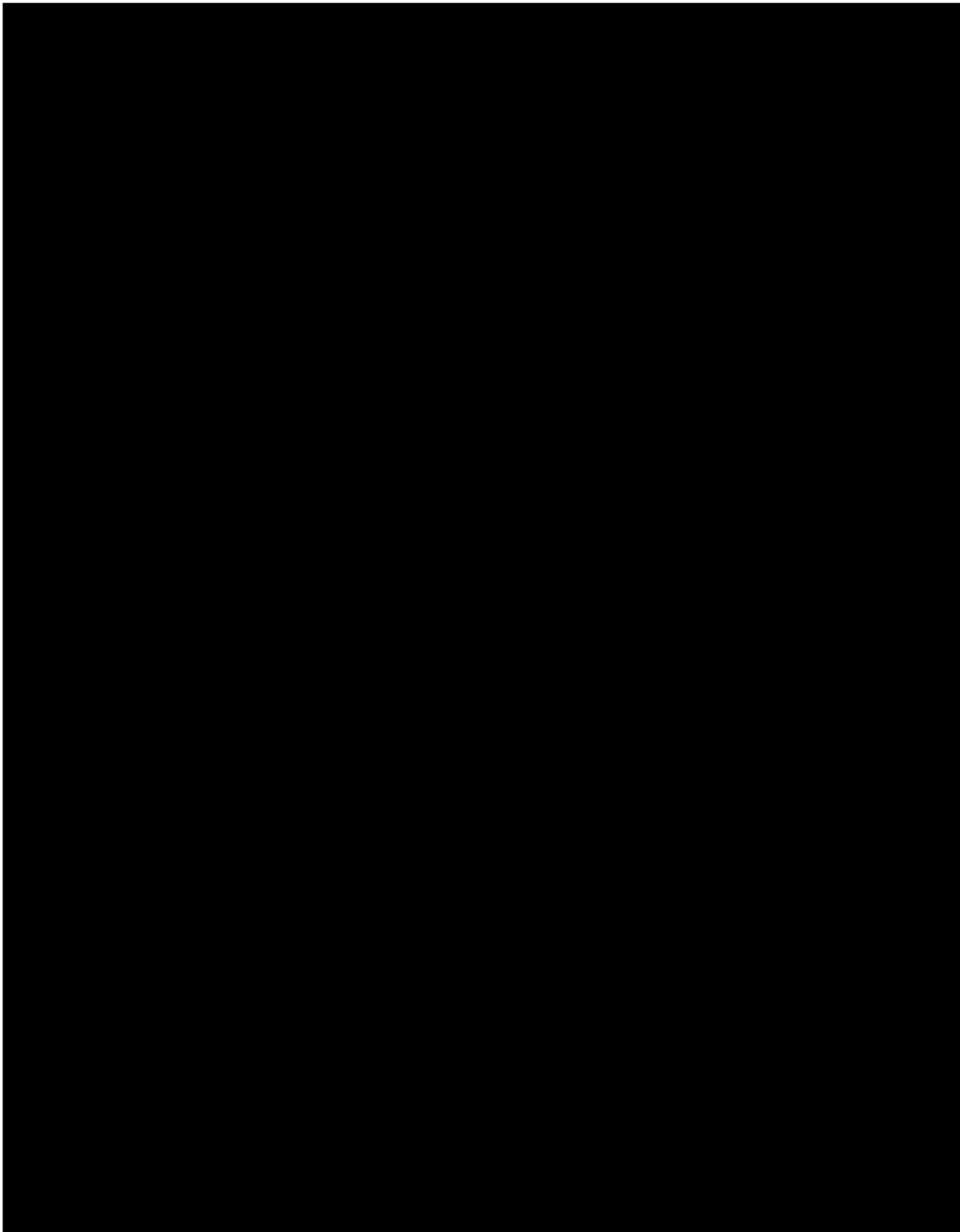
Figure 1-58 – Mercury saturation versus injection pressure results from high-pressure mercury injection testing (Core Lab Houston) for well ███████████████████████
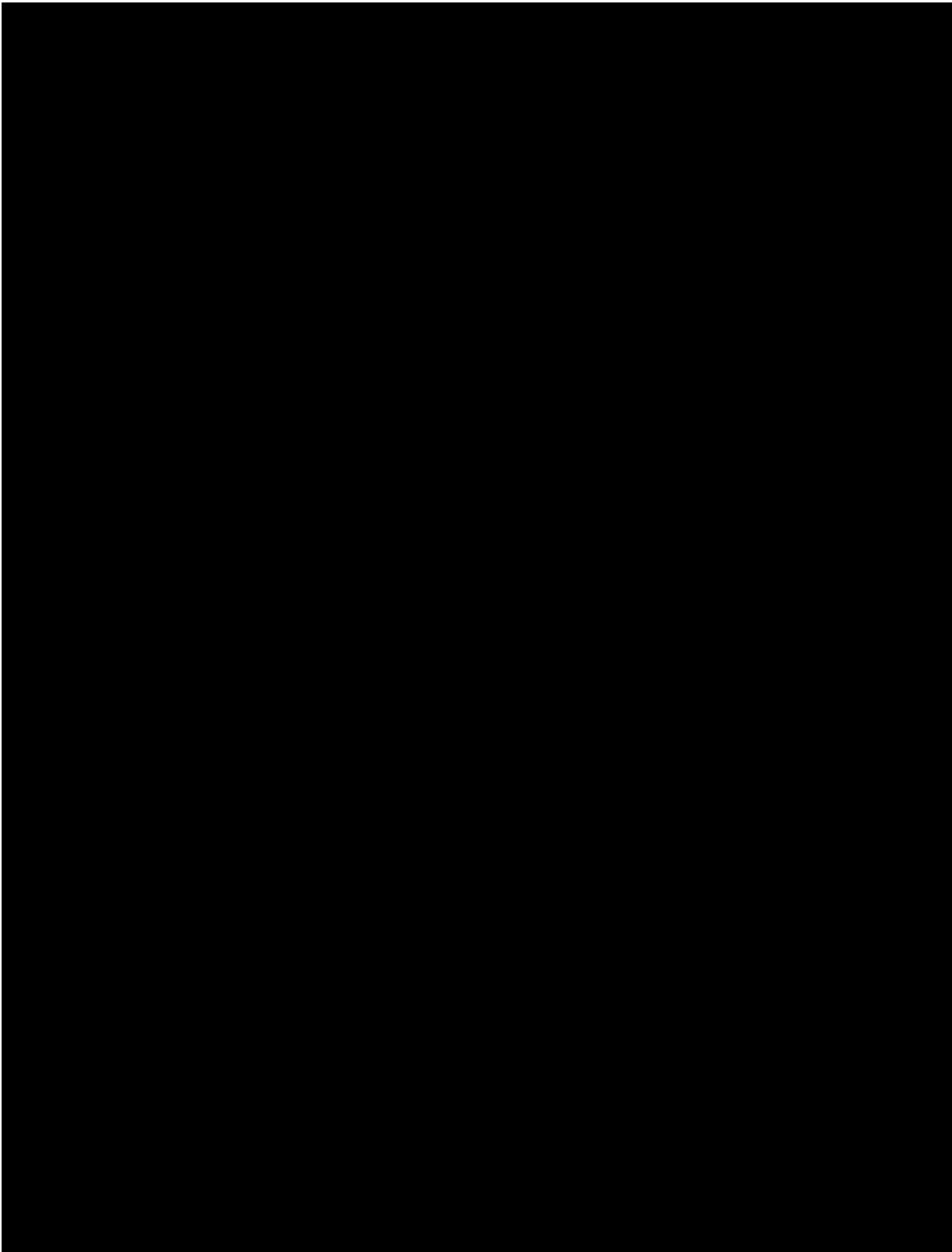
Figure 1-59 – Pore-throat size and distribution results from high-pressure mercury injection testing (Core Lab Houston) for well ███████████████████████████.

<u>Water Saturation</u>
The confining zone is assigned 100% water saturation with the same salinity as the injection zone.

1.3.4   Primary Lower Confining Zone
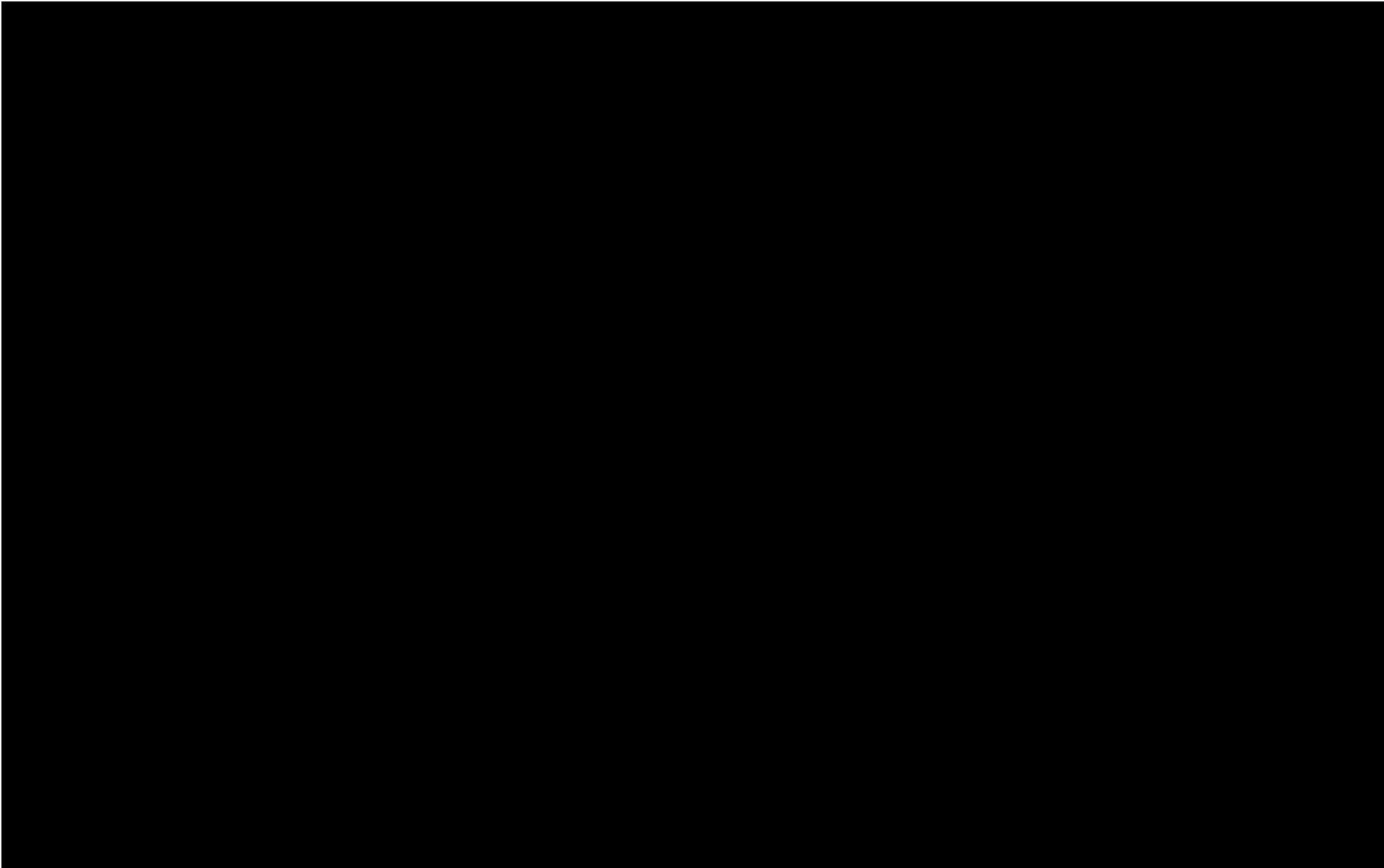
Figure 1-60 – Depth structure map (TVD SS) of the base of the ███████████████████████ (lower confining zone).
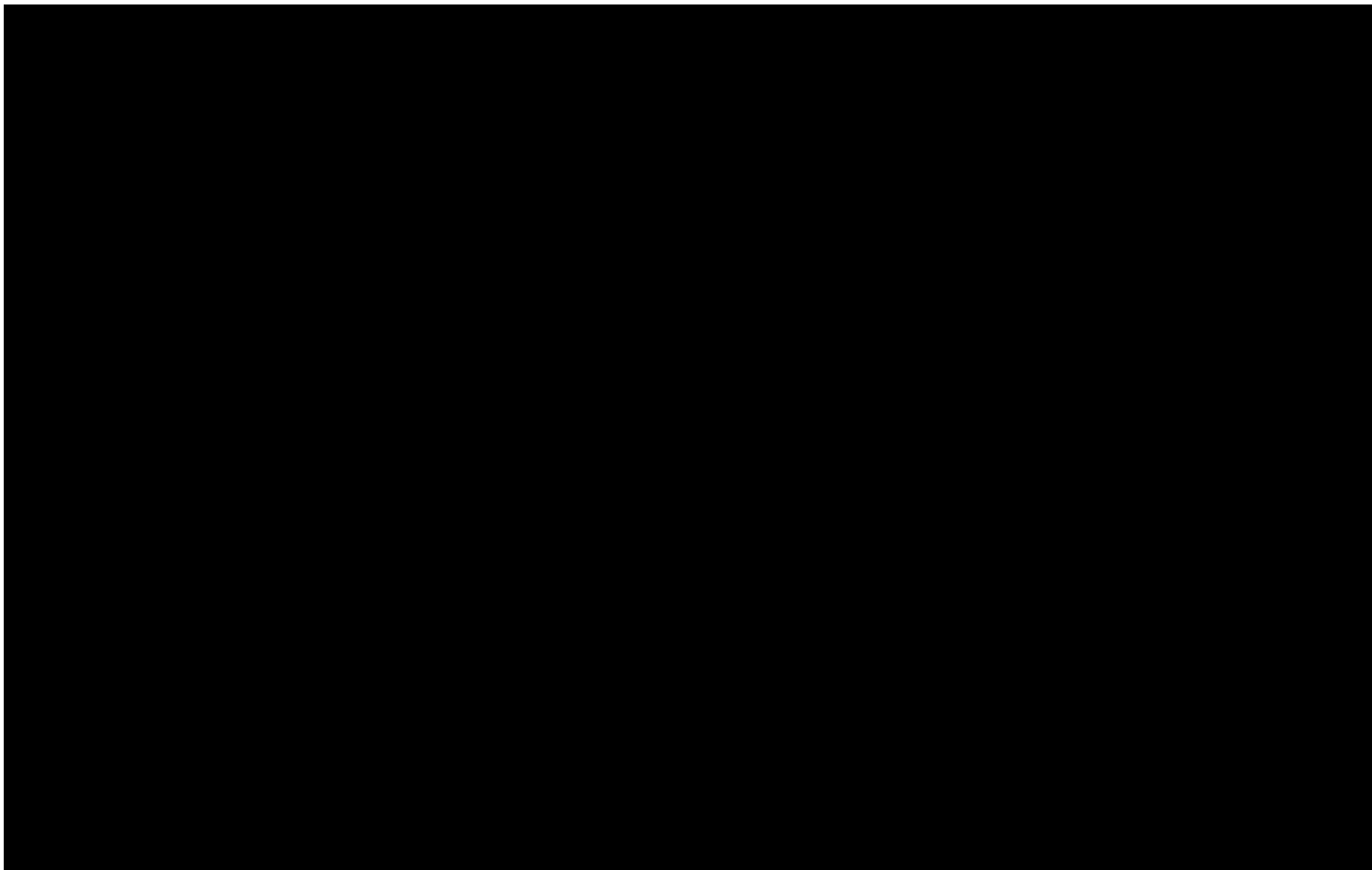
Figure 1-61 – Thickness map of the ▮▮▮▮▮▮▮▮▮▮▮▮▮▮▮▮▮▮▮ (lower confining zone).

Lithology
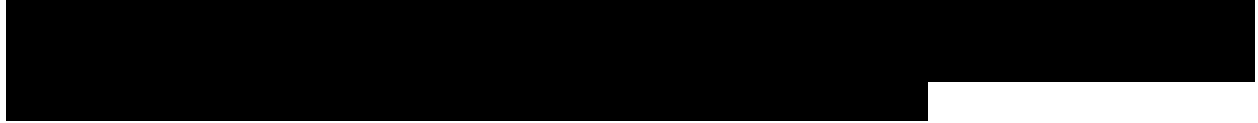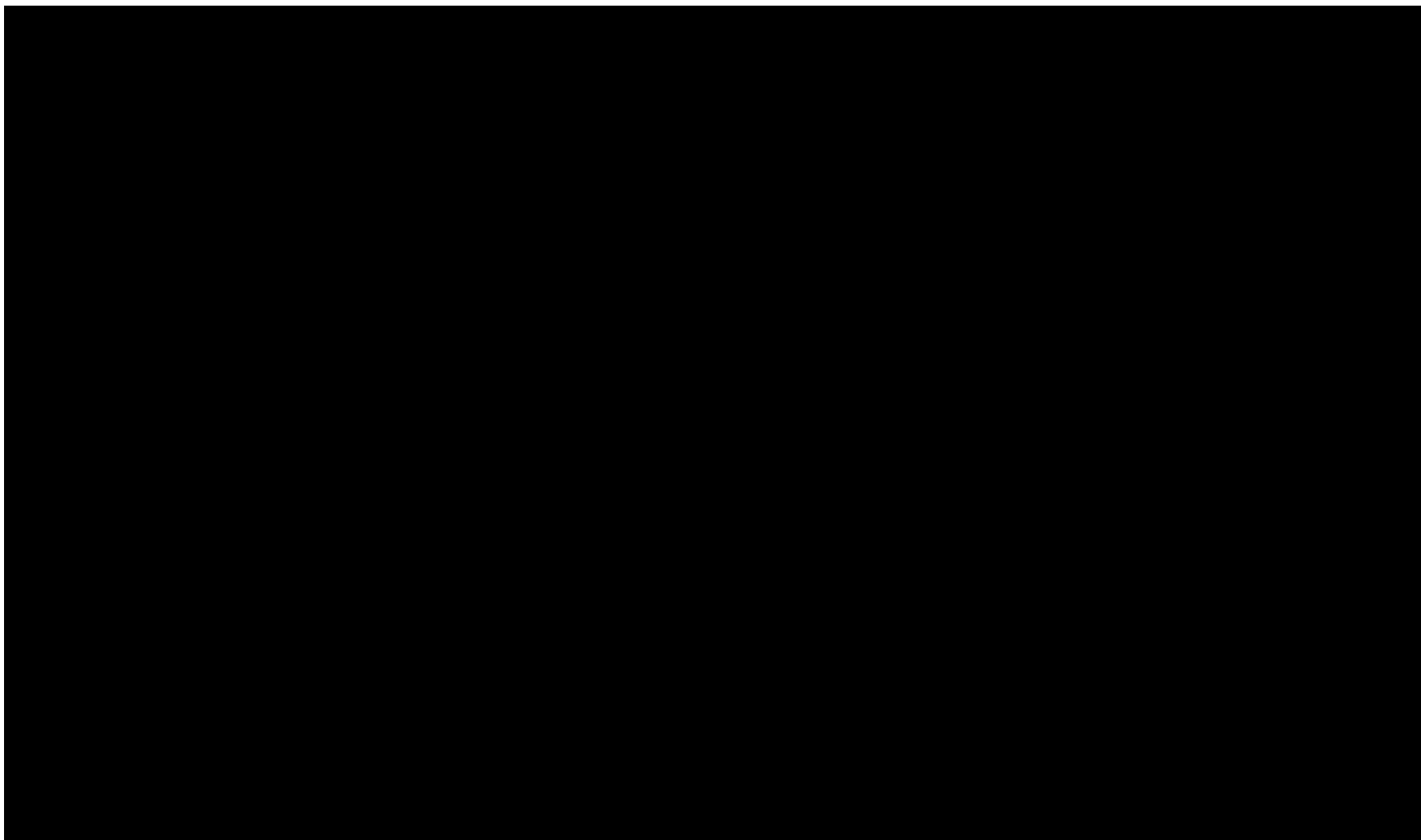
Figure 1-62 – Simplified depiction of a cross section oriented north-south to the east of the Orchard Project vicinity. It shows the dominant lithology changes across ██ .
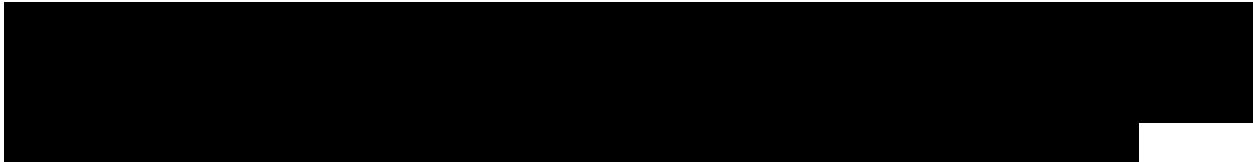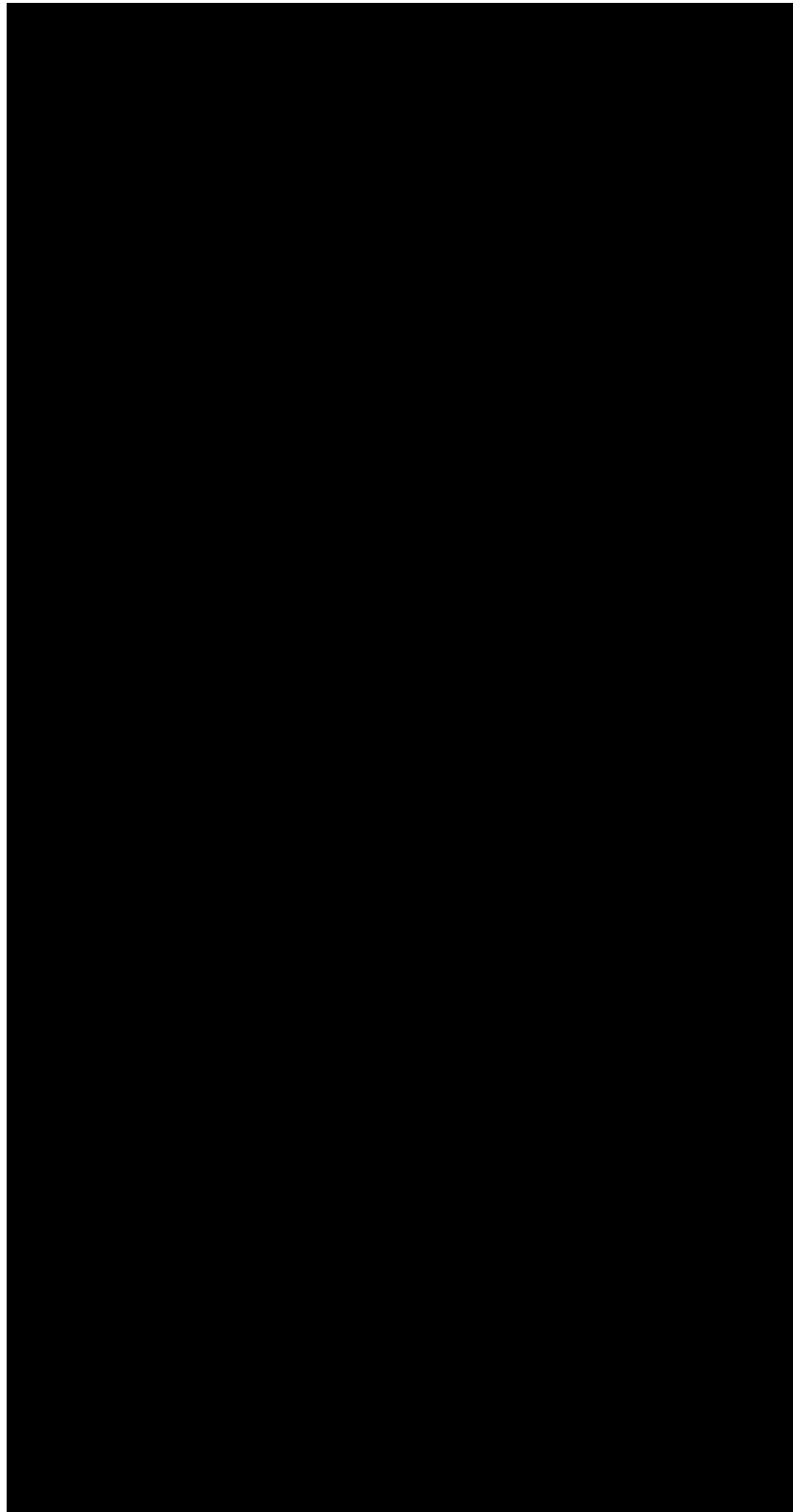
Figure 1-63 – A snapshot of the mud-log sample lithologic interpretation (track 2) for the

Porosity

Density porosity was derived using the bulk density log and an estimated matrix density for this confining zone. The matrix density assumed the dominant mineralogy of ███████████████████████ ██

Minimal correction was needed for shale (i.e., clay and silt) effects. This was based on the very low potassium-thorium gamma ray log values. ████████████████████████████████ ██

The average porosity derived from well logs using this approach is approximately ███ in the confining zone. The porosity is consistent vertically, based on █████████████. However, the closest well ████████████████ shows separation between resistivity log curves (deep and shallower) in the upper portion, indicating some beds possible with high porosity or an incorrect well top pick (i.e., could be deepened by approximately 90 ft). Furthermore, increased porosity and vertical heterogeneity are evident in wells located in multiple directions outside the Orchard Project area.

Permeability (Horizontal and Vertical)

The average calculated matrix permeability for the confining zone is null, based on the average calculated porosity. ██ ██

Water Saturation

The confining zone is assigned 100% water saturation with the same salinity as the injection zone.

1.4.   Site Structure, Stratigraphy, and Deposition: 2D Seismic Integration

Two-dimensional seismic data was integrated with well log data to create the 3D geologic framework within the Orchard Project area. Seismic data was also used to tie in to the regional geologic structural and stratigraphic models. The data also offered additional quality control of the stratigraphic interpretation.

Figure 1-64 shows a ████████ long 2D seismic line running north-south (A-A') through the Orchard Project area. The location of the 2D seismic line is shown on Figure 1-45. The nearby well ████████ ██████████ located approximately ████████ to the west of the line, was used as a pseudo-well to perform a seismic-to-well tie ("pseudo-well tie"). This pseudo-well related well-log data to seismic data, in two-way travel time, to develop a synthetic seismic model to assist with interpreting seismic horizons. The location of the pseudo-well is approximately common depth point (CDP) ████.
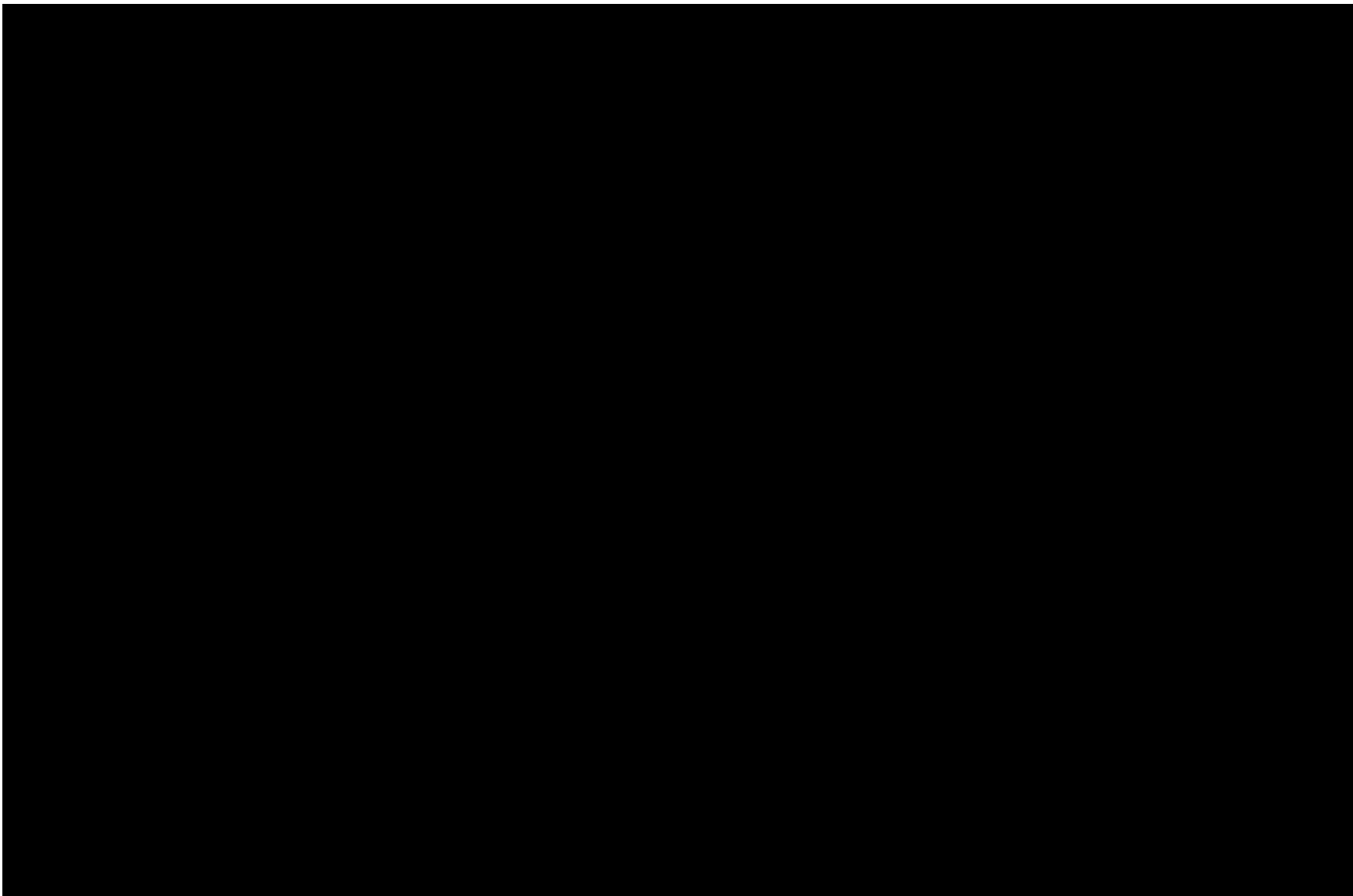
Figure 1-64 – A ▮▮▮▮▮ long 2D seismic line running north (left) to south (right) through the Orchard Project area. The Y-axis is two-way travel time (milliseconds) and the X-axis is CDP traces.

Tying well log data to seismic surveys involved forward modeling of a synthetic seismogram, derived from sonic and density well-log data. The seismogram was used to generate "normal reflectivity," reflection coefficients, and acoustic-impedance log curves. There is an absence of density and acoustic impedance in nearby wells for ███████████████████ ████████████ data. This match resulted in a time-to-depth relationship while considering the following:

- Well-log data quality
- Seismic data quality
- Handling of seismic data at shallow depths
- Handling of seismic wavelet data

The seismic-to-well tie allowed for selection of seismic horizons that either matched well log data and well tops or were not observable on well log data or current well tops—but were visible on the seismic data. ███

The following discussion on structure, stratigraphy, and deposition is related to the 2D seismic evaluation and its integration with well log data and the regional geologic framework.

Figure 1-65 shows the same ███████████ 2D seismic line (A-A') from Figure 1-64—with ██████ ███████████ used to complete a pseudo-well tie—but with interpreted horizons and faults. The bold-line seismic horizons are high confidence and/or correlate to well tops, whereas the dashed-line seismic horizons have lower confidence and/or do not match a well top. The well log from ███████████████████ shows gamma ray (at left) and acoustic impedance (calculated from sonic, at right). The acoustic impedance well log is colored in discrete scale by photoelectric factor log values. All large-scale (i.e., observable on seismic data) fault tips are deeper than the lower confining zone. ██

Figure 1-65 – The same ████ long 2D seismic line from Figure 1-64, but with interpreted horizons and faults shown.

This 2D seismic line trajectory (north to south) is roughly perpendicular to the dominant regional depositional trend ███████████████████████████████ The seismic interpretation objective was to identify low- and high-frequency depositional sequences in the north-south direction through the Orchard Project site and wider area. The aim was to understand and explain these sequences' lateral or vertical changes that may affect ███████████ ██, as described in *Section 1.3*.

1.4.1   Horizon Interpretation

Several seismic horizons were interpreted from the ████████████████████ on the 2D seismic line (A-A'). Most seismic horizons matched the well tops in well ██████████████. The tops of the ███████████████████ were interpreted as high-confidence seismic horizons for the upper confining and injection zones. The top of the injection zone and the top and base of the lower confining zone were interpreted as lower-confidence seismic horizons. Deeper and shallower seismic horizons than the injection and confining zones were mostly interpreted as high-confidence picks.

As was displayed in bold lines in Figure 1-65, the injection and confining zones show continuous seismic horizons. The dashed lines illustrate the effect of high-frequency cycles and lateral variations of lithofacies within the injection and lower confining zones (and below). Several dashed lines likely represent and correlate to higher frequency surfaces (associated with either transgression or highstand or lowstand periods) within the ██████████████████ ████████formations, rather than the current well-top stratigraphic framework. At ██

At CDPs ███ ██ ██ ██ ██████████████████

As mentioned above, the ████████████████████ seismic horizon matching well log data and well top picks. The upper confining zone is represented between the ████████ ████████ (nomenclature used by the seismic interpreter) on the 2D seismic line. This low porosity interval's continuity and consistent thickness across the whole seismic line are suitable.

The interpreted well top of the █████████████████████████████████ ██. The blue dashed seismic horizons that were displayed in Figure 1-65, near the well top pick in the pseudo-well, have a few minor gaps in interpretation across the seismic line. The seismic expression is likely due to the Orchard Project area representing a ███████████████████████████ ██ ████████████████████████████████████

Figure 1-66 shows the ███████████████ pseudo-well tie with well log data, a synthetic seismogram, and seismic data for comparison. Figure 1-67 shows the time-to-depth relationship for the pseudo-well tie.
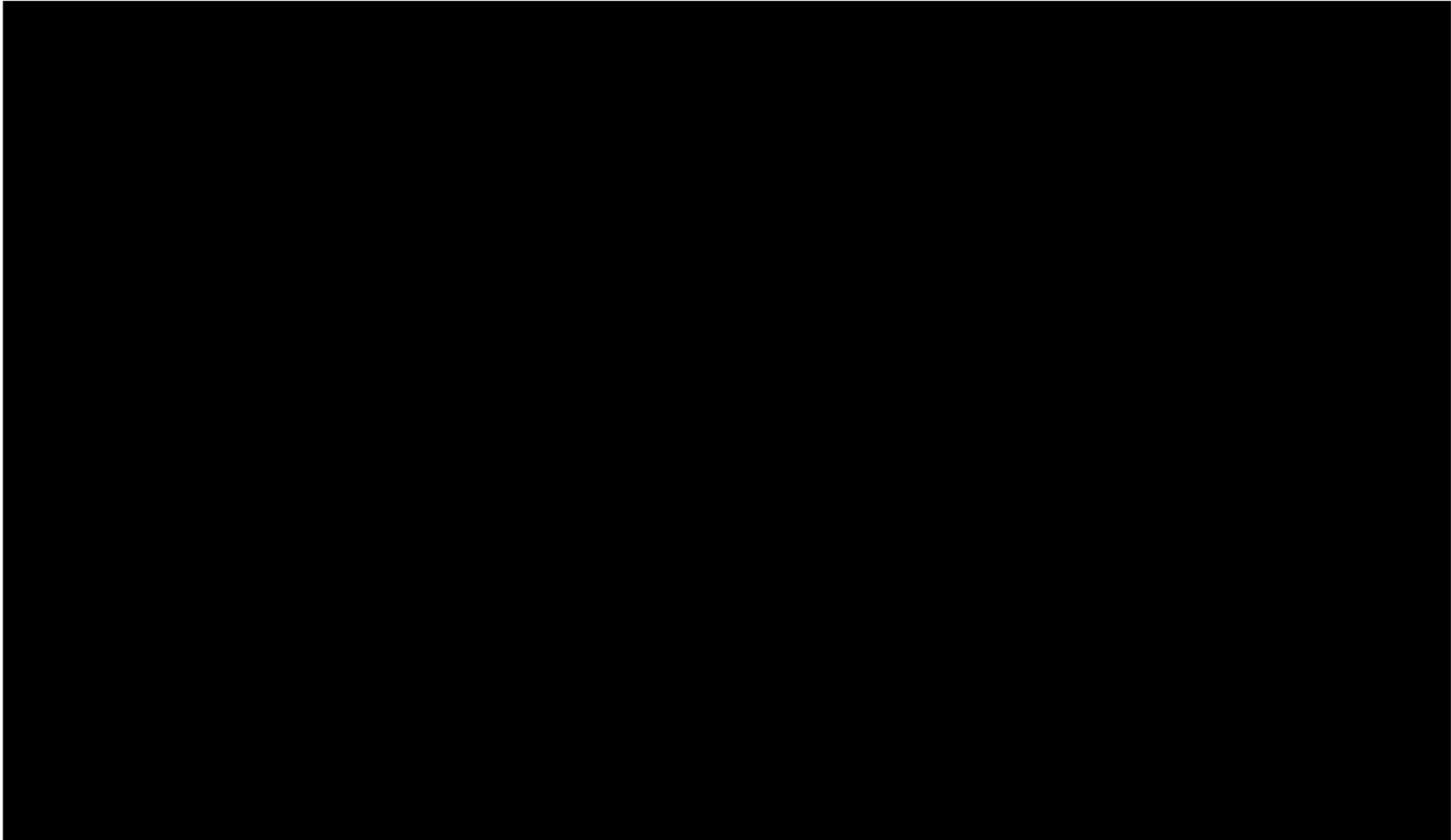
Figure 1-66 – The same 2D seismic line from Figures 1-64 and 1-65, showing the ▮▮▮▮▮▮▮▮▮▮▮ pseudo-well tie, with well log data, a synthetic seismogram overlayed, and seismic data for comparison.
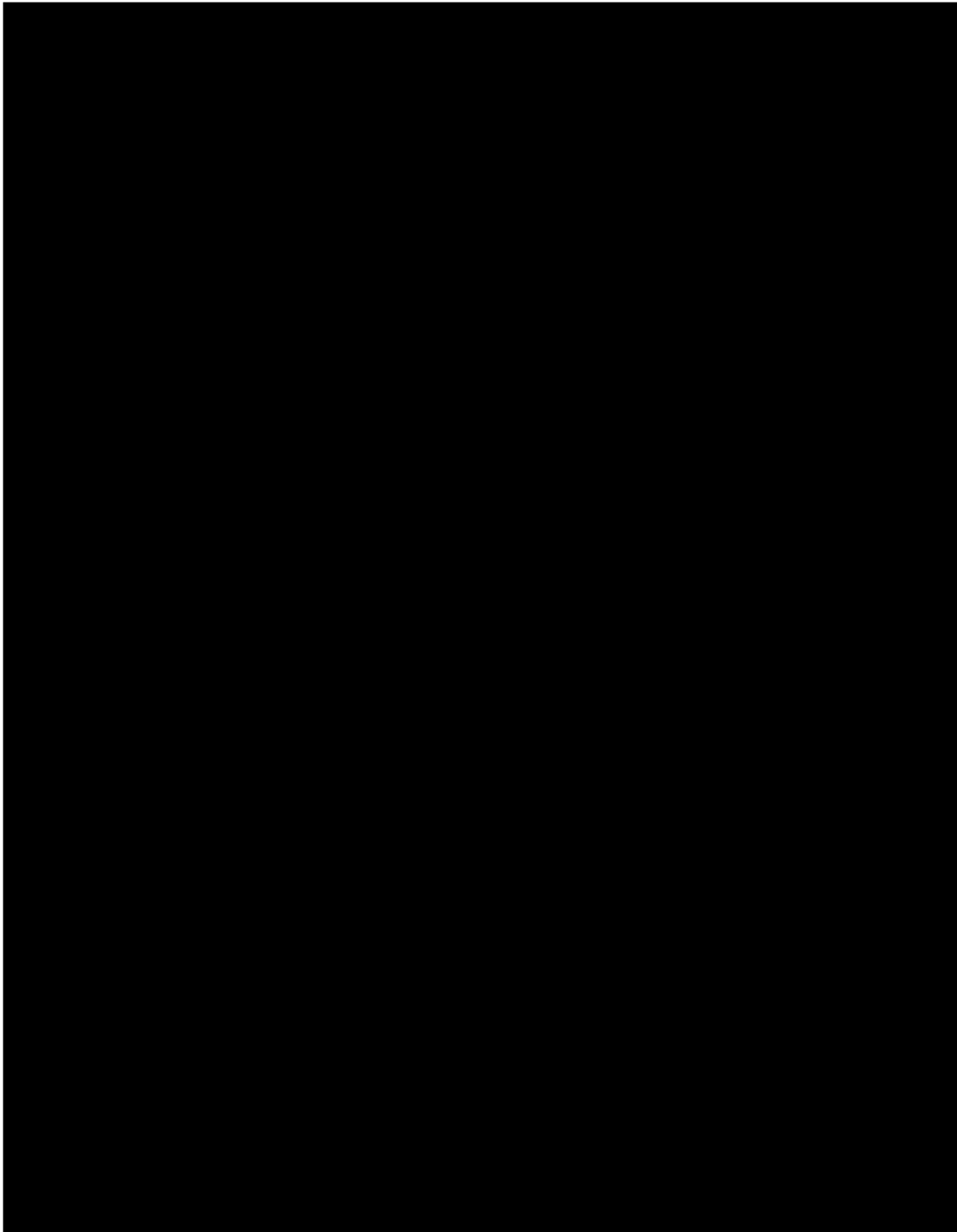
Figure 1-67 – The time-to-depth profile, or relationship, used for the [REDACTED] pseudo-well tie.

The velocity model was derived from the sonic log and adjusted using replacement velocities above the top of the shallowest sonic depth ███████████████████. The time-to-depth relationship for the ████████████████ pseudo-well tie is essentially a 1D velocity model. This model was derived from integrating (i.e., summing up) the sonic log slowness and manual adjustment, using the synthetic seismic correlation with the nearby actual seismic traces.

Analogous shallow velocities above the ███████████████ were obtained from well ████ ████████, located █████ the Orchard Project area. The sonic log curve for this well has a shallower start depth. The velocities were lightly adjusted via stretching and squeezing—an adjustment that is smoother than inserting a single constant replacement velocity in the depths shallower than the ███████████████, but not necessarily more accurate below the ██ ████████. The velocities are almost constant through the ███████████████ well tops. There are minor perturbations, but the major velocity variations are above the ██ ████████████████████.

Across the Orchard Project area, ██████████████████████████████ ██████████████████████. The dip angle of the injection zone top through the project area is approximately █████████████████████████████████. The dip angle of the upper confining zone top through the project area is ███████████████████████ ████████████████. The dip angle of the lower confining zone top through the area is approximately ████████████████████████████.

Figure 1-68 shows a depth map of the top of the injection zone, colored by the dip angle.
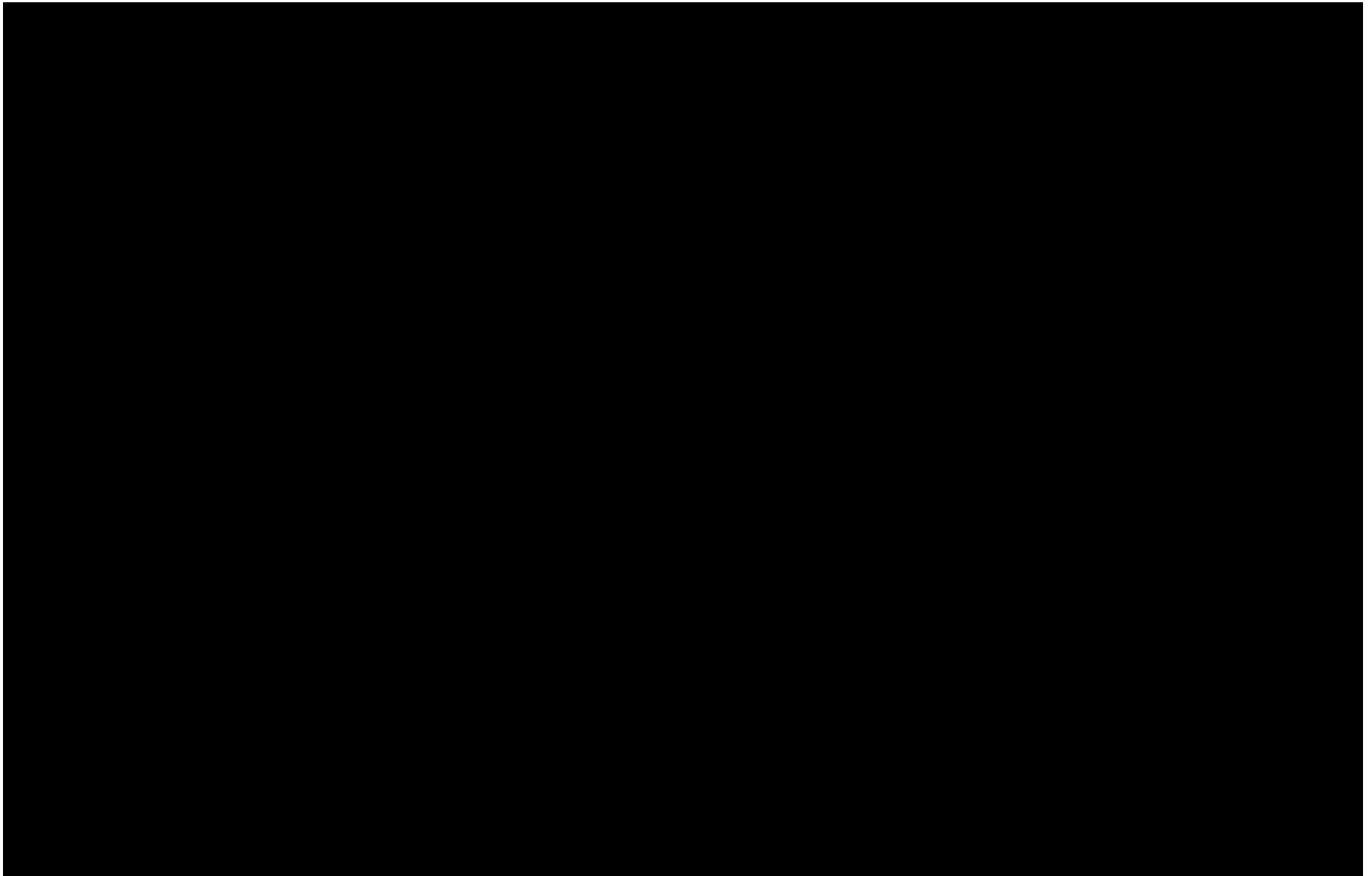
Figure 1-68 – Depth structure map (TVD SS) of the top of the injection zone, colored by dip angle.

Other seismic horizons mentioned in *Section 1.2* were identified to provide quality control of the seismic data and ensure valid injection and confining zone observations. ███████████████████ ██ No significant dip at the ██████████████ horizon was noticeable due to the 2D line (A-A') being perpendicular to the prevailing dip azimuth (to the southwest). ██████████████████████████████████ ██ ██████████████████████████

The ██ that were illustrated in Figure 1-65 (interpreted with a bold-line seismic horizon and a dashed-green-line seismic horizon, respectively, in *Section 1.4*) are part of a ██████████████████████████████████ ██ ██ ██ ██ ██ ██ ██████████████

1.4.2 Fault Interpretation

No publicly available maps or other published sources of information were identified during this site characterization that indicated the existence of faults and fracture networks within the vicinity of the Orchard Project area. A thorough fault interpretation on the seismic 2D line was completed and tied to the regional structural model.

Fault tips are deeper than the lower confining zones. No faults were interpreted shallower than the ████████████ The fault interpretation correlates to the regional fault model, where most tectonic deformation ends in the ████████████████████████████████████ ██ ██ No faults were observed between the wells used for well top picking (e.g., no major vertical offset between wells, and no missing or repeated intervals on the well logs).

The Permian Basin has been shaped by several extensional and contractional deformation events through geologic time (Horne et al., 2021). ████████████████████████ ██ ██ ██ ██ ██████████████████████████

Figure 1-69 shows the ██
██
███████████

Figure 1-69 – Diagram showing tectonic events by geologic age for the ███████████████████
███████████████████████████

Figure 1-70 shows a regional fault map. Researchers at the TexNet Seismic Monitoring and Center for Integrated Seismicity research group have made a concerted effort to better understand the causative hazards associated with induced seismicity across the state of Texas.
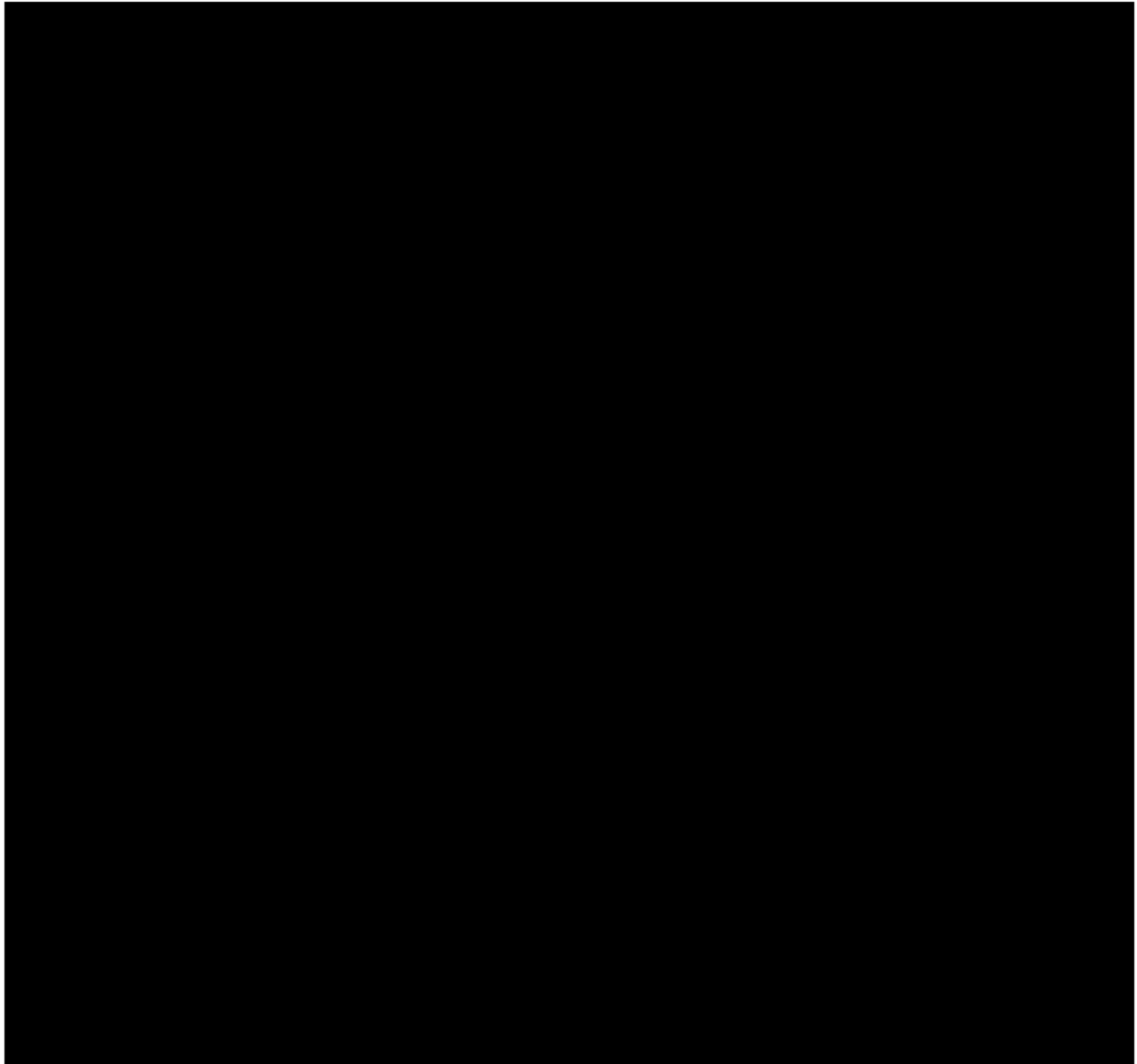
Figure 1-70 – Regional fault map generated by researchers at the TexNet Seismic Monitoring and Center for Integrated Seismicity research group (https://www.beg.utexas.edu/texnet-cisr/fault-maps).

The 2D seismic-line trajectory (north-south) is roughly perpendicular to the dominant regional fault strike and the present-day stress (S_H maximum) direction. The present-day slip potential of this faulting regime (from Snee and Zoback, 2018) in this part of the Permian Basin is associated with the normal-type state of stress.

1.5.   Geomechanics

Data from site-specific and publicly available publications were used to generate the geomechanical model for this site characterization. The model contains three parts:

- Elastic moduli
- Local stress conditions
- Fracture gradients

1.5.1   Elastic Moduli

Dynamic elastic moduli were calculated based on ██████████████ as this well had both shear and compressive sonic well logs available through the injection and confining zones. Figure 1-20 (in *Section 1.3.2*) provided the type well, showing the petrophysical analysis and dynamic elastic moduli.
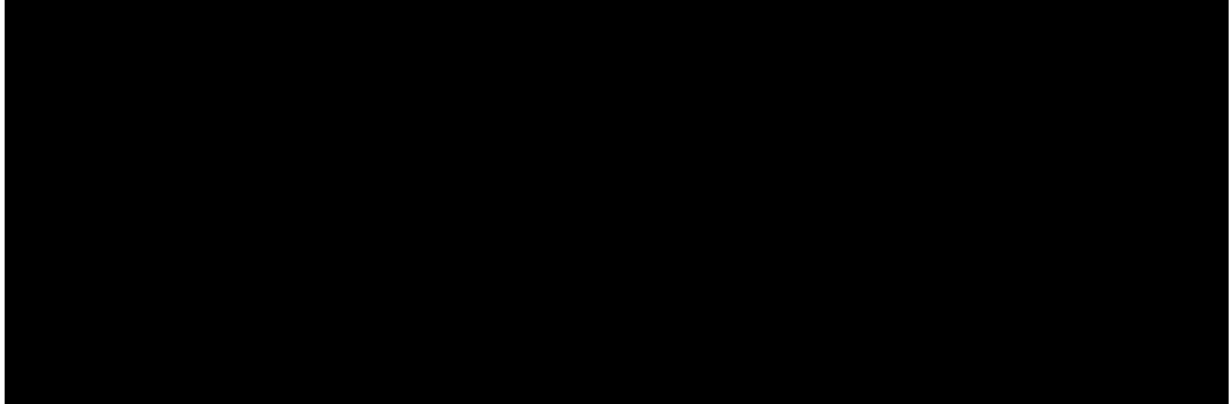
The geomechanical well logs demonstrate the elastic mismatch between the injection zone and the upper and lower confining zones. The differing geomechanical properties reduce the ability of any fractures caused by injection well operations to propagate above or below the injection zone.

Static elastic moduli were estimated from core analysis using samples from ██████████████ ██████████████████████████ Triaxial tests were performed on six vertical core plugs (three from each well), including the basal part of the upper confining zone and the upper part of the injection zone.

Table 1-6 shows the triaxial test results for the six samples. A pronounced elastic moduli variation is exhibited between the injection and upper confining zones, as was observed by the dynamic elastic moduli calculations. This difference adds confidence in the upper confinement zone's ability to prevent the initiation and propagation of fluid-conductive fractures upwards due to the increased pore pressure in the injection zone below.

Table 1-6 – Triaxial Test Results for Six Samples

Well API No.	Depth (ft)	Zone	Confining Pressure (psi)	Bulk Density (g/cm³)	Compressive Strength (psi)	Young's Modulus (10⁶ psi)	Poisson's Ratio

Figure 1-71 shows photographs of samples taken after the triaxial testing was completed
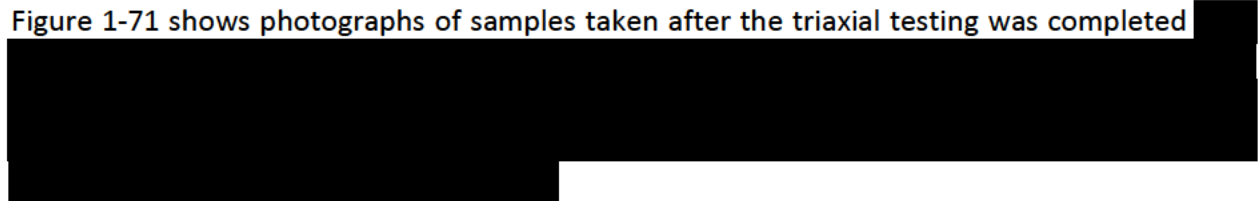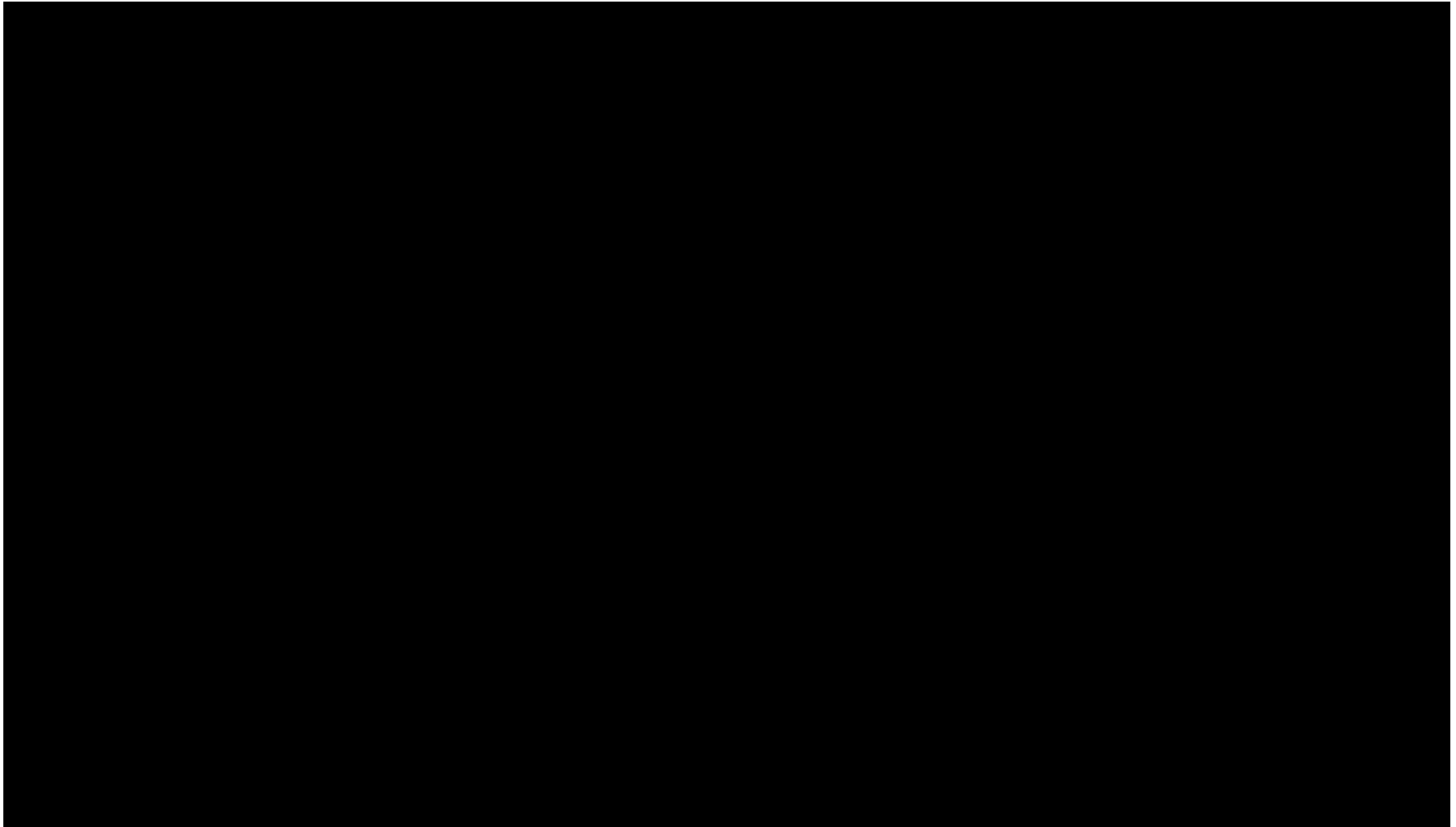
Figure 1-71 – Photographs of samples taken after triaxial testing for well ▮▮▮▮▮▮▮▮▮▮. The injection zone samples' deformation style appears to be a mix between tensile and shear.
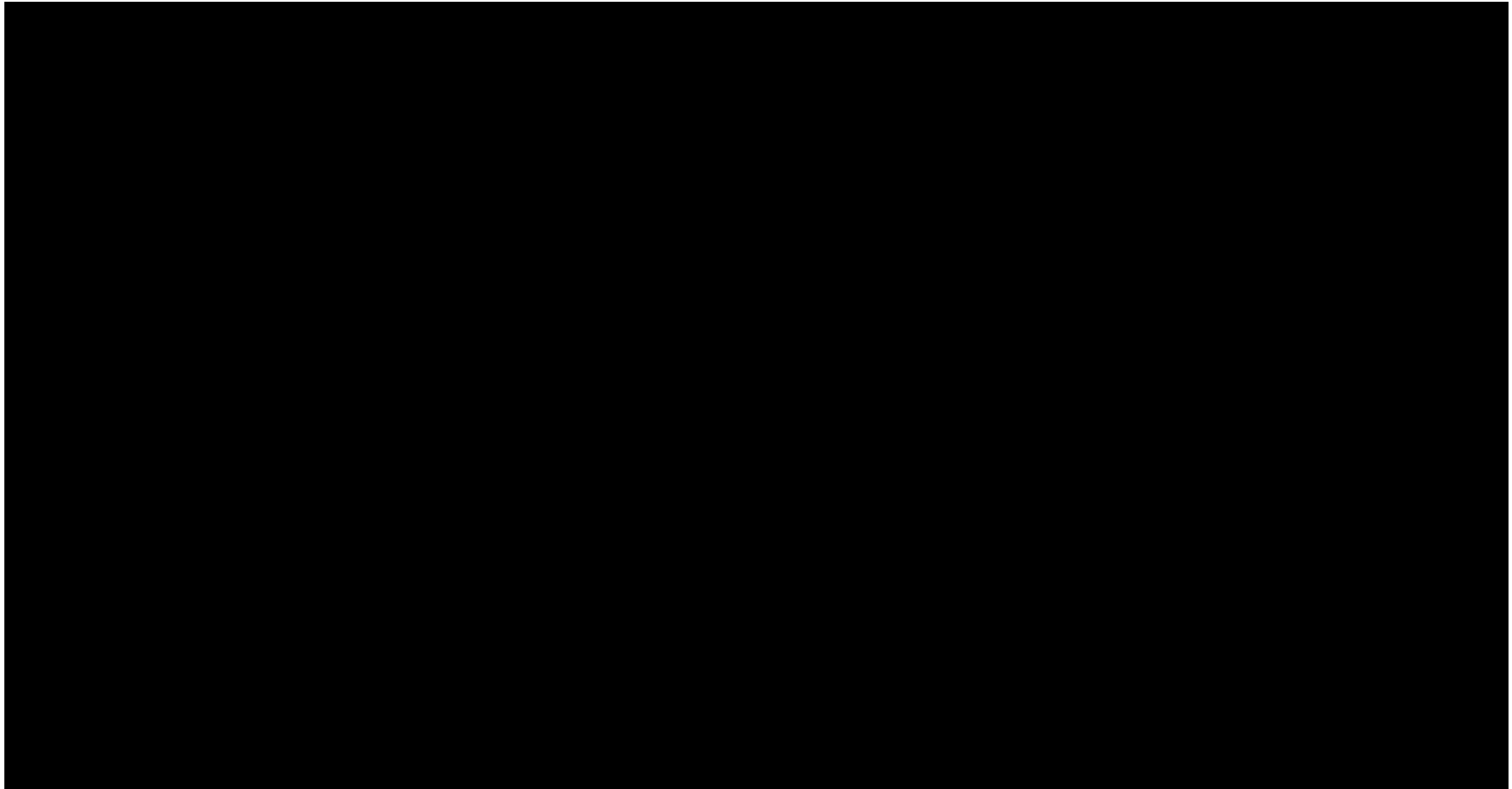
Figure 1-72 – Photographs of samples taken after triaxial testing for well ███████████████. The confining zone samples' deformation style appears to be a mix between tensile and shear.

1.5.2   Local Stress Conditions

The lithostatic, or overburden, stress (S_v) gradient used in the geomechanical model is ███████ per square inch (psi)/ft. The pore pressure gradient is estimated at █████ psi/ft.

The azimuth of maximum horizontal stress (S_H maximum) in the Orchard Project area is approximately ████████ (Snee & Zoback, 2018) as shown in Figure 1-73. This study also demonstrated that the principal stress regime is normal in the project area. ████████████████ ██ ████████████████
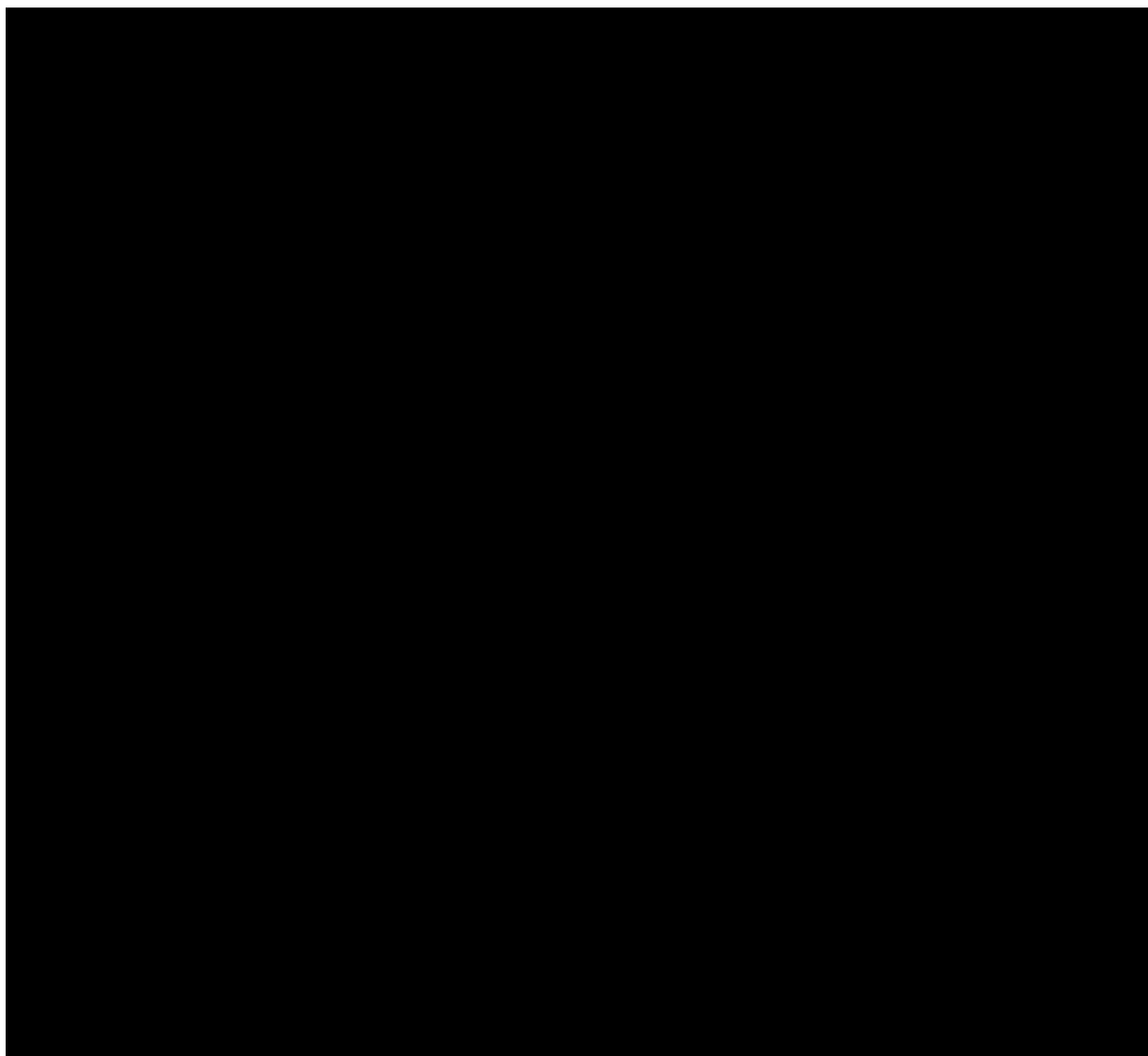
Figure 1-73 – Regional map showing the maximum horizontal stress orientation across the Permian Basin derived from a combination of well data and seismicity (Snee & Zoback, 2018).

A method to predict a simplified fracture gradient is the standard Eaton equation (i.e., S_h minimum horizontal stress, or fracture closure pressure). Eaton's equation is shown below:

$$P_f = (v / 1 - v) * (S_v - P_p) + P_p$$

Where:
P_f = fracture closure pressure gradient
v = Poisson's ratio
S_v (overburden stress gradient) = 1.0
P_p (pore pressure gradient) = 0.433.

Biot's constant was based on approximate dynamic elastic moduli calculated using the equation based on data from Detournay & Cheng (1993):

$$a = 0.62 + 0.935 * phi$$

Where phi = porosity.

The minimum stress equation (Barree, 2009) used to estimate the fracture closure pressure is below:

$$Pf = (v / 1 - v) * (S_v - a_v * P_p) + a_h * P_p [+ \varepsilon_x * E + \sigma_t]$$

Where:
P_f = fracture closure pressure gradient
v = Poisson's ratio
S_v (overburden stress gradient) = 1.0
P_p (pore pressure gradient) = 0.433
a = Biot's constant (vertical is calculated and horizontal = 1).

(Not used, but shown above, ε_x is regional horizontal strain, E is Young's modulus, and σ_t is regional horizontal tectonic stress.[1])

The following dynamic elastic moduli ███████████████████████ were calculated using well logs using methods summarized in Crain's Petrophysical Handbook:

- Shear Modulus (G)
- Poisson's ratio (v)

---

[1] Note: The above results do not account for external stress boundary conditions, and are not representative of the (higher value) breakdown pressure of the injection and confining zones.

- Young's modulus (E)
- Bulk modulus (Kb)
- Biot's constant (a)
- Minimum horizontal stress (S_h)

1.5.3 Injection Zone Fracture Gradient

The minimum horizontal stress and fracture gradient were calculated using the elastic moduli calculated from three triaxial tests in the upper part of the injection zone. Table 1-7 shows the estimated fracture gradient at triaxial test depths and select depths in the injection zone and confining zone.

Table 1-7 – Estimated fracture gradient in the injection zone and confining zone using well logs (dynamic elastic moduli) and well core (static elastic moduli) samples.

Depth (ft)	Zone	Sample	Lithostatic Stress (psi)	Pore Pressure (psi)	Porosity (dolomite)	Biot's Constant	Minimum Fracture Closure Gradient (psi/ft)

The triaxial core test results were used to generate failure envelopes for the ███████ injection interval. Mohr circle analysis was applied to two stress conditions at a depth of ████ TVD. Figure 1-74 shows that, at in situ conditions, the rock is stable—as expected. Figure 1-75 shows an *unstable* condition based on the triaxial core failure data, with the predicted Mohr circle at an unstable state of stress. Cohesive strength was derived using the approximate differential stress of ████████████████████████████████ test core samples. Table 1-8 provides the parameters used to develop the Mohr circle analysis.

Table 1-8 – Mohr Circle Analysis Parameters

Parameter	Value
███	
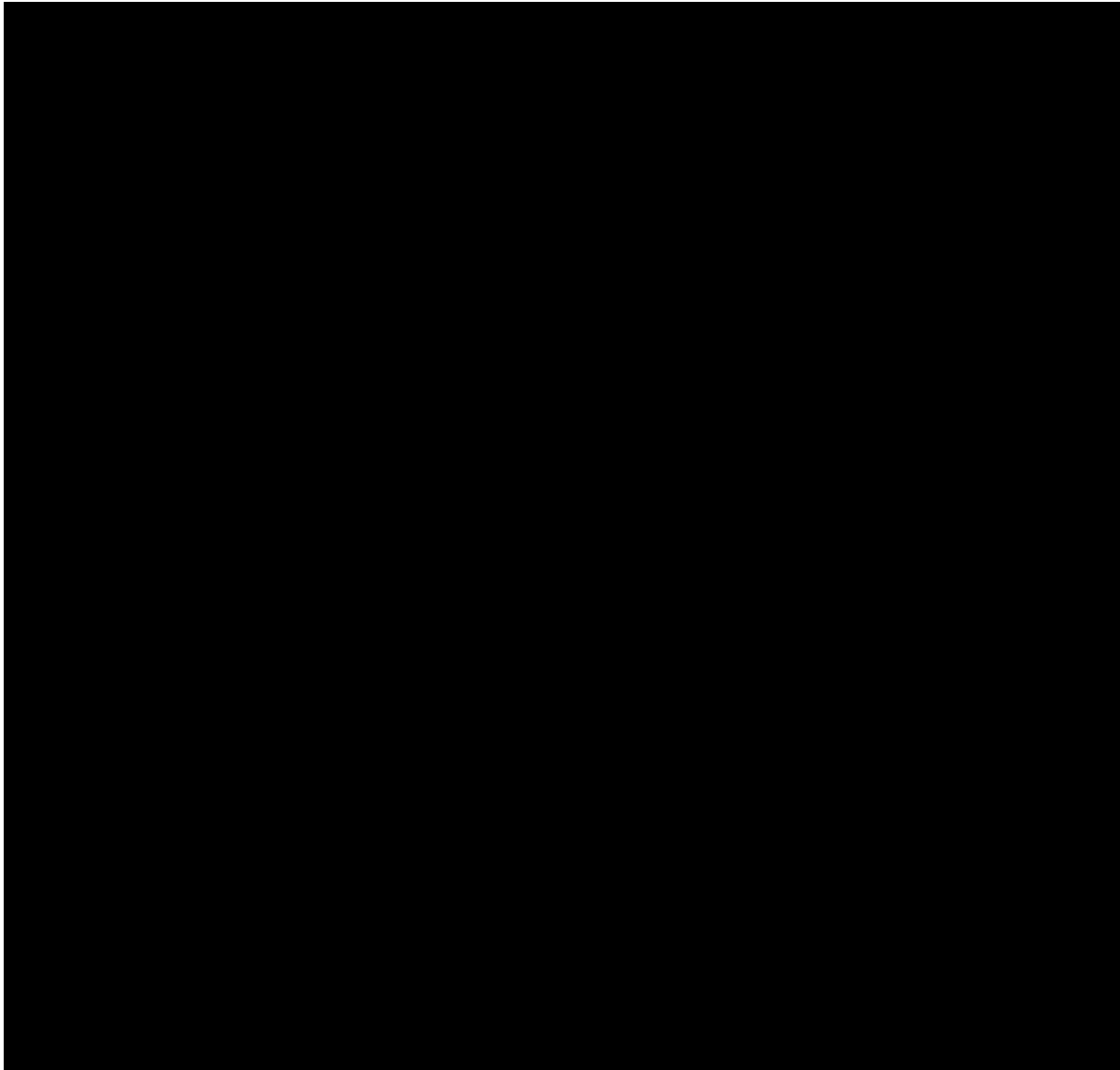
Figure 1-74 – Mohr Circle Analysis—Stable State of Stress (in Megapascals)
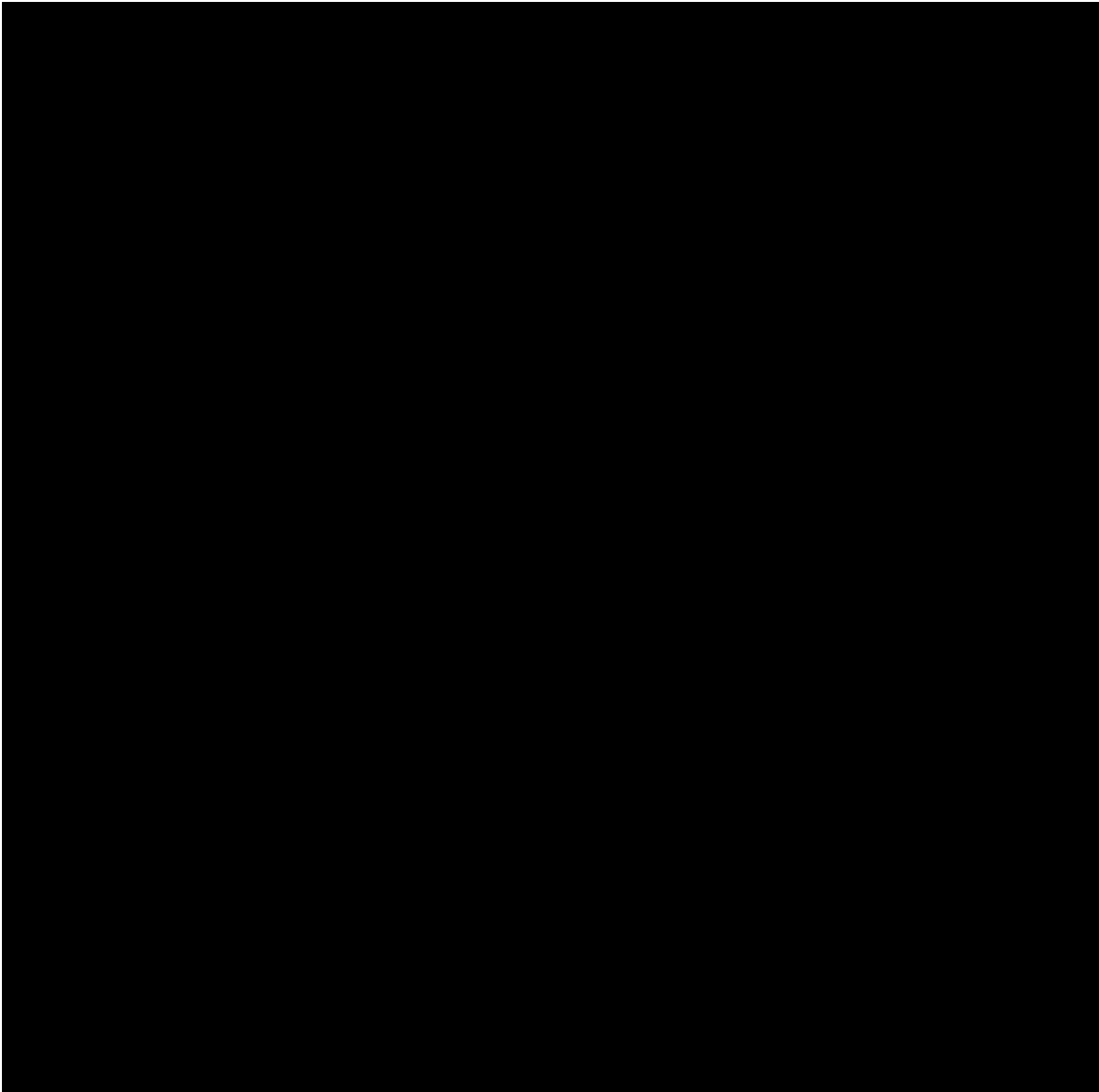
Figure 1-75 – Mohr Circle Analysis—Unstable State of Stress (in Megapascals)

1.6. Geochemistry

This section discusses the fluid and solid-phase geochemistry in the Orchard Project site and wider area.

1.6.1 Fluid Chemistry (Injection Zone)

Laboratory analyses of produced water from the ▮▮▮▮▮▮▮▮▮▮▮▮ in adjacent hydrocarbon fields have been used to understand the range and likely salinity of the injection zone water in the Orchard Project area. Figures 1-76 and 1-77 show examples of historical results from several laboratory analyses within the ▮▮▮▮▮▮▮▮▮▮▮▮▮▮▮▮▮▮. Further details are provided in *Section 3 – Area of Review and Corrective Action Plan*. The selected total dissolved solids (TDS, or equivalent), representative of the ▮▮▮▮▮▮▮▮▮ in the project area, is ▮▮▮▮ parts per million.
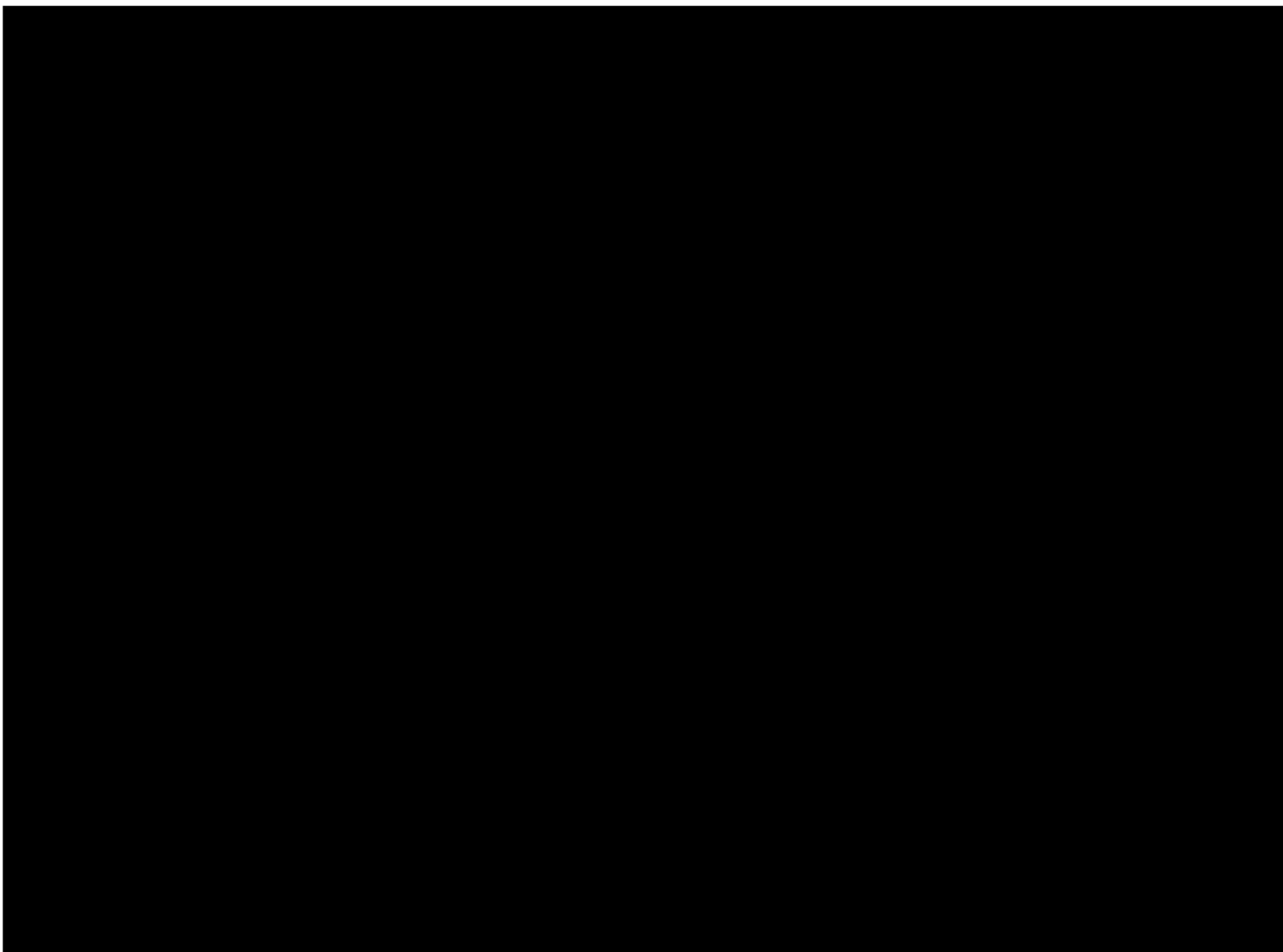
Figure 1-76 – Tabulated records of water quality from the Texas Water Development Board's Saline Water Resources Survey of the State of Texas for Gaines County (1971).
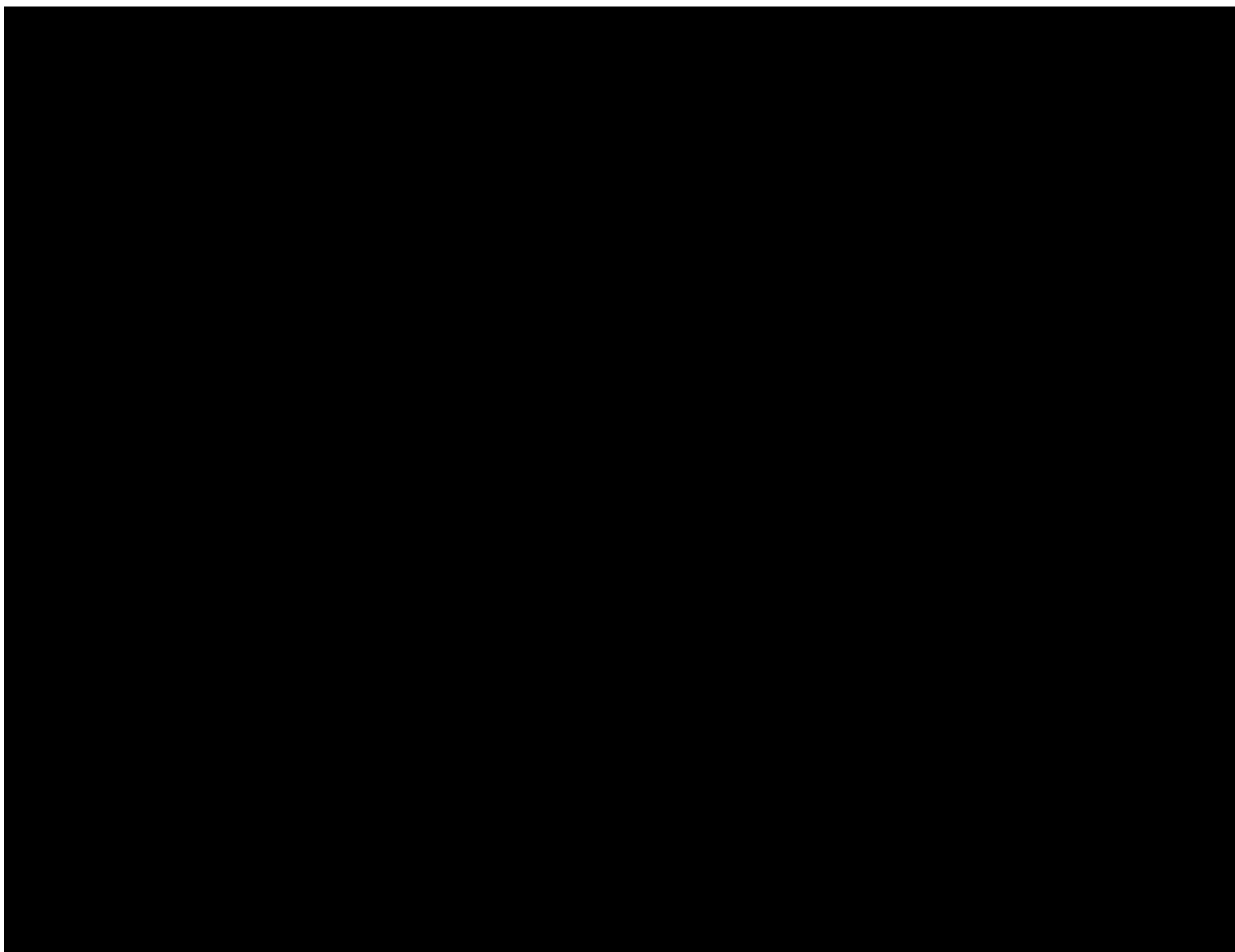
Figure 1-77 – Tabulated records of water quality (continued) from the Texas Water Development Board's Saline Water Resources Survey of the State of Texas for Dawson County (1971).

Results of the proportions of water versus hydrocarbons within the injection zone area are included in *Section 1.3.2*. A description of the hydrocarbon composition and chemistry is included in *Section 2 – Plume Model.*

1.6.2   Rock Chemistry (Injection Zone and Upper Confining Zone)

Three x-ray diffraction (XRD) samples (two in the injection zone and one in the confining zone) were acquired from existing core. Table 1-9 shows the mineralogy determined by XRD for both cored wells.

Table 1-9 – Mineralogy determined by XRD for both cored wells ███████████████████████████████

[BLACK REDACTED BLOCKS]

1.6.3   Simulated Interactions (Injection Zone and Upper Confining Zone)

No geochemical modeling or simulations were done to identify major reactions that may occur in either the injection or confining zone. Regional research and analog projects offer some insight into possible interactions with fluid or rocks with injected supercritical CO_2 in the near- and long-term.

A Department of Energy (DOE) funded investigation in 2002, led by Grigg et al. [BLACK REDACTED]

[BLACK REDACTED BLOCKS]

1.7.   Site Evaluation of Mineral Resources

While regional economic oil-and-gas production is prolific in the Permian basin in West Texas and Southeastern New Mexico, the Orchard Project is located near the [BLACK REDACTED] in Gaines County, Texas. This portion of the Midland Basin is far less suitable for recovering oil and gas in economic quantities.

A thorough review of oil-and-gas plays was conducted to avoid any potential conflicts with economic oil-and-gas production in the Orchard Project area. Within the project area of review (AOR), as defined in Section 3.5 and 3.6, [BLACK] oil and gas wells were drilled. Of the [BLACK] wells drilled, [BLACK REDACTED] produced at economic quantities (cumulative production greater than 100,000 barrels of oil equivalent). [BLACK REDACTED]

[BLACK REDACTED BLOCKS]

Other oil and gas activity in the immediate Orchard Project area is minimal. ████████████ fields are shown on Figure 1-13. With the Permian Basin having been the most actively developed basin in North America during the last two decades, one would expect both historical and present activities in the greater Orchard Project area to be much higher—if it were considered attractive to mineral or working interest owners as an opportunity for economic oil or gas production.

1.8.   Seismic History

Figure 1-78 shows two maps of historical seismic events in the Permian Basin area. The top map is USGS data of seismic events of more than 2.5 magnitude from 1900 to the present. The bottom map is from TexNet data for seismic events of more than 1.5 magnitude from 2017 to the present. Neither data source shows seismicity occurrences in the Orchard Project vicinity.
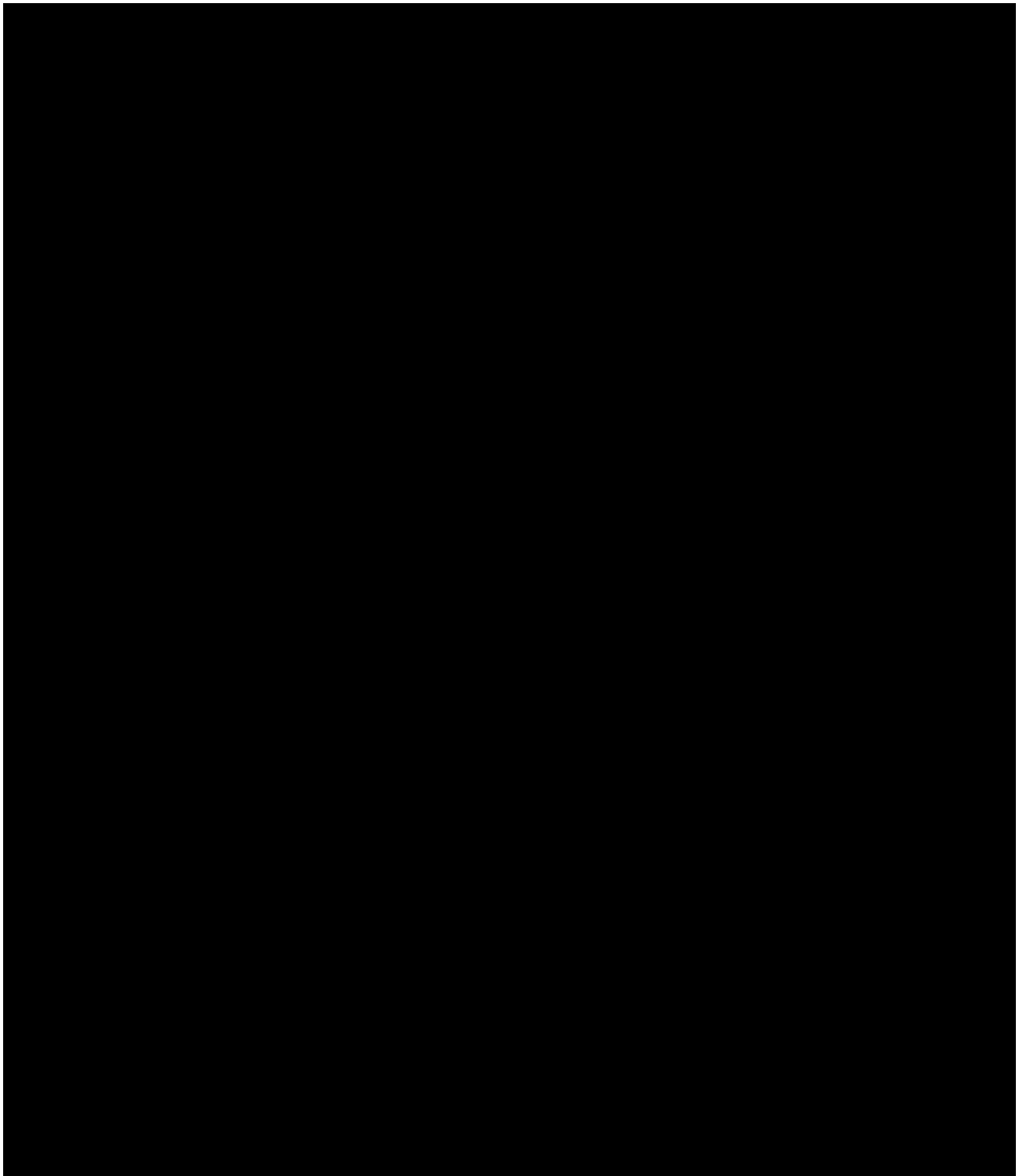
Figure 1-78 – Two maps of historical seismic events in the Permian Basin area; the upper map is from USGS, the lower from TexNet. Neither data source shows seismicity occurrences in the Orchard Project vicinity (indicated by the black star).

The Bureau of Economic Geology's TexNet site identifies a permanent active monitoring station ███████████████ the Orchard Project area, adding confidence that if a seismic event had occurred in or near the project area, it would have been detected.

As discussed previously, there is a low probability of faults or fracture zones within the vicinity of the Orchard Project area injection zone that would pose an induced seismicity risk caused by CO_2 injection. Furthermore, there is an absence of active disposal wells within the project site. Areas with active disposal wells may have an increased induced-seismicity risk by injecting into deeper intervals where seismic data has revealed faults.

1.9. Site Suitability

The following is based on synthesis of the above site characterization work completed for this application. As shown in *Section 2 – Plume Model*, the injection zone has pore volume available for sequestration of injected CO_2, and the confining zone has sufficient integrity to contain the fluid—to prevent leakage into a USDW.

1.9.1 Lithofacies
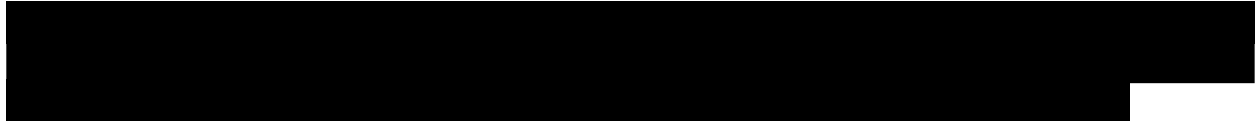
1.9.2 Leakage Pathways

Site-specific data and regional understanding show a low probability of the occurrence of faults or fractures causing leakage of injected CO_2. The confining zone above the injection zone has good continuity and sufficient low porosity to provide a high probability of containment.

1.9.3 Hydrology and Hydrogeology
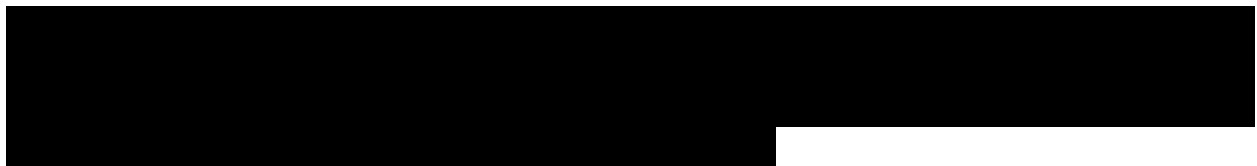
Figure 1-79 shows a simplistic cross section of the major and minor aquifers across the region and through the Orchard Project area in Gaines County (George et al., 2011).
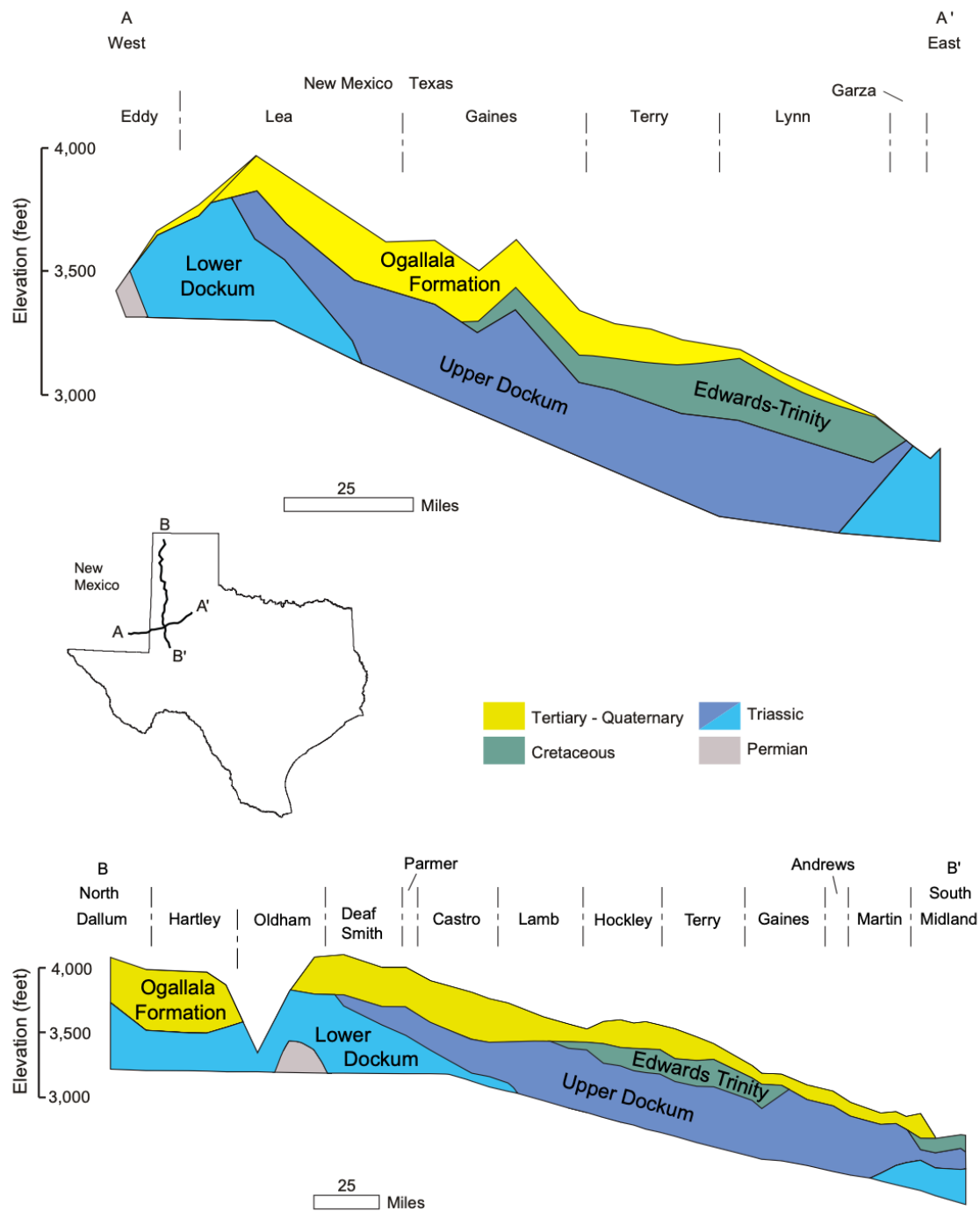
Geologic cross sections showing the relationship
of the Ogallala Formation to underlying strata
(modified from McGowen and others, 1977).

Figure 1-79 – Simplified cross section of the major and minor aquifers across the region and through the Orchard Project area in Gaines County, Texas (George et al., 2011).

The Dockum aquifer, the oldest of the three discussed aquifers, was formed in the Triassic and underlies the Cretaceous Trinity and Fredericksburg Groups (Teeple et al., 2021). The TDS meet or exceed 5,000 mg/l; therefore, the aquifer is considered brackish. The Edwards-Trinity aquifer is of Cretaceous age, with the Trinity Group Antlers formation and Fredericksburg Group limestones being the primary sedimentary constituents of the aquifer. The infiltration of freshwater into the Edwards-Trinity system is primarily from the overlying Ogallala aquifer (George et al., 2011). The Ogallala aquifer is Tertiary in age and produces the majority of freshwater for Gaines and surrounding counties.

Figure 1-80 features a map showing the distribution of TDS in groundwater from the Dockum aquifer (Ewing et al., 2008).
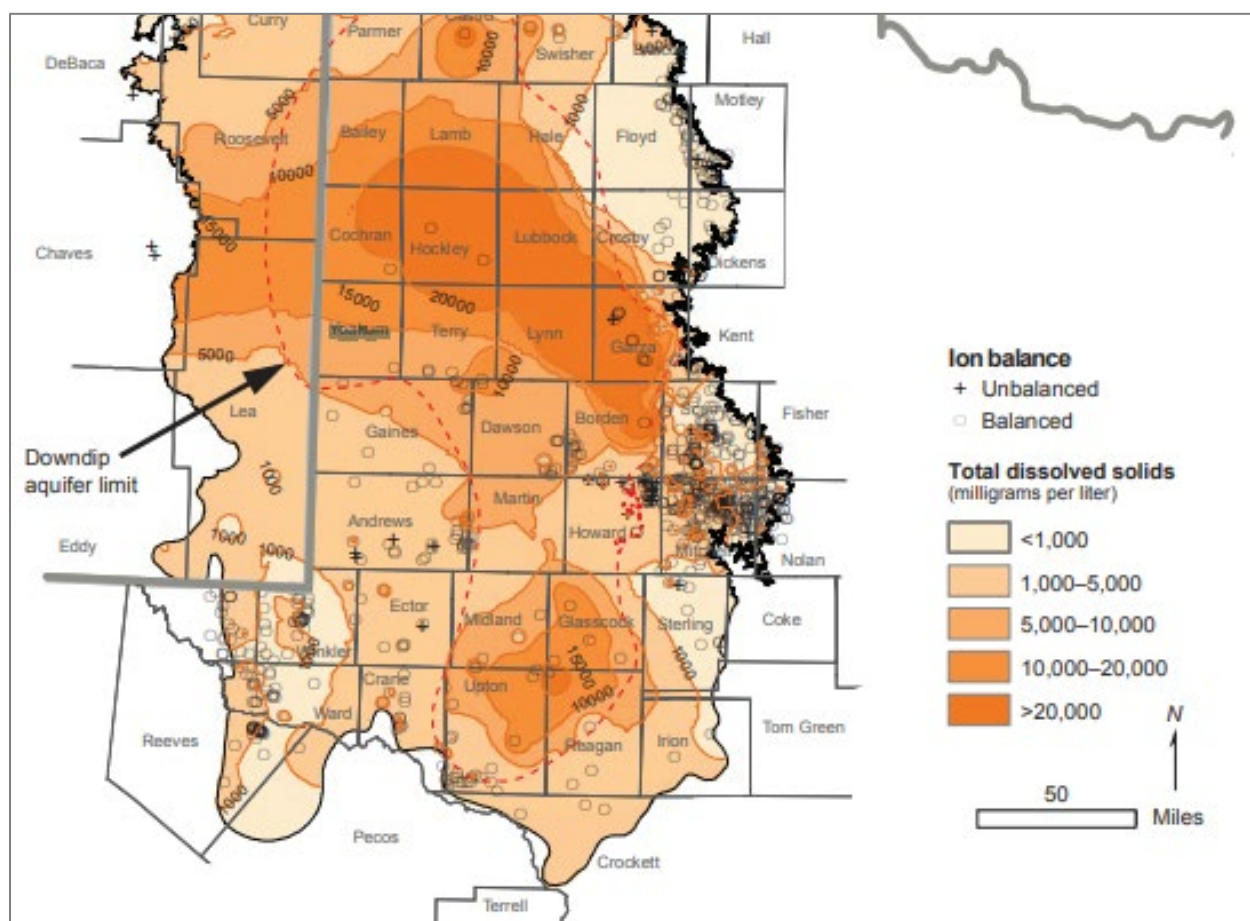
Figure 1-80 – Map showing the distribution of TDS in groundwater from the Dockum aquifer (Ewing et al., 2008).

The Texas Railroad Commission (TRRC) Groundwater Advisory Unit (GAU) identified the base of a USDW at a depth of ██
██
██

[black redaction bars]

1.9.4 Total Storage Capacity

A simple experiment using the 3D numerical model demonstrates the total pore volume within a 1-kilometer radius surrounding the injection wells' locations. [black redaction]

Similar results were produced when using the CO2-SCREEN[2] tool. Using the saline model parameters, the range of total storage capacity in the [black redaction]

1.9.5 Injection Capacity

Several iterations of the porosity and permeability model have incorporated site-specific data, regional geologic frameworks, and subsurface analog information to reduce uncertainty around the quality of the injection zone in the Orchard Project area. [black redaction]

1.9.6 Secondary Confinement

Based on the site-specific data and regional perspective of the upper confining zone, a secondary upper confining zone is not necessary to ensure USDW protection. The site characterization for the Orchard Project identified the secondary upper confining zone directly above the primary upper confining zone as one with sufficient integrity to prevent migrating fluid from reaching the USDW. Both confining zones are vertically heterogeneous and relatively thinly bedded.

---

[2]DOE's NETL developed CO2-SCREEN (CO_2 Storage prospeCtive Resource Estimation Excel aNalysis) to screen saline formations for prospective CO_2 storage resources.

1.10. <u>Further Site Characterization</u>

Several topics below are opportunities for future work to increase the accuracy and reduce the uncertainty of the Orchard Project site characterization. Much of this information will be acquired during the drilling of the initial well and incorporated into the site characterization and plume modeling and the application updated as needed.

1.10.1 Core

Further core analysis will be performed when confining and injection zone cores are obtained. Testing may include thin-section description, mercury injection, core description (confining zone), XRD, scanning electron microscopy, relative permeability (CO_2, brine), etc.

1.10.2 Sequence Stratigraphy

Depending on additional core analyses and seismic data, the current stratigraphy may be refined to represent a stratigraphic-sequence framework closely aligned to the higher-frequency cycles within the regional geologic framework (shown in *Section 1.2*). The current stratigraphic framework in the conceptual model, which was used to create the numerical simulation model, includes the major stratigraphic boundaries only ███████████████████████

1.10.3 Facies

Similar to increasing the resolution of the stratigraphic-sequence framework in the Orchard Project site and wider area, testing the effect on the porosity and permeability model by lithological and facies changes spatially may help reduce uncertainty. The purpose would be to create facies logs in multiple wells. The facies log may be related to core-described facies and expectations based on the regional depositional model.

1.11. <u>References</u>

Alimahomed, F., Haddad, E., Velez, E., Foster, R., Downing, T., Seth, C., Melzer, S., Downing, W. (2018). The San Andres Play: Observations and Challenges in Horizontal Wells on the Central Basin Platform, Permian Basin. *Society of Petroleum Engineers*.

Andreason, M.W. (1992). Coastal siliciclastic sabkhas and related evaporative environments of the Permian Yates Formation, North Ward-Estes Field, Ward County, Texas. *American Association of Petroleum Geologists Bulletin, Vol. 76, No. 11, P. 1735-1759.*

Atchley, S.C., Kozar, M.G., Yose, L.A. (1999). A Predictive Model for Reservoir Distribution in the Permian (Leonardian) Clear Fork and Glorieta Formations, Robertson Field Area, West Texas. *AAPG Bulletin, Vol. 83, No. 7, P. 1031-1056*.

Barree, R.D. (2009). Input Data for Frac Design Models. *Barree & Associates LLC, 2009 Seminar*.

Beaumont, Christopher (1981). Foreland basins. *Geophys. J. R. Astr. Soc., V. 65, P. 291-329*.

Beaver, James L. (1982). Deposition and Diagenesis of Abo and Wichita Carbonates, Northern Midland Basin, Texas. *Texas Tech University Libraries*. Retrieved from http://hdl.handle.net/2346/9495

Bhatnagar, P., Scipione, M., Verma, S., Bianco, R. (2018). Characterization of mass transport deposit using seismic attributes: Spraberry formation, Midland Basin, West Texas. *SEG International Exposition and 88th Annual Meeting*.

Bhatnagar, P., Verma, S., Bianco, R. (2019). Characterization of mass transport deposits using seismic attributes: Upper Leonard Formation, Permian Basin. *Society of Exploration Geophysicists and American Association of Petroleum Geologists, Interpretation, Vol. 7, No. 4, P. 1-14*.

Bhatnagar, P., Verma, S., Trentham, R., Zobaa, M., Bianco, R., Watson, S. (2018). Geomorphologic Character of an Upper Leonardian Mass Transport Deposit, Midland Basin: Insights from 3D Seismic Data. *The University of Texas of the Permian Basin*. Retrieved from https://www.researchgate.net/publication/335150144

Borer, J.M., Harris, P.M. (2009). Computer Simulation of the Yates Formation (Permian, Delaware Basin) – Sequence Stratigraphy and Shelf-to-Basin Correlation Implications. *AAPG Search and Discovery Article No. 60044*.

Borer, J.M., Harris, P.M. (1991). Lithofacies and cyclicity of the Yates Formation, Permian Basin: implications for reservoir heterogeneity. *American Association of Petroleum Geologists Bulletin, Vol. 75, No. 4, P. 726-779.*

Brown, A.A., Loucks, R.G. (2016). Geological Controls on Evaporite – Carbonate Facies Transition in Permian Seven Rivers Formation, SE New Mexico. *AAPG Search and Discovery Article No. 51317*.

Browning, J., Gorrell, S.B., Asquith, G.B., Henderson, S.K., Watson, M.C., Sheridan, M. (2021). Evaluating the San Andres Horizontal Play in the Northwest Shelf of the Permian Basin, Developing Best Practices for Exploration. *Texas Tech University Libraries*. Retrieved from https://hdl.handle.net/2346/87838

Burnside, N.M., Naylor, M. (2014). Review and implications of relative permeability of CO_2/brine systems and residual trapping of CO_2. *International Journal of Greenhouse Gas Control, Vol. 23, P. 1-11*. Retrieved from http://dx.doi.org/10.1016/j.ijggc.2014.01.013

Caf, A.B., Pigott, J.D. (2021). Dolomitization geometry and reservoir quality from supervised Bayesian classification and probabilistic neural networks: Midland Basin Leonardian Wichita and Clear Fork Formations. *Society of Exploration Geophysicists and American Association of Petroleum Geologists, Interpretation, Vol. 9, No. 2, P. T585-T598*. Retrieved from http://dx.doi.org/10.1190/INT-2020-0204

Davis, Ken E. & Associates (1988). Survey of Methods to Determine Total Dissolved Solids Concentrations. *U.S. Environmental Protection Agency, Underground Injection Control Program, EPA LOE Contract No. 68-03-3416*.

Detournay, E., Cheng, A.H.D. (1993). Fundamentals of Poroelasticity. *Comprehensive Rock Engineering: Principles, Practice and Projects, Vol. 2, P. 113-171.*

Draper, C.H., Kerans, C., Wahlman, G.P., Janson, X. (2019). Wolfcampian Shelf-to-Basin Stratigraphic Framework of the Central Basin Platform and Midland Basin, Andrews County, Texas. *The University of Texas at Austin, Jackson School of Geosciences*.

Dutton, A.R. (1987). Origin of brine in the San Andres Formation, evaporite confining system, Texas Panhandle and eastern New Mexico. *Geological Society of America Bulletin, Vol. 99, P. 103-112.*

Dutton, S.P., Kim, E.M., Broadhead, R.F., Breton, C.L., Raatz, W.D., Ruppel, S.C., Kerans, C. (2004). Play Analysis and Digital Portfolio of Major Oil Reservoirs in the Permian Basin: Application and Transfer of Advanced Geological and Engineering Technologies for Incremental Production Opportunities. *The University of Texas at Austin, Bureau of Economic Geology, and New Mexico Bureau of Geology and Mineral Resources*.

Eaton, B.A. (1969). Fracture Gradient Prediction and its application in Oilfield Operations. *Journal of Petroleum Technology, SPE-2163-PA*. Retrieved from https://doi.org/10.2118/2163-PA

Engle, M.A., Reyes, F.R., Varonka, M.S., Orem, W.H., Ma, L., Ianno, A.J., Schell, T.M., Xu, P., Carroll, K.C. (2016). Geochemistry of formation waters from the Wolfcamp and "Cline" shales: Insights into brine origin, reservoir connectivity, and fluid flow in the Permian Basin, USA. *USGS, Chemical Geology Vol. 425, P. 76-92.*

Ewing, J.E., Jones, T.L., Yan, T., Vreugdenhill, A.M. (2008). Groundwater Availability Model for the Dockum Aquifer – Final Report. *Prepared by INTERA Inc. for Texas Water Development Board, Austin, Texas.*

Ewing, T.E. (2019). Tectonics and Subsidence in the West Texas (Permian) Basin: A Model for Complex Intracratonic Basin Development. *AAPG Search and Discovery Article No. 30606.*

Fairhurst, B., Ikonnikova, S., Dommisse, R., Hamlin, S., Carr, D., Gherabati, A., Male, F., Yurchenko, I. (2019). Reconstructing the Permian Basin for Wolfberry and Wolfbone Unconventional Assessment. *The University of Texas at Austin, Bureau of Economic Geology*.

Galley, J.D. (1958). Oil and gas geology in the Permian Basin in Texas and New Mexico. *Weeks, L.G., ed., Habitat of oil—a symposium: Tulsa, Oklahoma, American Association of Petroleum Geologists, P. 395-446.*

Galloway, W.E., Tyler, N., Garrett Jr., C.M., Bebout, D.G., Cheng, E.S., Fisher, W.L., Ewing, T.E., Posey, J.S., Dutton, S.P. (1983). Geological Characterization of Texas Oil Reservoirs. *The University of Texas at Austin, Bureau of Economic Geology*.

Garber, R.A., Harris, P.M. (2009). Depositional Facies of Grayburg/San Andres Dolomite Reservoirs, Central Basin Platform, Permian Basin. *AAPG Search and Discovery Article No. 60031.*

Garcia-Fresca, B., Lucia, F.J., Sharp Jr., J.M., Kerans, C. (2012). Outcrop-constrained hydrogeological simulations of brine reflux and early dolomitization of the Permian San Andres Formation. *AAPG Bulletin, Vol. 96, No. 9, P. 1757-1781*.

George, P.G., Mace, R.E., Petrossian, R. (2011). Aquifers of Texas. *Texas Water Development Board, Report 380*.

Grigg, R.B., Svec, R.K., Ferguson, D.J. (2002). Improving CO_2 Efficiency for Recovering Oil in Heterogeneous Reservoirs. *New Mexico Petroleum Recovery Research Center, DOE Contract No. DE-FG26-01BC15364*.

Handford, C.R. (1981). Sedimentology and Genetic Stratigraphy of Dean and Spraberry Formations (Permian), Midland Basin, Texas. *The American Association of Petroleum Geologists.*

Helbert, D.K., Ruppel, S.C., Kerans, C., Fisher, W.L. (2010). Reservoir Characterization and Sequence Stratigraphy of Permian San Andres Platform Carbonates, Fullerton Field, Permian Basin, West Texas. *The University of Texas at Austin, Jackson School of Geosciences*.

Hinterlong, G.D., Taylor, A.R. (1996). Characterization of Rock Types with Mixed Wettability Using Log and Core Data – DOE Project Welch Field, Dawson County, Texas. *SPE-35160-MS.*

Hiss, K.A., Williamson, D.B. (2020). Facies and Stratigraphy of the San Andres Formation (Mid-Permian) Petroleum Province, Northwest Shelf of the Permian Basin, West Texas: A Resurgent Play. *The University of Texas at Dallas, GSA South-Central Section*.

Hoak, T., Sundberg, K., Ortoleva, P. (1998). Overview of the Structural Geology and Tectonics of the Central Basin Platform, Delaware Basin, and Midland Basin, West Texas and New Mexico. *U.S. Department of Energy, Report No. DOE/PC/91008-23-Pt.8.*

Holtz, M.H., Garrett Jr., C.M., Tremblay, T.A., Finley, R.J., Tyler, N. (1993). Update of Atlas of Major Texas Oil Reservoirs Data Base and Atlas of Major Texas Gas Reservoirs Data Base. *The University of Texas at Austin, Bureau of Economic Geology.*

Honarpour, M.M., Nagarajan, N.R., Grijalba, A.C., Valle, M., Adesoye, K. (2010). Rock-Fluid Characterization for Miscible CO_2 Injection: Residual Oil Zone, Seminole Field, Permian Basin. *Society of Petroleum Engineers, No. 133089.*

Horne, E.A., Hennings, P.H., Zahm, C.K. (2021). Basement-Rooted Faults of the Delaware Basin and Central Basin Platform, Permian Basin, West Texas and Southeastern New Mexico. *The University of Texas at Austin, Bureau of Economic Geology.*

Hoteit, H., Fahs, M., Soltanian, M.R. (2019). Assessment of CO_2 Injectivity During Sequestration in Depleted Gas Reservoirs. *MDPI Geosciences 2019, Vol. 9, No. 199.*

Hovorka, S.D. (1997). Salt Cavern Studies – Regional Map of Salt Thickness in the Midland Basin. *The University of Texas at Austin, Bureau of Economic Geology.*

Hovorka, S.D., Nava, R. (2000). Characterization of Bedded Salt for Storage Salt Caverns – A Case Study from the Midland Basin, Texas. *The University of Texas at Austin, Bureau of Economic Geology.*

Johnson, K.S. (1993). Dissolution of Permian Salado salt during Salado time in the Wink area, Winkler County, Texas. *New Mexico Geological Society, 44th Annual Fall Field Conference Guidebook, P. 211-218.*

Johnson, R.D., Mazzullo, J., Dorobek, S., Wu, C., Rabinowitz, P. (1997). The Facies, Environments of Deposition and Cyclicity of the Yates Formation, North Ward-Estes Field, Ward County, Texas. *Texas A&M University.*

Kerans, C. (2006). San Andres Formation: Outcrop to Subsurface Stratigraphic Framework. *The University of Texas at Austin, Jackson School of Geosciences.*

Kerans, C., Kempter, K. (2002). Hierarchical stratigraphic analysis of a carbonate platform, Permian of the Guadalupe Mountains. *The University of Texas at Austin, Bureau of Economic Geology, American Association of Petroleum Geologists – Datapages Discovery Series No. 5.*

Kerans, C., Lucia, F.J., Senger, R.K. (1994). Integrated Characterization of Carbonate Ramp Reservoirs Using Permian San Andres Formation Outcrop Analogs. *AAPG Bulletin, Vol. 78, No. 2, P. 181-216.*

Kerans, C., Lucia, F.J., Senger, R.K., Fogg, G.E., Nance, H.S., Hovorka, S.D. (1992). Characterization of Facies and Permeability Patterns in Carbonate Reservoirs based on Outcrop Analogs. *The University of Texas at Austin, Bureau of Economic Geology*.

Koperna, G.J. (2020). CarbonSAFE Phase II: 8.1.a Project ECO$_2$S Numerical Modeling Report. *U.S. Department of Energy, DOE Project DE-FE0029465*.

Kuuskraa, V.A., Petrusak, R., Wallace, M. (2020). A Four-County Appraisal of the San Andres Residual Oil Zone (ROZ) "Fairway" of the Permian Basin. *U.S. Department of Energy, National Energy Technology Laboratory, DOE/NETL-2020/2627*.

Lee, B., Khoudaiberdiev, R., Lujan, B., Verma, S. (2019). Depositional Environment and Sedimentary Structures of the Grayburg Formation, Midland Basin. *AAPG Search and Discovery Article No. 51550.*

Leibrock, R.M., Hiltz, R.G., Huzarevich, J.E. (1951). Results of Gas Injection in the Cedar Lake Field. *Petroleum Transactions, AIME, Vol. 192, P. 357-366*.

Li, S., Yu, X., Li, S., Giles, K.A. (2015). Role of sea-level change in deep water deposition along a carbonate shelf margin, Early and Middle Permian, Delaware Basin: implications for reservoir characterization. *Geologica Carpathica, Vol. 66, No. 2, P. 99-116*.

Lindsay, R. (2017). Grayburg Formation Reservoir-Scale Architecture and Sequence Stratigraphy, Permian Basin. *AAPG Search and Discovery Article No. 51388.*

Lucia, F.J. (2007). Carbonate Reservoir Characterization, an Integrated Approach. *The University of Texas at Austin, Bureau of Economic Geology*.

Matchus, E.J., Jones, T.S. (1984). East-west cross section through Permian Basin of West Texas. *West Texas Geological Society.*

Mazullo, J., Malicse, A., Siegel, J. (1991). Facies and Depositional Environments of the Shattuck Sandstone on the Northwest Shelf of the Permian Basin. *Journal of Sedimentary Petrology, Vol. 61, No. 6, P. 940-958.*

Mazzullo, S.J., Reid, A.M. (1989). Depositional-sequence analysis of Lower Permian progradational systems, Midland Basin, Texas. *Kansas Geological Survey, Subsurface Geology Vol. 12, P. 47-50*.

Mazzullo, S.J., Reid, A.M. (1989). Lower Permian Platform and Basin Depositional Systems, Northern Midland Basin, Texas. *Society of Economic Paleontologists and Mineralogists Special Publication No. 44*.

McKee, E.D., Oriel, S.S. (1967). Paleotectonic Investigations of the Permian System in the United States. *U.S. Department of the Interior (DOI), Geological Survey Professional Paper 515*.

Melzer, S. (2006). Stranded Oil in the Residual Oil Zone. *Prepared for Advanced Resources International and U.S. Department of Energy Office of Fossil Energy—Office of Oil and Natural Gas*. Retrieved from https://doi.org/10.13140/RG.2.2.16299.95528

Merrill, M.D., Slucher, E.R., Roberts-Ashby, T.L., Warwick, P.D., Blondes, M.S., Freeman, P.A., Cahan, S.M., DeVera, C.A., Lohr, C.D. (2015). Geologic Framework for the National Assessment of Carbon Dioxide Storage Resources – Permian, Palo Duro Basins, and Bend Arch-Fort Worth Basin. *USGS, Chapter K*.

Nance, H.S. (2006). Geology and Reservoir Development in the Upper Guadalupian Series Permian Basin. *The University of Texas at Austin, Jackson School of Geosciences.*

Nance, H.S. (2020). Guadalupian (Artesia Group) and Ochoan Shelf Succession of the Permian Basin: Effects of Deposition, Diagenesis, and Structure on Reservoir Development. *The University of Texas at Austin, Bureau of Economic Geology*.

Occidental Petroleum Ltd. (2015). Oxy Denver Unit CO_2 Subpart RR – Monitoring, Reporting and Verification (MRV) Plan. *Environmental Protection Agency*.

Occidental Petroleum Ltd. (2017). Oxy Hobbs Field CO_2 Subpart RR – Monitoring, Reporting and Verification (MRV) Plan. *Environmental Protection Agency*.

Occidental Petroleum Ltd. (2020). Oxy West Seminole San Andres Unit CO_2 Subpart RR – Monitoring, Reporting and Verification (MRV) Plan. *Environmental Protection Agency*.

Onishi, T., Nguyen, M.C., Carey, J.W., Will, B., Zaluski, W., Bowen, D.W., Devault, B.C., Duguid, A., Zhou, Q., Fairweather, S.H., Spangler, L.H., Stauffer, P.H. (2019). Potential CO_2 and brine leakage through wellbore pathways for geologic CO_2 sequestration using the National Risk Assessment Partnership tools: Application to the Big Sky Regional Partnership. *International Journal of Greenhouse Gas Control, Vol. 81, P. 44-65*.

Perlman, Z.S. (2017). Stratigraphic, Geochemical, and Geochronological Analysis of the Wolfcamp-D Interval, Midland Basin, Texas. *The University of Kentucky, Earth and Environmental Sciences*.

Playton, T., Kerans, C. (2006). Early Permian Carbonate Slope & Basin Channel-Fan Complexes, West Texas: Implications for Early Permian Deep Water Reservoir Development in the Permian Basin. *The University of Texas at Austin, Bureau of Economic Geology, PGGSP Annual Meeting*.

Popova, O. (2020). Permian Basin, Part 1: Wolfcamp, Bone Spring, Delaware Shale Plays of the Delaware Basin. *U.S. Energy Information Administration*. Retrieved from https://www.eia.gov/maps/pdf/Permian-pI_Wolfcamp-Bonespring-Delaware.pdf

Popova, O. (2022). Permian Basin, Part 2: Wolfcamp and Spraberry Shale Plays of the Midland Sub-Basin. *U.S. Energy Information Administration*. Retrieved from https://www.eia.gov/maps/pdf/Permian-p2_Spraberry_Midland.pdf

Pranter, M.J., Hurley, N.F., Davis, T.L. (2004). Anhydrite distribution within a shelf-margin carbonate reservoir: San Andres Formation, Vacuum Field, New Mexico, USA. *Geological Society of London, Petroleum Geoscience, Vol. 10, P. 43-52*.

Raza, A., Gholami, R., Rezaee, R., Bing, C.H., Nagarajan, R., Hamid, M.A. (2018). CO_2 storage in depleted gas reservoirs: A study on the effect of residual gas saturation. *Petroleum, Vol. 4, No. 1, P. 95-107*. Retrieved from https://doi.org/10.1016/j.petlm.2017.05.005

Raziperchikolaee, S., Singh, V., Kelley, M. (2020). The effect of Biot coefficient and elastic moduli stress–pore pressure dependency on poroelastic response to fluid injection: laboratory experiments and geomechanical modeling. *Greenhouse Gases: Science and Technology*. Retrieved from https://doi.org/10.1002/ghg.2019

Ren, B., Duncan, I.J. (2021). Maximizing Oil Production from Water Alternating Gas (CO_2) Injection into Residual Oil Zones: The Impact of Oil Saturation and Heterogeneity. *The University of Texas at Austin, Bureau of Economic Geology.* Retrieved from https://www.sciencedirect.com/science/article/pii/S036054422100164X

Ren, B., Duncan, I.J. (2019). Modeling Oil Saturation Evolution in Residual Oil Zones: Implications for CO_2 EOR and Sequestration. *The University of Texas at Austin, Bureau of Economic Geology.* Retrieved from https://www.sciencedirect.com/science/article/pii/S0920410519302098

Ren, B., Duncan, I.J. (2018). Reservoir Simulation of Carbon Storage Associated with CO_2 EOR in Residual Oil Zones, San Andres Formation of West Texas, Permian Basin, USA. *The University of Texas at Austin, Bureau of Economic Geology.* Retrieved from https://www.sciencedirect.com/science/article/pii/S0360544218322114

Rogers, B.F., Hu, Q. (2017). Petrophysical Characterization of the Jo Mill Submarine Fan Complex, Spraberry Trend, Midland Basin, Texas. *The University of Texas at Arlington*.

Rose, M.W. (2005). Application of Water-Jet Horizontal Drilling Technology to Drill and Acidize Horizontal Drain Holes, Tedbit (San Andres) Field, Gaines County, Texas. *U.S. Department of Energy, NETL/NPTO No. 288, P. 2-11*.

Ruppel, S.C. (2006). Key to Reservoir Development and Characterization: Clear Fork, Wichita, Abo. *The University of Texas at Austin, Jackson School of Geosciences.*

Ruppel, S.C. (2001). Opportunities for Recovery of Remaining Oil in San Andres Reservoirs: Example from Fuhrman-Mascho Field, University Lands Block 10, Andrews County, Texas. *The University of Texas at Austin, Jackson School of Geosciences.*

Ruppel, S.C., Cander, H.S. (1988). Dolomitization of shallow-water platform carbonates by sea water and seawater-derived brines: San Andres Formation (Guadalupian), West Texas. *SEPM Special Publications No. 43.*

Saller, A., Bierly, L., Shafer, D., Owens, L. (2012). Contrasting Styles of San Andres Reservoirs: Vacuum Versus Slaughter Fields, Middle Permian, West Texas and Southeast New Mexico. *AAPG Search and Discovery Article No. 20168.*

Sarg, J.F. (1981). Petrology of the carbonate-evaporite facies transition of the Seven Rivers Formation (Guadalupian, Permian), southeast New Mexico. *Journal of Sedimentary Petrology, Vol. 51, No. 1, P. 73-96.*

SEPM Strata (2022). The Geology of the Upper Permian – Permian Basin. *SEPM Strata – Society for Sedimentary Geology.* Retrieved from www.sepmstrata.org

Shelton, J.L., McIntosh, J.C., Hunt, A.G., Beebe, T.L., Parker, A.D., Warwick, P.D., Drake II, R.M., McCray, J.E. (2016). Determining CO_2 storage potential during miscible CO_2 enhanced oil recovery: Noble gas and stable isotope tracers. *International Journal of Greenhouse Gas Control, Vol. 51, P. 239-253*.

Silver, B.A., Todd, R.G. (1969). Permian cyclic strata, northern Midland and Delaware Basins, West Texas and Southeastern New Mexico. *American Association of Petroleum Geologists Bulletin, Vol. 53, P. 2223-2251.*

Snee, J.L., Zoback, M.D. (2018). State of stress in the Permian Basin, Texas and New Mexico: Implications for induced seismicity. *Stanford University, Department of Geophysics, The Leading Edge*.

Spitz, T., Chalmers, H., Ascui, F., Lucquiaud, L. (2017). Operating flexibility of CO_2 injection wells in future low carbon energy system. *Energy Procedia, Vol. 114, P. 4797-4810*.

Tait, D.B., Ahlen, J.L., Gordon, A., Scott, G.L., Motts, W.S., Spitler, M.E. (1962). Artesia Group of New Mexico and West Texas. *Bulletin of the American Association of Petroleum Geologists, Vol. 46, No. 4, P. 504-517.*

Teeple, A.P., Ging, P.B., Thomas, J.V., Wallace, D.S., Payne, J.D. (2021). Hydrogeologic Framework, Geochemistry, Groundwater-Flow System, and Aquifer Hydraulic Properties Used in the Development of a Conceptual Model of the Ogallala, Edwards-Trinity (High Plains), and Dockum Aquifers in and near Gaines, Terry, and Yoakum Counties, Texas. *USGS Scientific Investigations Report 2021-5009.*

Tinsley, W.E., Shurbet, M., Gilmore, R.B., McCoy, J.H., Potts, M.T., Illig, C. (1972). A Survey of the Subsurface Saline Water of Texas. *Texas Water Development Board, Vol. 2, Report No. 157*.

Trentham, R.C. (2014). Goldsmith Landreth San Andres Unit (GLSAU) No. 203R-A CO_2 Oil Bank Caught in the Act. *AAPG Search and Discovery Article No. 10648.*

Trentham, R.C., Melzer, L.S., Kuuskraa, V., Koperna, G. (2015). Case Studies of the ROZ CO_2 Flood and the Combined ROZ/MPZ CO_2 Flood at the Goldsmith Landreth Unit, Ector County,

Texas. Using "Next Generation" CO$_2$ EOR Technologies to Optimize the Residual Oil Zone CO$_2$ Flood. *U.S. Department of Energy, DE-FE0005889.*

Trentham, R.C., Melzer, L.S., Vance, D.B., Kuuskraa, V., Petrusak, R. (2015). Identifying and developing technology for enabling small producers to pursue the residual oil zone (ROZ) fairways in the Permian Basin San Andres. University of Texas of the Permian Basin, RPSEA. Retrieved from https://www.researchgate.net/publication/341357679

Tucker, K.E., Chalcraft, R.G. (1991). Cyclicity in the Permian Queen Formation – U.S.M. Queen Field, Pecos County, Texas. *SEPM Society for Sedimentary Geology, Vol. 15, P. 385-428*. Retrieved from https://doi.org/10.2110/cor.91.15

Tutolo, B.M., Luhmann, A.J., Kong, X.Z., Saar, M.O., Seyfried Jr., W.E. (2019). CO$_2$ sequestration in feldspar-rich sandstone: Coupled evolution of fluid chemistry, mineral reaction rates, and hydrogeochemical properties. *University of Minnesota, Department of Earth Sciences*. Retrieved from https://www.sciencedirect.com/science/article/pii/S0016703715001957

Tyler, N., Guevara, E.H., Coates, G.R., Wolff, M., Mukhopadhyay, P.K., Roberts, M.P., Gholston, J.C., Farrely, J.J., Graham, R.L., Walter, T., Reistroffer, J.R. (1987). Geological Characterization and Reserve Growth Potential of Spraberry Reservoirs in the Midland Basin, West Texas. *The University of Texas at Austin, Bureau of Economic Geology.*

Wahlman, G.P., Tasker, D.R. (2013). Lower Permian (Wolfcampian) Carbonate Shelf-Margin and Slope Facies, Central Basin Platform and Hueco Mountains, Permian Basin, West Texas, USA. *SEPM Society for Sedimentary Geology, Special Publication No. 105, P. 305-333*.

Waite, L. (2021). Stratigraphic Framework of the Wolfcamp-Spraberry of the Midland Basin. *University of Texas at Dallas, Abilene Geologic Society*.

Waite, L. (2019). Stratigraphic Framework of the Wolfcamp-Spraberry of the Midland Basin. *University of Texas at Dallas, Roswell Geologic Society*.

Waite, L., Stern, R.J. (2021). Reefs of the Permo-Penn Caribbean: The Horseshoe Atoll of the Midland Basin. *University of Texas at Dallas.*

Wang, J., Zhao, Y., An, Z., Shabani, A. (2022). CO$_2$ storage in carbonate rocks: An experimental and geochemical modeling study. *Journal of Geochemical Exploration, Vol. 234, P. 1-14*. Retrieved from https://doi.org/10.1016/j.gexplo.2021.106942

Ward, R.F., Kendall, C.G., Harris, P.M. (1986). Upper Permian (Guadalupian) facies and their association with hydrocarbons – Permian Basin, west Texas and New Mexico. *AAPG Bulletin, Vol. 70, No. 3, P. 239-262*.

Ward, Z.D., Pashin, J.C., Puckette, J., Hileman, M. (2013). Depositional Processes and Environments in Wolfcampian-Leonardian Strata, Southern Midland Basin, Texas. *Oklahoma State University*.

Warn, G.F., Sidwell, R. (1953). Petrology of the Spraberry Sands of West Texas. *Journal of Sedimentary Petrology, Vol. 23, No. 2, P. 67-74*.

Wells, J.A., Evans, L.J. (1992). Engineering Evaluation and Performance Analysis of the Loop Gas Storage Field. *Society of Petroleum Engineers, SPE No. 24922*.

Zapata, Y., Kristensen, M.R., Huerta, N., Brown, C., Kabir, C.S., Reza, Z. (2020). CO_2 geological storage: Critical insights on plume dynamics and storage efficiency during long-term and post-injection period. *Journal of Natural Gas Science and Engineering, Vol. 83, P. 1-29*. Retrieved from https://doi.org/10.1016/j.jngse.2020.103542